

Introduction to QCD*

P. Z. Skands[†]

Theoretical Physics, CERN, 1211 Geneva 23, Switzerland
 School of Physics & Astronomy, Monash University, Clayton VIC 3800, Australia

Updated: July, 2017

Abstract

These lectures were originally given at TASI 2012 and are directed at a level suitable for graduate students in High Energy Physics. They are intended to give an introduction to the theory and phenomenology of quantum chromodynamics (QCD), focusing on collider physics applications. The aim is to bring the reader to a level where informed decisions can be made concerning different approaches and their uncertainties. The material is divided into five main areas: 1) fundamentals, 2) fixed-order perturbative QCD, 3) Monte Carlo event generators and parton showers, 4) Matching at Leading and Next-to-Leading Order, and 5) Hadronization and soft hadron-hadron physics.

Useful Complementary References

- Basic Quantum Field Theory: [1]
- Textbooks on QCD: [2–4]
- Jets and Jet Algorithms: [5]
- General-Purpose Event Generators: [6]
- The String Model: [7, 8]
- Underlying Event and Multiple Parton Interactions: [9, 10]
- Step-by-step PYTHIA tutorial: see “worksheet” available on the PYTHIA homepage.
- Monte Carlo methods and Random Numbers: [11, 12]
- The veto algorithm, trial showers, the Sudakov algorithm [13–15]

*Lectures presented at TASI 2012: Theoretical Advanced Study Institute in Elementary Particle Physics — Searching for New Physics at Small and Large Scales. University of Colorado, Boulder, CO, June 4 – 29, 2012. Based on lectures first given at ESHEP 2010 (Raseborg, Finland); updated for AEPSHEP 2014 (Puri, India), pre-SUSY 2016 (Melbourne, Australia), and for MCNET 2017 (Lund, Sweden).

[†]peter.skands@monash.edu

Contents

1	Introduction	3
1.1	A First Hint of Colour	4
1.2	The Lagrangian of QCD	5
1.3	Colour Factors	6
1.4	The Strong Coupling	10
1.5	Colour States	15
2	Hard Processes	17
2.1	Factorization	18
2.2	Parton Densities	20
2.3	Fixed-Order QCD	24
2.4	The Subtraction Idea	27
2.5	Infrared Safety	29
3	Monte Carlo Event Generators	32
3.1	The Monte Carlo Method	33
3.2	Theoretical Basis of Parton Showers	34
3.3	Perturbation Theory with Markov Chains	42
3.4	Decays of Unstable Particles	44
4	Matching at LO and NLO	45
4.1	Slicing	45
4.2	Subtraction	48
4.3	Unitarity	49
5	Hadronisation and Soft Hadron-Hadron Physics	51
5.1	The String Model of Hadronisation	53
5.2	Soft Hadron-Hadron Processes	58
5.3	Underlying Event and Multiple Parton Interactions	61
5.4	Tuning	64
	References	67
	Index	83

1 Introduction

When probed at very short wavelengths, QCD is essentially a theory of free ‘partons’ — quarks and gluons — which only scatter off one another through relatively small quantum corrections, that can be systematically calculated. But at longer wavelengths, of order the size of the proton $\sim 1\text{fm} = 10^{-15}\text{m}$, we see strongly bound towers of hadron resonances emerge, with string-like potentials building up if we try to separate their partonic constituents. Due to our inability to perform analytic calculations in strongly coupled field theories, QCD is therefore still only partially solved. Nonetheless, all its features, across all distance scales, are believed to be encoded in a single one-line formula of alluring simplicity; the Lagrangian¹ of QCD.

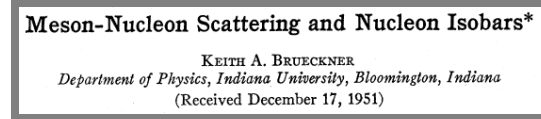
The consequence for collider physics is that some parts of QCD can be calculated in terms of the fundamental parameters of the Lagrangian, whereas others must be expressed through models or functions whose effective parameters are not a priori calculable but which can be constrained by fits to data. However, even in the absence of a perturbative expansion, there are still several strong theorems which hold, and which can be used to give relations between seemingly different processes. (This is, e.g., the reason it makes sense to measure the partonic substructure of the proton in ep collisions and then re-use the same parametrisations for pp collisions.) Thus, in the chapters dealing with phenomenological models we shall emphasise that the loss of a factorised perturbative expansion is not equivalent to a total loss of predictivity.

An alternative approach would be to give up on calculating QCD and use leptons instead. Formally, this amounts to summing inclusively over strong-interaction phenomena, when such are present. While such a strategy might succeed in replacing what we do know about QCD by “unity”, however, even the most adamant chromophobe would acknowledge the following basic facts of collider physics for the next decade(s): 1) At the LHC, the initial states are hadrons, and hence, at the very least, well-understood and precise parton distribution functions (PDFs) will be required; 2) high precision will mandate calculations to higher orders in perturbation theory, which in turn will involve more QCD; 3) the requirement of lepton *isolation* makes the very definition of a lepton depend implicitly on QCD and 4) the rate of jets that are mis-reconstructed as leptons in the experiment depends explicitly on it. And, 5) though many new-physics signals *do* give observable signals in the lepton sector, this is far from guaranteed, nor is it exclusive when it occurs. It would therefore be unwise not to attempt to solve QCD to the best of our ability, the better to prepare ourselves for both the largest possible discovery reach and the highest attainable subsequent precision.

Furthermore, QCD is the richest gauge theory we have so far encountered. Its emergent phenomena, unitarity properties, colour structure, non-perturbative dynamics, quantum vs. classical limits, interplay between scale-invariant and scale-dependent properties, and its wide range of phenomenological applications, are still very much topics of active investigation, about which we continue to learn.

In addition, or perhaps as a consequence, the field of QCD is currently experiencing something of a revolution. On the perturbative side, new methods to compute scattering amplitudes with very high particle multiplicities are being developed, together with advanced techniques for combining such amplitudes with all-orders resummation frameworks. On the non-perturbative side, the wealth of data on soft-physics processes from the LHC is forcing us

¹Throughout these notes we let it be implicit that “Lagrangian” really refers to Lagrangian density, \mathcal{L} , the four-dimensional space-time integral of which is the action.



[...] It is concluded that the apparently anomalous features of the scattering can be interpreted to be an indication of a resonant meson-nucleon interaction corresponding to a nucleon isobar with spin $\frac{3}{2}$, isotopic spin $\frac{3}{2}$, and with an excitation energy of 277 MeV."

Figure 1: The title and part of the abstract of the 1951 paper [16] (published in 1952) in which the existence of the Δ^{++} baryon was deduced, based on data from Sachs and Steinberger at Columbia [17] and from Anderson, Fermi, Nagle, et al. at Chicago [18]. Further studies at Chicago were quickly performed in [19, 20]. See also the memoir by Nagle [21].

to reconsider the reliability of the standard fragmentation models, and heavy-ion collisions are providing new insights into the collective behavior of hadronic matter. The study of cosmic rays impinging on the Earth’s atmosphere challenges our ability to extrapolate fragmentation models from collider energy scales to the region of ultra-high energy cosmic rays. And finally, dark-matter annihilation processes in space may produce hadrons, whose spectra are sensitive to the modeling of fragmentation.

In the following, we shall focus on QCD for mainstream collider physics. This includes the basics of SU(3), colour factors, the running of α_s , factorisation, hard processes, infrared safety, parton showers and matching, event generators, hadronisation, and the so-called underlying event. While not covering everything, hopefully these topics can also serve at least as stepping stones to more specialised issues that have been left out, such as twistor-inspired techniques, heavy flavours, polarisation, or forward physics, or to topics more tangential to other fields, such as axions, lattice QCD, or heavy-ion physics.

1.1 A First Hint of Colour

Looking for new physics, as we do now at the LHC, it is instructive to consider the story of the discovery of colour. The first hint was arguably the Δ^{++} baryon, discovered in 1951 [16]. The title and part of the abstract from this historical paper are reproduced in figure 1. In the context of the quark model — which first had to be developed, successively joining together the notions of spin, isospin, strangeness, and the eightfold way² — the flavour and spin content of the Δ^{++} baryon is:

$$|\Delta^{++}\rangle = |u\uparrow u\uparrow u\uparrow\rangle , \quad (1)$$

clearly a highly symmetric configuration. However, since the Δ^{++} is a fermion, it must have an overall antisymmetric wave function. In 1965, fourteen years after its discovery, this was finally understood by the introduction of colour as a new quantum number associated with the group SU(3) [22, 23]. The Δ^{++} wave function can now be made antisymmetric by arranging

²In physics, the “eightfold way” refers to the classification of the lowest-lying pseudoscalar mesons and spin-1/2 baryons within octets in SU(3)-flavour space (u, d, s). The Δ^{++} is part of a spin-3/2 baryon decuplet, a “tenfold way” in this terminology.

its three quarks antisymmetrically in this new degree of freedom,

$$|\Delta^{++}\rangle = \epsilon^{ijk} |u_{i\uparrow} u_{j\uparrow} u_{k\uparrow}\rangle , \quad (2)$$

hence solving the mystery.

More direct experimental tests of the number of colours were provided first by measurements of the decay width of $\pi^0 \rightarrow \gamma\gamma$ decays, which is proportional to N_C^2 , and later by the famous “R” ratio in e^+e^- collisions ($R = \sigma(e^+e^- \rightarrow q\bar{q})/\sigma(e^+e^- \rightarrow \mu^+\mu^-)$), which is proportional to N_C , see e.g. [4]. Below, in Section 1.2 we shall see how to calculate such colour factors.

1.2 The Lagrangian of QCD

Quantum Chromodynamics is based on the gauge group $SU(3)$, the Special Unitary group in 3 (complex) dimensions, whose elements are the set of unitary 3×3 matrices with determinant one. Since there are 9 linearly independent unitary complex matrices³, one of which has determinant 1, there are a total of 8 independent directions in this matrix space, corresponding to eight different generators as compared with the single one of QED. In the context of QCD, we normally represent this group using the so-called *fundamental*, or *defining*, representation, in which the generators of $SU(3)$ appear as a set of eight traceless and hermitean matrices, to which we return below. We shall refer to indices enumerating the rows and columns of these matrices (from 1 to 3) as *fundamental* indices, and we use the letters i, j, k, \dots , to denote them. We refer to indices enumerating the generators (from 1 to 8), as *adjoint* indices⁴, and we use the first letters of the alphabet (a, b, c, \dots) to denote them. These matrices can operate both on each other (representing combinations of successive gauge transformations) and on a set of 3-vectors, the latter of which represent quarks in colour space; the quarks are *triplets* under $SU(3)$. The matrices can be thought of as representing gluons in colour space (or, more precisely, the gauge transformations carried out by gluons), hence there are eight different gluons; the gluons are *octets* under $SU(3)$.

The Lagrangian density of QCD is

$$\mathcal{L} = \psi_q^i (i\gamma^\mu) (D_\mu)_{ij} \psi_q^j - m_q \psi_q^i \psi_{qi} + \frac{1}{4} F_{\mu\nu}^a F^{a\mu\nu}, \quad (3)$$

where ψ_q^i denotes a quark field with (fundamental) colour index i , $\psi_q = (\psi_{qR}, \psi_{qG}, \psi_{qB})^T$, γ^μ is a Dirac matrix that expresses the vector nature of the strong interaction, with μ being a Lorentz vector index, m_q allows for the possibility of non-zero quark masses (induced by the standard Higgs mechanism or similar), $F_{\mu\nu}^a$ is the gluon field strength tensor for a gluon⁵ with (adjoint) colour index a (i.e., $a \in [1, \dots, 8]$), and D_μ is the covariant derivative in QCD,

$$(D_\mu)_{ij} = \delta_{ij} \partial_\mu - ig_s t_{ij}^a A_\mu^a, \quad (4)$$

with g_s the strong coupling (related to α_s by $g_s^2 = 4\pi\alpha_s$; we return to the strong coupling in more detail below), A_μ^a the gluon field with colour index a , and t_{ij}^a proportional to the

³A complex $N \times N$ matrix has $2N^2$ degrees of freedom, on which unitarity provides N^2 constraints.

⁴The dimension of the *adjoint*, or *vector*, representation is equal to the number of generators, $N^2 - 1 = 8$ for $SU(3)$, while the dimension of the fundamental representation is the degree of the group, $N = 3$ for $SU(3)$.

⁵The definition of the gluon field strength tensor will be given below in equation (11).

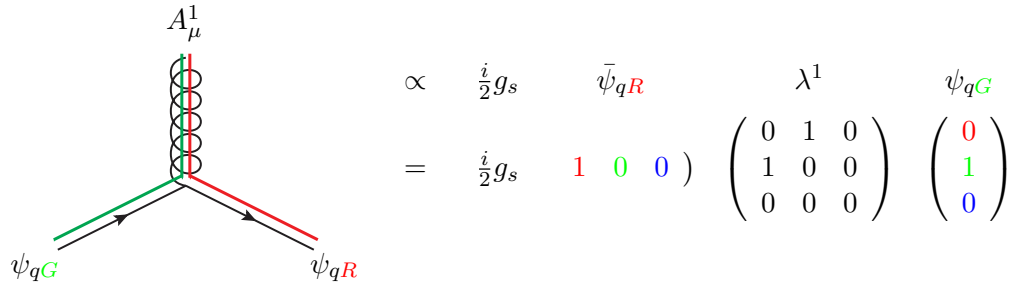


Figure 2: Illustration of a qqg vertex in QCD, before summing/averaging over colours: a gluon in a state represented by λ^1 interacts with quarks in the states ψ_{qR} and ψ_{qG} .

hermitean and traceless Gell-Mann matrices of $SU(3)$,

$$\begin{aligned} \lambda^1 &= \begin{pmatrix} 0 & 1 & 0 \\ 1 & 0 & 0 \\ 0 & 0 & 0 \end{pmatrix}, \quad \lambda^2 = \begin{pmatrix} 0 & i & 0 \\ i & 0 & 0 \\ 0 & 0 & 0 \end{pmatrix}, \quad \lambda^3 = \begin{pmatrix} 1 & 0 & 0 \\ 0 & 1 & 0 \\ 0 & 0 & 0 \end{pmatrix}, \quad \lambda^4 = \begin{pmatrix} 0 & 0 & 1 \\ 0 & 0 & 0 \\ 1 & 0 & 0 \end{pmatrix} \\ \lambda^5 &= \begin{pmatrix} 0 & 0 & i \\ 0 & 0 & 0 \\ i & 0 & 0 \end{pmatrix}, \quad \lambda^6 = \begin{pmatrix} 0 & 0 & 0 \\ 0 & 0 & 1 \\ 0 & 1 & 0 \end{pmatrix}, \quad \lambda^7 = \begin{pmatrix} 0 & 0 & 0 \\ 0 & 0 & i \\ 0 & i & 0 \end{pmatrix}, \quad \lambda^8 = \begin{pmatrix} \frac{1}{\sqrt{3}} & 0 & 0 \\ 0 & \frac{1}{\sqrt{3}} & 0 \\ 0 & 0 & \frac{2}{\sqrt{3}} \end{pmatrix}. \end{aligned} \quad (5)$$

These generators are just the $SU(3)$ analogs of the Pauli matrices in $SU(2)$. By convention, the constant of proportionality is normally taken to be

$$t_{ij}^a = \frac{1}{2} \lambda_{ij}^a. \quad (6)$$

This choice in turn determines the normalisation of the coupling g_s , via equation (4), and fixes the values of the $SU(3)$ Casimirs and structure constants, to which we return below.

An example of the colour flow for a quark-gluon interaction in colour space is given in figure 2. Normally, of course, we sum over all the colour indices, so this example merely gives a pictorial representation of what one particular (non-zero) term in the colour sum looks like.

1.3 Colour Factors

Typically, we do not measure colour in the final state — instead we average over all possible incoming colours and sum over all possible outgoing ones, wherefore QCD scattering amplitudes (squared) in practice always contain sums over quark fields contracted with Gell-Mann matrices. These contractions in turn produce traces which yield the *colour factors* that are associated to each QCD process, and which basically count the number of “paths through colour space” that the process at hand can take⁶.

⁶The convention choice represented by equation (6) introduces a “spurious” factor of 2 for each power of the coupling α_s . Although one could in principle absorb that factor into a redefinition of the coupling, effectively redefining the normalisation of “unit colour charge”, the standard definition of α_s is now so entrenched that alternative choices would be counter-productive, at least in the context of a pedagogical review.

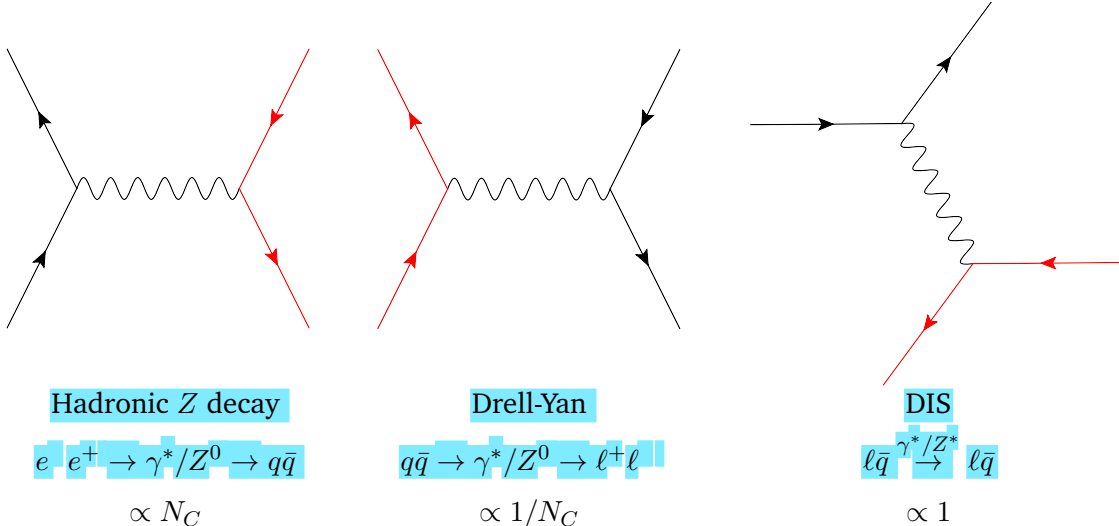


Figure 3: Illustration of the three crossings of the interaction of a lepton current (black) with a quark current (red) via an intermediate photon or Z boson, with corresponding colour factors.

A very simple example of a colour factor is given by the decay process $Z \rightarrow q\bar{q}$. This vertex contains a simple δ_{ij} in colour space; the outgoing quark and antiquark must have identical (anti-)colours. Squaring the corresponding matrix element and summing over final-state colours yields a colour factor of

$$e^+ e^- \rightarrow Z \rightarrow q\bar{q} \quad : \quad \sum_{\text{colours}} |M|^2 \propto \delta_{ij}\delta_{ji} = \text{Tr}\{\delta\} = N_C = 3 , \quad (7)$$

since i and j are quark (i.e., 3-dimensional fundamental) indices. This factor corresponds directly to the 3 different “paths through colour space” that the process at hand can take; the produced quarks can be red, green, or blue.

A next-to-simplest example is given by $q\bar{q} \rightarrow \gamma^*/Z \rightarrow \ell^+\ell^-$ (usually referred to as the Drell-Yan process [24]), which is just a crossing of the previous one. By crossing symmetry, the squared matrix element, including the colour factor, is exactly the same as before, but since the quarks are here incoming, we must *average* rather than sum over their colours, leading to

$$q\bar{q} \rightarrow Z \rightarrow e^+e^- \quad : \quad \frac{1}{9} \sum_{\text{colours}} |M|^2 \propto \frac{1}{9} \delta_{ij} \delta_{ji} = \frac{1}{9} \text{Tr}\{\delta\} = \frac{1}{3}, \quad (8)$$

where the colour factor now expresses a *suppression* which can be interpreted as due to the fact that only quarks of matching colours are able to collide and produce a Z boson. The chance that a quark and an antiquark picked at random from the colliding hadrons have matching colours is $1/N_C$.

Similarly, $\ell q \rightarrow \ell q$ via *t*-channel photon exchange (usually called Deep Inelastic Scattering — DIS — with “deep” referring to a large virtuality of the exchanged photon), constitutes yet another crossing of the same basic process, see figure 3. The colour factor in this case comes out as unity.

To illustrate what happens when we insert (and sum over) quark-gluon vertices, such as the one depicted in figure 2, we take the process $Z \rightarrow 3$ jets. The colour factor for this process can

Trace Relation	Indices	Occurs in Diagram Squared
$\text{Tr}\{t^a t^b\} = T_R \delta^{ab}$	$a, b \in [1, \dots, 8]$	
$\sum_a t_{ij}^a t_{jk}^a = C_F \delta_{ik}$	$a \in [1, \dots, 8]$ $i, j, k \in [1, \dots, 3]$	
$\sum_{c,d} f^{acd} f^{bcd} = C_A \delta^{ab}$	$a, b, c, d \in [1, \dots, 8]$	
$t_{ij}^a t_{k\ell}^a = T_R \left(\delta_{jk} \delta_{i\ell} - \frac{1}{N_C} \delta_{ij} \delta_{k\ell} \right)$	$i, j, k, \ell \in [1, \dots, 3]$	

Table 1: Trace relations for t matrices (convention-independent). More relations can be found in [3, Section 1.2] and in [1, Appendix A.3].

be computed as follows, with the accompanying illustration showing a corresponding diagram (squared) with explicit colour-space indices on each vertex:

$$\begin{aligned}
 Z \rightarrow qg\bar{q} : \\
 \sum_{\text{colours}} |M|^2 &\propto \delta_{ij} t_{jk}^a t_{k\ell}^a \delta_{\ell i} \\
 &= \text{Tr}\{t^a t^a\} \\
 &= \frac{1}{2} \text{Tr}\{\delta\} = 4 ,
 \end{aligned}
 \quad
 \begin{array}{c}
 \text{Diagram: Two gluon loops connected by a vertical line. Left loop has indices } ij \text{ and } q_j, q_k. Right loop has indices } k\ell \text{ and } q_\ell, q_i. \\
 \text{Diagram: Two gluon loops connected by a vertical line. Left loop has indices } ij \text{ and } q_j, q_k. Right loop has indices } k\ell \text{ and } q_\ell, q_i.
 \end{array} \quad (9)$$

where the last $\text{Tr}\{\delta\} = 8$, since the trace runs over the 8-dimensional adjoint indices. If we want to “count the paths through colour space”, we should leave out the factor $\frac{1}{2}$ which comes from the normalisation convention for the t matrices, equation (6), hence this process can take 8 different paths through colour space, one for each gluon basis state.

The tedious task of taking traces over t matrices can be greatly alleviated by use of the relations given in Table 1. In the standard normalisation convention for the $SU(3)$ generators, equation (6), the Casimirs of $SU(3)$ appearing in Table 1 are⁷

$$T_R = \frac{1}{2} \quad C_F = \frac{4}{3} \quad C_A = N_C = 3 . \quad (10)$$

In addition, the gluon self-coupling on the third line in Table 1 involves factors of f^{abc} . These are called the *structure constants* of QCD and they enter via the non-Abelian term in the gluon

⁷See, e.g., [1, Appendix A.3] for how to obtain the Casimirs in other normalisation conventions. As an example, choosing $t_{ij}^a = \lambda_{ij}^a / \sqrt{2}$ would yield $T_R = 1$, $C_F = T_R(N_C^2 - 1)/N_C = 8/3$, $C_A = 3$.

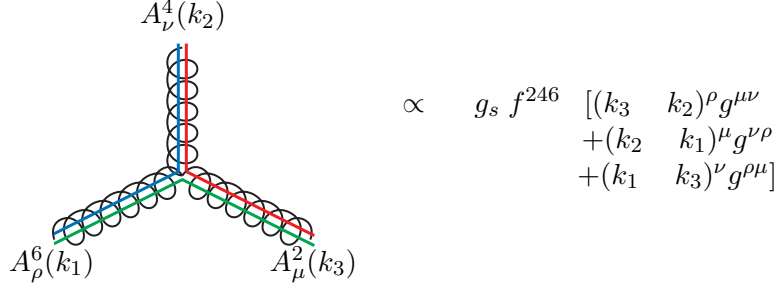


Figure 4: Illustration of a ggg vertex in QCD, before summing/averaging over colours: interaction between gluons in the states λ^2 , λ^4 , and λ^6 is represented by the structure constant f^{246} .

field strength tensor appearing in equation (3),

$$F_{\mu\nu}^a = \underbrace{\partial_\mu A_\nu^a - \partial_\nu A_\mu^a}_{\text{Abelian}} + g_s \underbrace{f^{abc} A_\mu^b A_\nu^c}_{\text{non Abelian}}. \quad (11)$$

The structure constants of $SU(3)$ are listed in the table to the right. They define the *adjoint*, or *vector*, representation of $SU(3)$ and are related to the fundamental-representation generators via the commutator relations

$$t^a t^b - t^b t^a = [t^a, t^b] = i f^{abc} t_c, \quad (12)$$

or equivalently,

$$i f^{abc} = 2 \text{Tr}\{t^c [t^a, t^b]\}. \quad (13)$$

Thus, it is a matter of choice whether one prefers to express colour space on a basis of fundamental-representation t matrices, or via the structure constants f , and one can go back and forth between the two.

Expanding the $F_{\mu\nu} F^{\mu\nu}$ term of the Lagrangian using equation (11), we see that there is a 3-gluon and a 4-gluon vertex that involve f^{abc} , the latter of which has two powers of f and two powers of the coupling.

Finally, the last line of Table 1 is not really a trace relation but instead a useful so-called Fierz transformation, which expresses products of t matrices in terms of Kronecker δ functions. It is often used, for instance, in shower Monte Carlo applications, to assist in mapping between colour flows in $N_C = 3$, in which cross sections and splitting probabilities are calculated, and those in $N_C \rightarrow \infty$ (“leading colour”), used to represent colour flow in the MC “event record”.

A gluon self-interaction vertex is illustrated in figure 4, to be compared with the quark-gluon one in figure 2. We remind the reader that gauge boson self-interactions are a hallmark

Structure Constants of $SU(3)$

$$f_{123} = 1 \quad (14)$$

$$f_{147} = f_{246} = f_{257} = f_{345} = \frac{1}{2} \quad (15)$$

$$f_{156} = f_{367} = \frac{1}{2} \quad (16)$$

$$f_{458} = f_{678} = \frac{\sqrt{3}}{2} \quad (17)$$

Antisymmetric in all indices

All other $f_{abc} = 0$

of non-Abelian theories and that their presence leads to some of the main differences between QED and QCD. One should also keep in mind that the colour factor for the vertex in figure 4, C_A , is roughly twice as large as that for a quark, C_F .

1.4 The Strong Coupling

To first approximation, QCD is *scale invariant*. That is, if one “zooms in” on a QCD jet, one will find a repeated self-similar pattern of jets within jets within jets, reminiscent of fractals. In the context of QCD, this property was originally called light-cone scaling, or Bjørken scaling. This type of scaling is closely related to the class of angle-preserving symmetries, called *conformal* symmetries. In physics today, the terms “conformal” and “scale invariant” are used interchangeably⁸. Conformal invariance is a mathematical property of several QCD-“like” theories which are now being studied (such as $N = 4$ supersymmetric relatives of QCD). It is also related to the physics of so-called “unparticles”, though that is a relation that goes beyond the scope of these lectures.

Regardless of the labelling, if the strong coupling did not run (we shall return to the running of the coupling below), Bjørken scaling would be absolutely true. QCD would be a theory with a fixed coupling, the same at all scales. This simplified picture already captures some of the most important properties of QCD, as we shall discuss presently.

In the limit of exact Bjørken scaling — QCD at fixed coupling — properties of high-energy interactions are determined only by dimensionless kinematic quantities, such as scattering angles (pseudorapidities) and ratios of energy scales⁹. For applications of QCD to high-energy collider physics, an important consequence of Bjørken scaling is thus that the rate of bremsstrahlung jets, with a given transverse momentum, scales in direct proportion to the hardness of the fundamental partonic scattering process they are produced in association with. This agrees well with our intuition about accelerated charges; the harder you “kick” them, the harder the radiation they produce.

For instance, in the limit of exact scaling, a measurement of the rate of 10-GeV jets produced in association with an ordinary Z boson could be used as a direct prediction of the rate of 100-GeV jets that would be produced in association with a 900-GeV Z' boson, and so forth. Our intuition about how many bremsstrahlung jets a given type of process is likely to have should therefore be governed first and foremost by the *ratios* of scales that appear in that particular process, as has been highlighted in a number of studies focusing on the mass and p_\perp scales appearing, e.g., in Beyond-the-Standard-Model (BSM) physics processes [25–28]. Bjørken scaling is also fundamental to the understanding of jet substructure in QCD, see, e.g., [29, 30].

On top of the underlying scaling behavior, the running coupling will introduce a dependence on the absolute scale, implying more radiation at low scales than at high ones. The

⁸Strictly speaking, conformal symmetry is more restrictive than just scale invariance, but examples of scale-invariant field theories that are not conformal are rare.

⁹Originally, the observed approximate agreement with this was used as a powerful argument for pointlike substructure in hadrons; since measurements at different energies are sensitive to different resolution scales, independence of the absolute energy scale is indicative of the absence of other fundamental scales in the problem and hence of pointlike constituents.

running is logarithmic with energy, and is governed by the so-called *beta function*,

$$Q^2 \frac{\partial \alpha_s}{\partial Q^2} = \frac{\partial \alpha_s}{\partial \ln Q^2} = \beta(\alpha_s) , \quad (18)$$

where the function driving the energy dependence, the beta function, is defined as

$$\beta(\alpha_s) = \alpha_s^2(b_0 + b_1 \alpha_s + b_2 \alpha_s^2 + \dots) , \quad (19)$$

with LO (1-loop) and NLO (2-loop) coefficients

$$b_0 = \frac{11C_A - 4T_R n_f}{12\pi} , \quad (20)$$

$$b_1 = \frac{17C_A^2 - 10T_R C_A n_f - 6T_R C_F n_f}{24\pi^2} = \frac{153 - 19n_f}{24\pi^2} . \quad (21)$$

In the b_0 coefficient, the first term is due to gluon loops while the second is due to quark ones. Similarly, the first term of the b_1 coefficient arises from double gluon loops, while the second and third represent mixed quark-gluon ones. At higher loop orders, the b_i coefficients depend explicitly on the renormalisation scheme that is used. A brief discussion can be found in the PDG review on QCD [31], with more elaborate ones contained in [3, 4]. Note that, if there are additional coloured particles beyond the Standard-Model ones, loops involving those particles enter at energy scales above the masses of the new particles, thus modifying the running of the coupling at high scales. This is discussed, e.g., for supersymmetric models in [32]. For the running of other SM couplings, see e.g., [33].

Numerically, the value of the strong coupling is usually specified by giving its value at the specific reference scale $Q^2 = M_Z^2$, from which we can obtain its value at any other scale by solving equation (18),

$$\alpha_s(Q^2) = \alpha_s(M_Z^2) \frac{1}{1 + b_0 \alpha_s(M_Z^2) \ln \frac{Q^2}{M_Z^2} + \mathcal{O}(\alpha_s^2)} , \quad (22)$$

with relations including the $\mathcal{O}(\alpha_s^2)$ terms available, e.g., in [3]. Relations between scales not involving M_Z^2 can obviously be obtained by just replacing M_Z^2 by some other scale Q'^2 everywhere in equation (22). A comparison of running at one- and two-loop order, in both cases starting from $\alpha_s(M_Z) = 0.12$, is given in figure 5. As is evident from the figure, the 2-loop running is somewhat faster than the 1-loop one.

As an application, let us prove that the logarithmic running of the coupling implies that an intrinsically multi-scale problem can be converted to a single-scale one, up to corrections suppressed by two powers of α_s , by taking the geometric mean of the scales involved. This follows from expanding an arbitrary product of individual α_s factors around an arbitrary scale μ , using equation (22),

$$\begin{aligned} \alpha_s(\mu_1) \alpha_s(\mu_2) \cdots \alpha_s(\mu_n) &= \prod_{i=1}^n \alpha_s(\mu) \left(1 + b_0 \alpha_s \ln \left(\frac{\mu^2}{\mu_i^2} \right) + \mathcal{O}(\alpha_s^2) \right) \\ &= \alpha_s^n(\mu) \left(1 + b_0 \alpha_s \ln \left(\frac{\mu^{2n}}{\mu_1^2 \mu_2^2 \cdots \mu_n^2} \right) + \mathcal{O}(\alpha_s^2) \right) , \end{aligned} \quad (23)$$

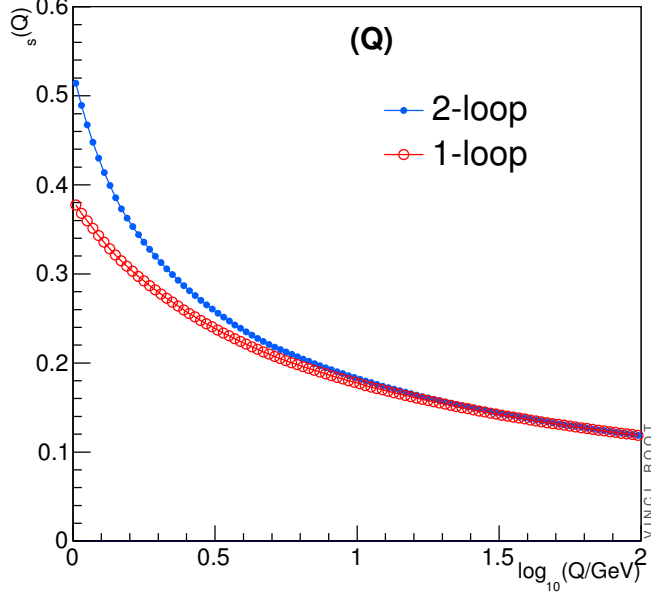


Figure 5: Illustration of the running of α_s at 1- (open circles) and 2-loop order (filled circles), starting from the same value of $\alpha_s(M_Z) = 0.12$.

whereby the specific single-scale choice $\mu^n = \mu_1\mu_2 \cdots \mu_n$ (the geometric mean) can be seen to push the difference between the two sides of the equation one order higher than would be the case for any other combination of scales¹⁰.

The appearance of the number of flavours, n_f , in b_0 implies that the slope of the running depends on the number of contributing flavours. Since full QCD is best approximated by $n_f = 3$ below the charm threshold, by $n_f = 4$ and 5 from there to the b and t thresholds, respectively, and then by $n_f = 6$ at scales higher than m_t , it is therefore important to be aware that the running changes slope across quark flavour thresholds. Likewise, it would change across the threshold for any coloured new-physics particles that might exist, with a magnitude depending on the particles' colour and spin quantum numbers.

The negative overall sign of equation (19), combined with the fact that $b_0 > 0$ (for $n_f \leq 16$), leads to the famous result¹¹ that the QCD coupling effectively *decreases* with energy, called asymptotic freedom, for the discovery of which the Nobel prize in physics was awarded to D. Gross, H. Politzer, and F. Wilczek in 2004. An extract of the prize announcement runs as follows:

¹⁰In a fixed-order calculation, the individual scales μ_i , would correspond, e.g., to the n hardest scales appearing in an infrared safe sequential clustering algorithm applied to the given momentum configuration.

¹¹Perhaps the highest pinnacle of fame for equation (19) was reached when the sign of it featured in an episode of the TV series “Big Bang Theory”.

What this year's Laureates discovered was something that, at first sight, seemed completely contradictory. The interpretation of their mathematical result was that the closer the quarks are to each other, the weaker is the “colour charge”. When the quarks are really close to each other, the force is so weak that they behave almost as free particles^a. This phenomenon is called “asymptotic freedom”. The converse is true when the quarks move apart: the force becomes stronger when the distance increases^b.

^aMore correctly, it is the coupling rather than the force which becomes weak as the distance decreases. The $1/r^2$ Coulomb singularity of the force is only damped, not removed, by the diminishing coupling.

^bMore correctly, it is the potential which grows, linearly, while the force becomes constant.

Among the consequences of asymptotic freedom is that perturbation theory becomes better behaved at higher absolute energies, due to the effectively decreasing coupling. Perturbative calculations for our 900-GeV Z' boson from before should therefore be slightly faster converging than equivalent calculations for the 90-GeV one. Furthermore, since the running of α_s explicitly breaks Bjørken scaling, we also expect to see small changes in jet shapes and in jet production ratios as we vary the energy. For instance, since high- p_\perp jets start out with a smaller effective coupling, their intrinsic shape (irrespective of boost effects) is somewhat narrower than for low- p_\perp jets, an issue which can be important for jet calibration. Our current understanding of the running of the QCD coupling is summarised by the plot in figure 6, taken from a recent comprehensive review by S. Bethke [31,34]. A complementary up-to-date overview of α_s determinations can be found in [35].

As a final remark on asymptotic freedom, note that the decreasing value of the strong coupling with energy must eventually cause it to become comparable to the electromagnetic and weak ones, at some energy scale. Beyond that point, which may lie at energies of order 10^{15} – 10^{17} GeV (though it may be lower if as yet undiscovered particles generate large corrections to the running), we do not know what the further evolution of the combined theory will actually look like, or whether it will continue to exhibit asymptotic freedom.

Now consider what happens when we run the coupling in the other direction, towards smaller energies. Taken at face value, the numerical value of the coupling diverges rapidly at scales below 1 GeV, as illustrated by the curves disappearing off the left-hand edge of the plot in figure 6. To make this divergence explicit, one can rewrite equation (22) in the following form,

$$\alpha_s(Q^2) = \frac{1}{b_0 \ln \frac{Q^2}{\Lambda^2}} , \quad (24)$$

where

$$\Lambda \sim 200 \text{ MeV} \quad (25)$$

specifies the energy scale at which the perturbative coupling would nominally become infinite, called the Landau pole. (Note, however, that this only parametrises the purely *perturbative* result, which is not reliable at strong coupling, so equation (24) should not be taken to imply that the physical behavior of full QCD should exhibit a divergence for $Q \rightarrow \Lambda$.)

Finally, one should be aware that there is a multitude of different ways of defining both Λ and $\alpha_s(M_Z)$. At the very least, the numerical value one obtains depends both on the renormalisation scheme used (with the dimensional-regularisation-based “modified minimal subtraction” scheme, $\overline{\text{MS}}$, being the most common one) and on the perturbative order of the

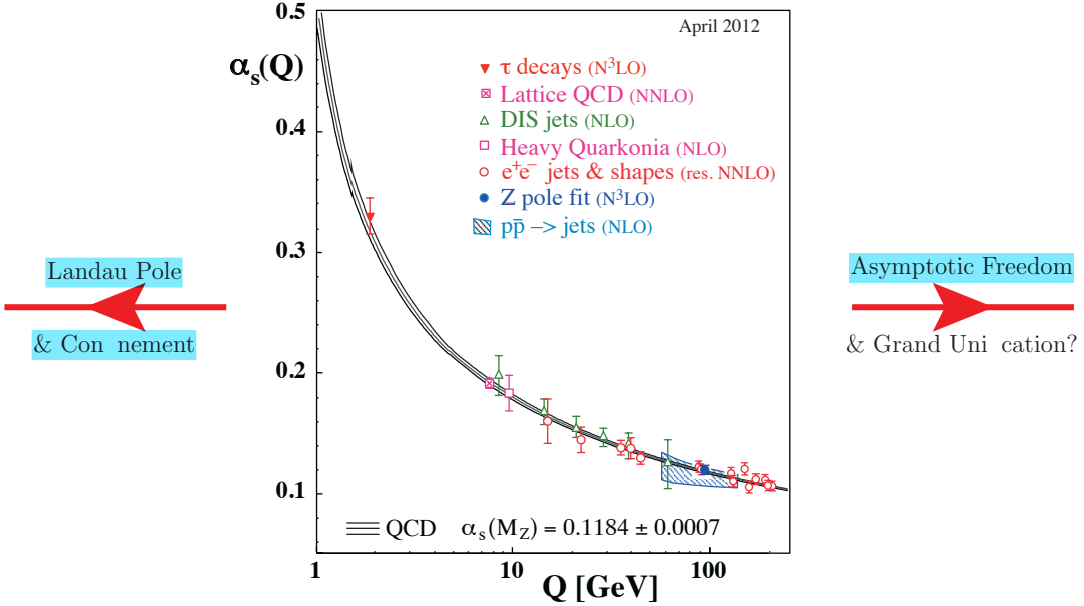


Figure 6: Illustration of the running of α_s in a theoretical calculation (band) and in physical processes at different characteristic scales, from [31, 34]. The little kinks at $Q = m_c$ and $Q = m_b$ are caused by discontinuities in the running across the flavour thresholds.

calculations used to extract them. As a rule of thumb, fits to experimental data typically yield smaller values for $\alpha_s(M_Z)$ the higher the order of the calculation used to extract it (see, e.g., [31, 34, 36, 37]), with $\alpha_s(M_Z)|_{\text{LO}} \gtrsim \alpha_s(M_Z)|_{\text{NLO}} \gtrsim \alpha_s(M_Z)|_{\text{NNLO}}$. Further, since the number of flavours changes the slope of the running, the location of the Landau pole for fixed $\alpha_s(M_Z)$ depends explicitly on the number of flavours used in the running. Thus each value of n_f is associated with its own value of Λ , with the following matching relations across thresholds guaranteeing continuity of the coupling at one loop,

$$n_f = 5 \leftrightarrow 6 : \quad \Lambda_6 = \Lambda_5 \left(\frac{\Lambda_5}{m_t} \right)^{\frac{2}{21}} \quad \Lambda_5 = \Lambda_6 \left(\frac{m_t}{\Lambda_6} \right)^{\frac{2}{23}}, \quad (26)$$

$$n_f = 4 \leftrightarrow 5 : \quad \Lambda_5 = \Lambda_4 \left(\frac{\Lambda_4}{m_b} \right)^{\frac{2}{23}} \quad \Lambda_4 = \Lambda_5 \left(\frac{m_b}{\Lambda_5} \right)^{\frac{2}{25}}, \quad (27)$$

$$n_f = 3 \leftrightarrow 4 : \quad \Lambda_4 = \Lambda_3 \left(\frac{\Lambda_3}{m_c} \right)^{\frac{2}{25}} \quad \Lambda_3 = \Lambda_4 \left(\frac{m_c}{\Lambda_4} \right)^{\frac{2}{27}}. \quad (28)$$

It is sometimes stated that QCD only has a single free parameter, the strong coupling. However, even in the perturbative region, the beta function depends explicitly on the number of quark flavours, as we have seen, and thereby also on the quark masses. Furthermore, in the non-perturbative region around or below Λ_{QCD} , the value of the perturbative coupling, as obtained, e.g., from equation (24), gives little or no insight into the behavior of the full theory. Instead, universal functions (such as parton densities, form factors, fragmentation functions, etc), effective theories (such as the Operator Product Expansion, Chiral Perturbation Theory,

or Heavy Quark Effective Theory), or phenomenological models (such as Regge Theory or the String and Cluster Hadronisation Models) must be used, which in turn depend on additional non-perturbative parameters whose relation to, e.g., $\alpha_s(M_Z)$, is not a priori known.

For some of these questions, such as hadron masses, lattice QCD can furnish important additional insight, but for multi-scale and/or time-evolution problems, the applicability of lattice methods is still severely restricted; the lattice formulation of QCD requires a Wick rotation to Euclidean space. The time-coordinate can then be treated on an equal footing with the other dimensions, but intrinsically Minkowskian problems, such as the time evolution of a system, are inaccessible. The limited size of current lattices also severely constrain the scale hierarchies that it is possible to “fit” between the lattice spacing and the lattice size.

1.5 Colour States

A final example of the application of the underlying SU(3) group theory to QCD is given by considering which colour states we can obtain by combinations of quarks and gluons. The simplest example of this is the combination of a quark and antiquark. We can form a total of nine different colour-anticolour combinations, which fall into two irreducible representations of SU(3):

$$3 \otimes \bar{3} = 8 \oplus 1 . \quad (29)$$

The singlet corresponds to the symmetric wave function $\frac{1}{\sqrt{3}} (|R\bar{R}\rangle + |G\bar{G}\rangle + |B\bar{B}\rangle)$, which is invariant under SU(3) transformations (the definition of a singlet). The other eight linearly independent combinations (which can be represented by one for each Gell-Mann matrix, with the singlet corresponding to the identity matrix) transform into each other under SU(3). Thus, although we sometimes talk about colour-singlet states as being made up, e.g., of “red-antired”, that is not quite precise language. The actual state $|R\bar{R}\rangle$ is *not* a pure colour singlet. Although it does have a non-zero *projection* onto the singlet wave function above, it also has non-zero projections onto the two members of the octet that correspond to the diagonal Gell-Mann matrices. Intuitively, one can also easily realise this by noting that an SU(3) rotation of $|R\bar{R}\rangle$ would in general turn it into a different state, say $|B\bar{B}\rangle$, whereas a true colour singlet would be invariant. Finally, we can also realise from equation (29) that a random (colour-uncorrelated) quark-antiquark pair has a $1/N^2 = 1/9$ chance to be in an overall colour-singlet state; otherwise it is in an octet.

Similarly, there are also nine possible quark-quark (or antiquark-antiquark) combinations, six of which are symmetric under interchange of the two quarks and three of which are anti-symmetric:

$$6 = \begin{pmatrix} |RR\rangle \\ |GG\rangle \\ |BB\rangle \\ \frac{1}{\sqrt{2}} (|RG\rangle + |GR\rangle) \\ \frac{1}{\sqrt{2}} (|GB\rangle + |BG\rangle) \\ \frac{1}{\sqrt{2}} (|BR\rangle + |RB\rangle) \end{pmatrix} \quad \bar{3} = \begin{pmatrix} \frac{1}{\sqrt{2}} (|RG\rangle & |GR\rangle) \\ \frac{1}{\sqrt{2}} (|GB\rangle & |BG\rangle) \\ \frac{1}{\sqrt{2}} (|BR\rangle & |RB\rangle) \end{pmatrix} . \quad (30)$$

The members of the sextet transform into (linear combinations of) each other under SU(3) transformations, and similarly for the members of the antitriplet, hence neither of these can

be reduced further. The breakdown into irreducible SU(3) multiplets is therefore

$$3 \otimes 3 = 6 \oplus \bar{3} . \quad (31)$$

Thus, an uncorrelated pair of quarks has a 1/3 chance to add to an overall anti-triplet state (corresponding to coherent superpositions like “red + green = antiblue”¹²); otherwise it is in an overall sextet state.

Note that the emphasis on the quark-(anti)quark pair being *uncorrelated* is important; production processes that correlate the produced partons, like $Z \rightarrow q\bar{q}$ or $g \rightarrow q\bar{q}$, will project out specific components (here the singlet and octet, respectively). Note also that, if the quark and (anti)quark are on opposite sides of the universe (i.e., living in two different hadrons), the QCD *dynamics* will not care what overall colour state they are in, so for the formation of multi-partonic states in QCD, obviously the spatial part of the wave functions (causality at the very least) will also play a role. Here, we are considering *only* the colour part of the wave functions. Some additional examples are

$$8 \otimes 8 = 27 \oplus 10 \oplus \bar{10} \oplus 8 \oplus 8 \oplus 1 , \quad (32)$$

$$3 \otimes 8 = 15 \oplus 6 \oplus 3 , \quad (33)$$

$$3 \otimes 6 = 10 \oplus 8 , \quad (34)$$

$$3 \otimes 3 \otimes 3 = (6 \oplus \bar{3}) \otimes 3 = 10 \oplus 8 \oplus 8 \oplus 1 . \quad (35)$$

Physically, the 27 in the first line corresponds to a completely incoherent addition of the colour charges of two gluons; the decuplets are slightly more coherent (with a lower total colour charge), the octets yet more, and the singlet corresponds to the combination of two gluons that have precisely equal and opposite colour charges, so that their total charge is zero. Further extensions and generalisations of these combination rules can be obtained, e.g., using the method of Young tableaux [38, 39].

¹²In the context of hadronisation models, this coherent superposition of two quarks in an overall antitriplet state is sometimes called a “diquark” (at low m_{qq}) or a “string junction” (at high m_{qq}), see section 5.1; it corresponds to the antisymmetric “red + green = antiblue” combination needed to create a baryon wavefunction.

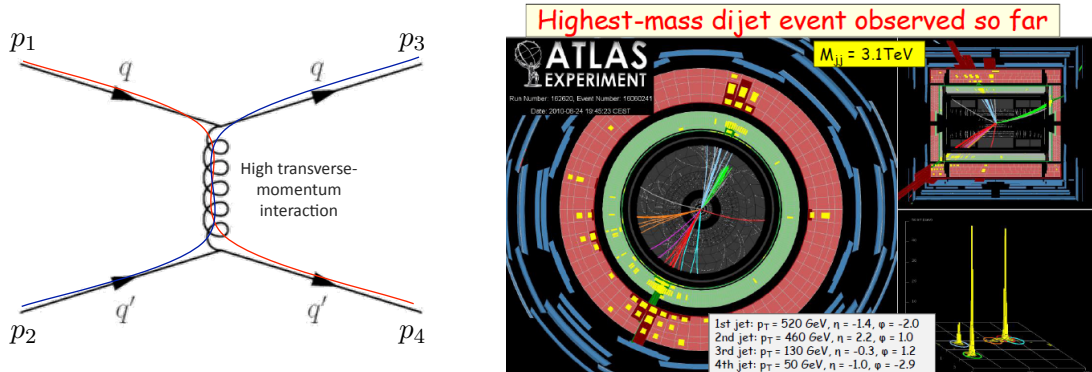


Figure 7: *Left:* Rutherford scattering of quarks in QCD, exemplifying the type of process that dominates the short-distance interaction cross section at hadron colliders. *Right:* an example of what such a reaction looks like in a detector, in this case the ATLAS experiment.

2 Hard Processes

Our main tool for solving QCD at high energy scales, $Q \gg \Lambda_{\text{QCD}}$, is perturbative quantum field theory, the starting point for which is Matrix Elements (MEs) which can be calculated systematically at fixed orders (FO) in the strong coupling α_s . At least at lowest order (LO), the procedure is standard textbook material [1] and it has also by now been highly automated, by the advent of tools like MADGRAPH [40], CALCHEP [41] / COMPEHEP [42], and several others [43–49]. Here, we require only that the reader has a basic familiarity with the methods involved from graduate-level particle physics courses based, e.g., on [1, 4]. Our main concern are the uses to which these calculations are put, their limitations, and ways to improve on the results obtained with them.

For illustration, take one of the most commonly occurring processes in hadron collisions: Rutherford scattering of two quarks via a t -channel gluon exchange — figure 7 — which at leading order has the differential cross section

$$q\bar{q}' \rightarrow q\bar{q}' : \frac{d\sigma}{d\hat{t}} = \frac{\pi}{\hat{s}^2} \frac{4}{9} \alpha_s^2 \frac{\hat{s}^2 + \hat{u}^2}{\hat{t}^2}, \quad (36)$$

with the $2 \rightarrow 2$ Mandelstam variables (“hatted” to emphasize that they refer to a partonic $2 \rightarrow 2$ scattering rather than the full $p\bar{p} \rightarrow \text{jets}$ process)

$$\hat{s} = (p_1 + p_2)^2, \quad (37)$$

$$\hat{t} = (p_3 - p_1)^2 = \frac{\hat{s}(1 - \cos\theta)}{2}, \quad (38)$$

$$\hat{u} = (p_4 - p_1)^2 = \frac{\hat{s}(1 + \cos\hat{\theta})}{2}. \quad (39)$$

Reality, however, is more complicated; the picture on the right-hand pane of figure 7 shows a real dijet event, as recorded by the ATLAS experiment. The complications to be addressed when going from left to right in figure 7 are: firstly, additional jets, a.k.a. real-emission corrections, which can significantly change the topology of the final state, potentially shifting jets

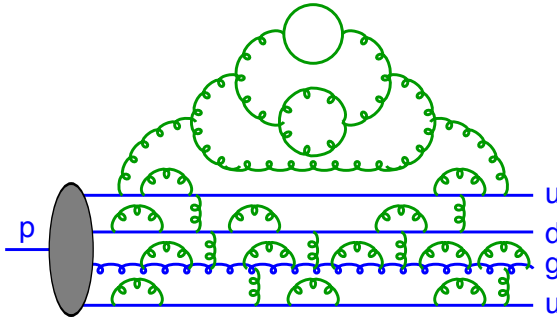


Figure 8: Illustration of partonic fluctuations inside a proton beam (from [50]).

in or out of an experimentally defined acceptance region. Secondly, loop factors, a.k.a. virtual corrections, change the number of available quantum paths through phase space, and hence modify the normalization of the cross section (total *and* differential). And finally, additional corrections are generated by confinement and by the so-called underlying event. These corrections must be taken into account to complete our understanding of QCD and connect the short-distance physics with macroscopic experiments. Apart from the perturbative expansion itself, the most powerful tool we have to organize this vast calculation, is factorization.

2.1 Factorization

In high-energy scattering problems involving hadrons in the initial state, we immediately face the complication that hadrons are composite, with a time-dependent structure illustrated in figure 8; there are partons within clouds of further partons, constantly being emitted and absorbed. Thus, before we can use perturbatively calculated partonic scattering matrix elements, we must first address the partonic structure of the colliding hadron(s).

For the hadron to remain intact, the fluctuations inside it must involve momentum transfers smaller than the confinement scale. Indeed, high-virtuality fluctuations are suppressed by powers of

$$\frac{\alpha_s \Lambda^2}{|k|^2}, \quad (40)$$

with Λ the confinement scale (~ 200 MeV, see section 1.4) and $|k|$ the virtuality of the fluctuation. Thus, most fluctuations occur over timescales $\sim 1/\Lambda$.

A hard perturbative probe, on the other hand, such as the exchanged photon in DIS (figure 3), interacts over a much shorter timescale $1/Q \ll 1/\Lambda$, during which the partonic fluctuations in the struck hadron appear almost frozen. The hard probe effectively takes an instantaneous snapshot of the hadron structure, at a characteristic resolution given by $\sim 1/Q$.

This is formalized by the *factorization theorem* [51] (see also the TASI lectures by George Sterman [52]), which expresses the independence of long-wavelength (soft) structure on the nature of the hard (short-distance) process. Originally formulated for DIS, factorization allows us to write the cross section for lepton-hadron scattering as a convolution of a non-perturbative but universal (i.e., process-independent) parton density function (PDF) and a perturbatively calculable partonic scattering cross section. Denoting the fraction of the hadron momentum

carried by parton i by x_i ,

$$\vec{p}_i = x_i \vec{p}_h , \quad (41)$$

we may write the lepton-hadron cross section on factorized form (see, e.g., [4, 53]),

$$\sigma_{\ell h} = \sum_i \int_0^1 dx_i \int d\Phi_f f_{i/h}(x_i, \mu_F^2) \frac{d\hat{\sigma}_{\ell i \rightarrow f}(x_i, \Phi_f, \mu_F^2)}{dx_i d\Phi_f} , \quad (42)$$

with i an index running over all possible parton types¹³ in the incoming hadron and f enumerating all possible (partonic) final states, with Lorentz-invariant phase space, Φ_f .

The *parton density functions* (PDFs), $f_{i/h}$, parametrize the distribution of partons inside the target hadron. They are not a priori calculable and must be constrained by fits to data. This is discussed in section 2.2.

The *partonic cross section*, $d\hat{\sigma}$, knows nothing of the target hadron apart from the fact that it contained the struck parton. It is calculable within perturbation theory, as will be discussed in section 2.3.

The dividing line between the two is drawn at an arbitrary (“user-defined”) scale μ_F , called the *factorization scale*. There is some arbitrariness involved in choosing a value for μ_F . Some heuristic arguments to guide in the choice of factorization scale are the following. On the long-distance side, the PDFs include a (re)summation of fluctuations inside fluctuations up to virtualities of order μ_F . It would therefore not make much sense to take μ_F significantly larger than the scales characterizing resolved particles on the short-distance side of the calculation (i.e., the particles appearing explicitly in Φ_f); otherwise the PDFs would be including sums over fluctuations that happen on timescales shorter than those probed by the physical process. Similarly, μ_F should also not be taken much lower than the scale(s) appearing in the hard process. For matrix elements characterized by a single well-defined scale, such as the Q^2 scale in DIS or the invariant-mass scale \hat{s} in Drell-Yan production ($q\bar{q} \rightarrow Z/\gamma^* \rightarrow \ell^+ \ell^-$), such arguments essentially fix the preferred scale choice to $\mu_F = Q$ or $\mu_F = \sqrt{\hat{s}}$, respectively, which may then be varied by a factor of 2 (or larger) around the nominal value in order to estimate uncertainties. For multi-scale problems, however, such as $pp \rightarrow Z/W + n$ jets, there are several a priori equally good choices available, from the lowest to the highest QCD scales that can be constructed from the final-state momenta, usually with several dissenting groups of theorists arguing over which particular choice is best. Suggesting that one might simply *measure* the scale would not really be an improvement, as the factorization scale is fundamentally unphysical and therefore unobservable (similarly to gauge or convention choices). One plausible strategy is to look at higher-order (NLO or NNLO) calculations, in which correction terms appear that cancel the dependence on the scale choice, stabilizing the final result. From such comparisons, a “most stable” initial scale choice can in principle be determined, which then furnishes a reasonable starting point, but we emphasize that the question is intrinsically ambiguous, and no golden recipe is likely to magically give all the right answers. The best we can do is to vary the value of μ_F not only by an overall factor, but also by exploring different possible forms for its functional dependence on the momenta appearing in Φ_f . A complementary useful discussion of the pros and cons of different factorization scale choices can be found in the TASI lectures by Tilman Plehn [54].

¹³Typically, only quarks and gluons are included in this sum, but also photons and even leptons can in principle be included. Similarly, parton density functions are normally used to describe hadrons, but can also be defined, e.g., to describe the cloud of virtual photons (and fermion pairs) surrounding an electron.

Secondly, and more technically, at NLO and beyond one also has to settle on a *factorization scheme* in which to do the calculations. For all practical purposes, students focusing on LHC physics are only likely to encounter one such scheme, the modified minimal subtraction ($\overline{\text{MS}}$) one already mentioned in the discussion of the definition of the strong coupling in Section 1.4. At the level of these lectures, we shall therefore not elaborate further on this choice here.

We note that factorization can also be applied multiple times, to break up a complicated calculation into simpler pieces that can be treated as approximately independent. This will be very useful when dealing with successive emissions in a parton shower, section 3.2, or when factoring off decays of long-lived particles from a hard production process, section 3.4.

We round off the discussion of factorization by mentioning a few caveats the reader should be aware of. (See [52] for a more technical treatment.)

Firstly, the proof only applies to the first term in an operator product expansion in “twist” = mass dimension - spin. Since operators with higher mass dimensions are suppressed by the hard scale to some power, this leading twist approximation becomes exact in the limit $Q \rightarrow \infty$, while at finite Q it neglects corrections of order

$$\text{Higher Twist : } \frac{[\ln(Q^2/\Lambda^2)]^{m < 2n}}{Q^{2n}} \quad (n = 2 \text{ for DIS}) . \quad (43)$$

In section 5, we shall discuss some corrections that go beyond this approximation, in the context of multiple parton-parton interactions.

Secondly, the proof only really applies to inclusive cross sections in DIS [51] and in Drell-Yan [55]. For all other hadron-initiated processes, factorization is an ansatz. For a general hadron-hadron process, we write the assumed factorizable cross section as:

$$d\sigma_{h_1 h_2} = \sum_{i,j} \int_0^1 dx_i \int_0^1 dx_j \sum_f \int d\Phi_f f_{i/h_1}(x_i, \mu_F^2) f_{j/h_2}(x_j, \mu_F^2) \frac{d\hat{\sigma}_{ij \rightarrow f}}{dx_i dx_j d\Phi_f} . \quad (44)$$

Note that, if $d\hat{\sigma}$ is divergent (as, e.g., Rutherford scattering is) then the integral over $d\Phi_f$ must be regulated, e.g. by imposing some explicit minimal transverse-momentum cut and/or other phase-space restrictions.

2.2 Parton Densities

The parton density function, $f_{i/h}(x, \mu_F^2)$, represents the effective density of partons of type/flavor i , as a function of the momentum fraction¹⁴ x_i , when a hadron of type h is probed at the factorization scale μ_F . The PDFs are non-perturbative functions which are not a priori calculable, but a perturbative differential equation governing their evolution with μ_F can be obtained by requiring that physical scattering cross sections, such as the one for DIS in equation (42), be independent of μ_F to the calculated orders [56]. The resulting *renormalization group equation* (RGE) is called the DGLAP¹⁵ equation and can be used to “run” the PDFs from one perturbative resolution scale to another (its evolution kernels are the same as those used in parton showers, to which we return in section 3.2).

This means that we only need to determine the form of the PDF as a function of x a single (arbitrary) scale, μ_0 . We can then get its form at any other scale μ_F by simple RGE evolution.

¹⁴Recall: the x fraction is defined in equation (41).

¹⁵DGLAP: Dokshitzer-Gribov-Lipatov-Altarelli-Parisi [56–58].

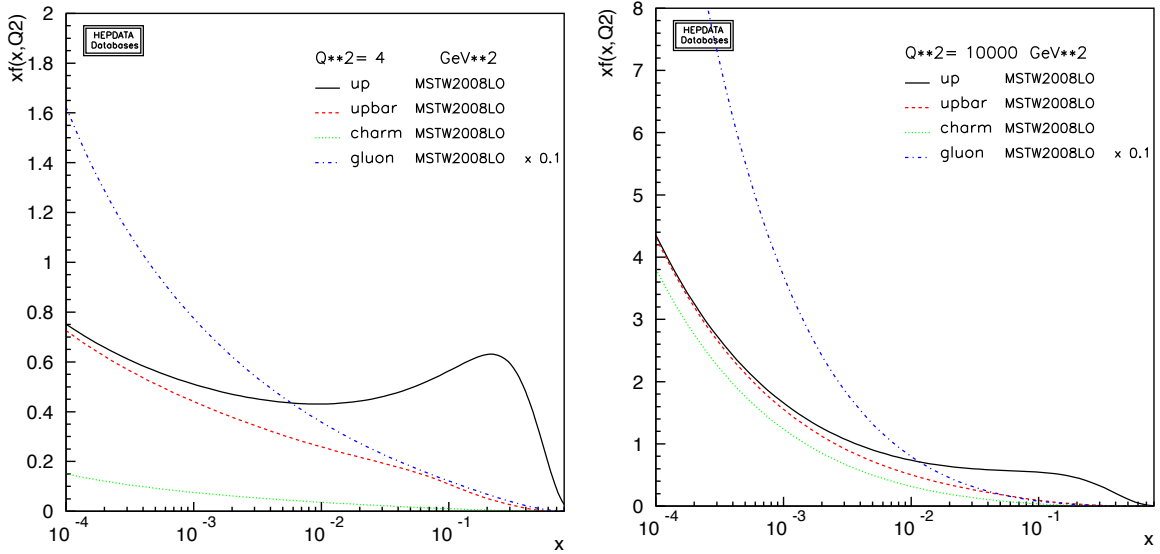


Figure 9: Illustration of the change of the u (black), \bar{u} (red, dashed), c (green, dotted), and g (blue, dot-dashed) distributions, from $Q = \mu_F = 2 \text{ GeV}$ (left) to $Q = \mu_F = 100 \text{ GeV}$ (right). Note that a factor 0.1 has been applied to the gluon distribution. Plots made using the HEPDATA online tool [64].

In the context of PDF fits (constraining the form of the PDF functions by fitting cross sections to experimental data, e.g., from DIS [59, 60], Drell-Yan [61, 62], and $pp \rightarrow \text{jets}$ [63]), the reference scale μ_0 is usually taken to be relatively low, of order one or a few GeV.

The behavior of the PDFs as we evolve μ_F from a low scale, 2 GeV, to a high one, 100 GeV, is illustrated in figure 9, for the MSTW¹⁶ 2008 LO¹⁷ PDF set [65]. At low $Q = \mu_F = 2 \text{ GeV}$ (left), the proton structure is dominated by a few hard quarks (a “valence bump” is clearly visible around $x \sim 0.2$), while at higher scales $Q = 100 \text{ GeV}$ (right) we predominantly resolve fluctuations within fluctuations, yielding increasingly large gluon- and sea-quark distributions with rather small x values, while the valence quarks play a progressively smaller role.

We note that different collaborations, like CTEQ, MSTW, NNPDF, etc., use different ansätze for the form of $f(x, \mu_0^2)$. They may also include different data in the fits, and/or treat or weight the data differently. Thus, results from different groups may not always be mutually compatible. An example is given in figure 10, which shows the difference between the CTEQ6L1 gluon PDF [66] (red dashed) and the MSTW 2008 LO one [65], normalized to MSTW (which would thus be a flat line at zero). The y axis shows the relative difference between the sets, in per cent. Also shown are the 90% CL contours computed from the uncertainty variations included in the MSTW 2008 LO set (black). Using only the MSTW uncertainty band, one would arrive at an estimated $\sim 5\%$ uncertainty over most of the x range, while including the CTEQ6L1 set would increase that to $\sim 10\%$. At NLO, this discrepancy is reduced, but not removed. A significant effort is currently being undertaken within the PDF community to agree on common, and more comprehensive, ways of defining PDF uncertainty bands [63, 67]. This

¹⁶MSTW: Martin-Stirling-Thorne-Watt.

¹⁷The “LO” means that the fit was performed using LO matrix elements in the cross section formulae.

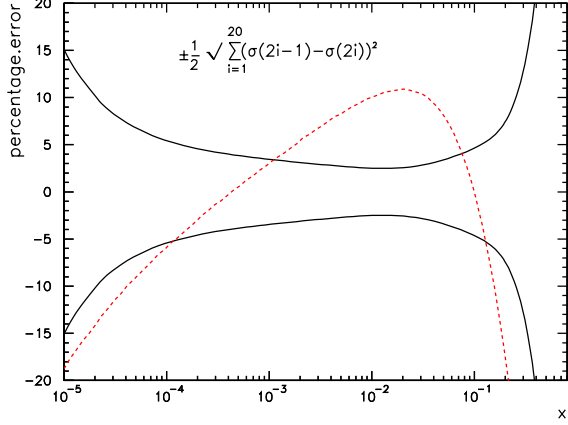


Figure 10: Illustration of the difference between the MSTW 2008 and CTEQ6 LO gluon PDFs at $\mu_F = 10$ GeV. All curves are normalized to the central MSTW 2008 prediction. The black solid lines show the 90% CL MSTW variations, while the dashed red line shows the CTEQ6L1 distribution.

is complicated due to the different ways of defining $f(x, \mu_0^2)$ and due to the experimental data sets not always being fully compatible with one another. For the time being, it is recommended to try at least sets from two different groups, for a comprehensive uncertainty estimate.

Occasionally, the words *structure functions* and *parton densities* are used interchangeably. However, there is an important distinction between the two, which we find often in (quantum) physics: the former is a physical observable used to parametrize the DIS cross sections (see e.g. [4]), while the latter is a “fundamental” quantity extracted from it. In particular, since the parton densities are not, themselves, physically observable, they can only be defined within a specific factorization scheme, order by order in perturbation theory. The only exception is at leading order, at which they have the simple physical interpretation of parton number densities. When going to higher orders, we tend to keep the simple intuitive picture from LO in mind, but one should be aware that the fundamental relationship between PDFs and measured quantities is now more complicated (due to the interplay between the PDFs and the real and virtual corrections to the LO cross section), and that the parton densities no longer have a clear probabilistic interpretation starting from NLO.

The reader should also be aware that there is some ambiguity whether NLO PDFs should be used for LO calculations. In principle, the higher-order PDFs are better constrained and the difference between, e.g., an NLO and an LO set should formally be beyond LO precision, so that one might be tempted to simply use the highest-order available PDFs for any calculation. However, higher-order terms can sometimes be absorbed, at least partially, into effective lower-order coefficients. In the context of PDFs, the fit parameters of lower-order PDFs will attempt to compensate for missing higher-order contributions in the matrix elements. To the extent those higher-order contributions are *universal*, this is both desirable and self-consistent. This leads to some typical qualitative differences between LO and NLO PDFs, illustrated in figure 11: NLO PDFs tend to be smaller at low x and slightly larger at high x , than LO ones. Thus, it is quite possible that using an NLO PDF in conjunction with LO matrix elements can give a worse agreement with data than LO PDFs do.

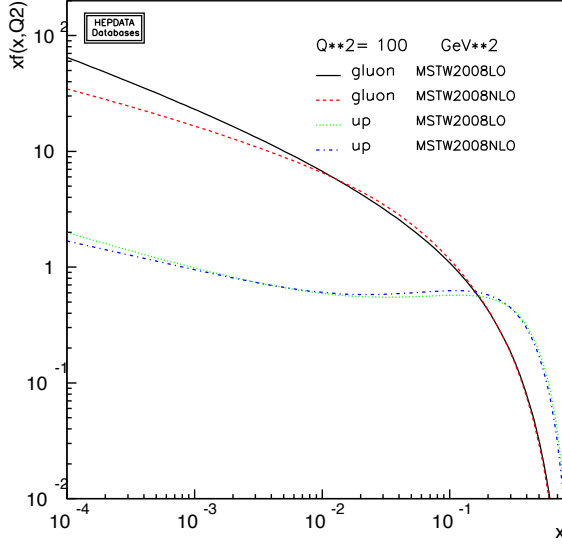


Figure 11: Illustration of the change between PDF fits using LO and NLO matrix elements: the g distribution at LO (black) and NLO (red, dashed), and the u distribution at LO (green, dotted) and NLO (blue, dot-dashed), for the MSTW 2008 PDF sets [65], at $Q = \mu_F = 10$ GeV. Plots made using the HEPDATA online tool [64].

Finally, another oft-raised question concerns which PDF sets to use for the parton-shower evolution in Monte Carlo generators. Importantly, the equations driving the initial-state showers in Monte Carlo models are only sensitive to *ratios* of PDFs [68]. Since the shower evolution typically only has leading-logarithmic (LL) precision, it should be theoretically consistent to use any (LO or better) PDF set to drive the evolution. However, similarly to above, there will be subleading differences between different choices, and one is justified in worrying about the level of physical effects that could be generated. Unfortunately, there is currently no way to ensure 100% self-consistency. Since PDF fits are not done with MC codes, but instead use analytical resummation models (see, e.g., the TASI lectures by Sterman [52]), which are not identical to their MC counterparts, the PDF fits are essentially “tuned” to a slightly different resummation than that incorporated in a given MC model. In practice, not much is known about the size and impact of this ambiguity [69]. Known differences include: the size of phase space (purely collinear massless PDF evolution vs. the finite-transverse-momentum massive MC phase space), the treatment of momentum conservation and recoil effects, additional higher-order effects explicitly or implicitly included in the MC evolution, choice of renormalization scheme and scale, and, for those MC algorithms that do not rely on collinear (DGLAP, see [4]) splitting kernels (e.g., the various kinds of dipole evolution algorithms, see [70]), differences in the effective factorization scheme.

As a baseline, we recommend simply using whatever PDF set the given MC model was originally tuned with, since this should de facto (by fitting the available data) reabsorb as much of the inconsistency as possible. Furthermore, it should be emphasized that underlying-event and minimum-bias models based on multi-parton interactions (see section 5.2) usually make the explicit assumption that the PDFs can be interpreted as physical number densities even down to very low Q and x , a property which is generally only true for LO PDFs. It must

therefore be strongly discouraged to use (N)NLO PDF sets in this context.

2.3 Fixed-Order QCD

Consider the production of an arbitrary final state, F (e.g., a Higgs boson, a $t\bar{t}$ pair, etc). Schematically, we may express the (perturbative) all-orders differential cross section for an observable \mathcal{O} , in the following way:

$$\frac{d\sigma_F}{d\mathcal{O}} \Big|_{\text{ME}} = \underbrace{\sum_{k=0}^{\infty} \int d\Phi_{F+k} \left(\underbrace{\sum_{\ell=0}^{\infty} \mathcal{M}_{F+k}^{(\ell)} \right)^2 \delta(\mathcal{O} - \mathcal{O}(\Phi_{F+k}))}_{\Sigma \text{ legs}} , \quad (45)$$

where, for compactness, we have suppressed all PDF and luminosity normalization factors. $\mathcal{M}_{F+k}^{(\ell)}$ is the amplitude for producing F in association with k additional final-state partons, “legs”, and with ℓ additional loops. The sums start at $k = 0$ and $\ell = 0$, corresponding to the Leading Order for producing F , while higher terms represent real and virtual corrections, respectively.

The purpose of the δ function is to project out hypersurfaces of constant value of \mathcal{O} in the full $d\Phi_{F+k}$ phase space, with $\mathcal{O}(\Phi_{F+k})$ a function that defines \mathcal{O} evaluated on each specific momentum configuration, Φ_{F+k} . (Without the δ function, the formula would give the total integrated cross section, instead of the cross section differentially in \mathcal{O} .)

We recover the various fixed-order truncations of perturbative QCD (pQCD) by limiting the nested sums in equation (45) to include only specific values of $k + \ell$. Thus,

$$\begin{aligned} k = 0, \ell = 0 &\implies \text{Leading Order (usually tree-level) for } F \text{ production} \\ k = n, \ell = 0 &\implies \text{Leading Order for } F + n \text{ jets} \\ k + \ell \leq n, &\implies \text{N}^n \text{LO for } F \text{ (includes N}^1 \text{ LO for } F + 1 \text{ jet, N}^2 \text{ LO for } F + 2 \text{ jets, and so on up to LO for } F + n \text{ jets).} \end{aligned}$$

For $k \geq 1$, we are not considering inclusive F production; instead, we are considering the process $F + k$ jets. If we simply integrate over all momenta, as implied by the integration over $d\Phi_{F+k}$ in equation (45), we would be including configurations in which one or more of the k partons are collinear or soft. Such configurations are infrared divergent in QCD and hence must be regulated. Since we talk about *collinear* and *soft* divergences (the origins of which will be discussed in more detail in sections 2.4 and 3.2), cuts on *angles* and *energies* and/or cuts on combinations, like *transverse momenta*, can be used to cut away the problematic regions of phase space.

Recall, however, that pQCD is approximately scale invariant. This implies that a regularization cut on a dimensionful quantity, like energy or transverse momentum, should be formulated as a *ratio* of scales, rather than as an absolute number. For example, a jet with $p_T = 50$ GeV would be considered hard and well-separated if produced in association with an ordinary Z boson (with hard scale $M_Z = 91.2$ GeV), while the same jet would be considered soft if produced in association with a 900-GeV Z' boson (see [25, 26] for more explicit examples).

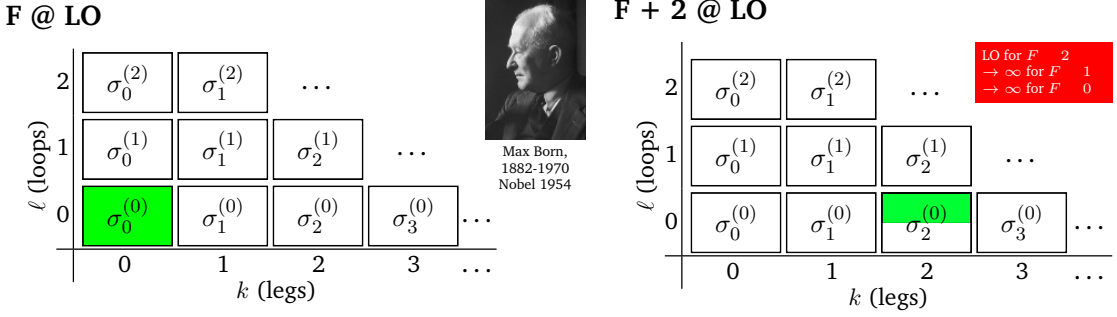


Figure 12: Coefficients of the perturbative series covered by LO calculations. *Left:* F production at lowest order. *Right:* $F + 2$ jets at LO, with the half-shaded box illustrating the restriction to the region of phase space with exactly 2 resolved jets. The total power of α_s for each coefficient is $n = k + \ell$. (Photo of Max Born from nobelprize.org).

The essence of the point is that, if the regularization scale is taken too low, logarithmic enhancements of the type

$$\alpha_s^n \ln^{m \leq 2n} \left(\frac{Q_F^2}{Q_k^2} \right) \quad (46)$$

will generate progressively larger corrections, order by order, which will spoil any fixed-order truncation of the perturbative series. Here, Q_F is the hard scale associated with the process under consideration, while Q_k is the scale associated with an additional parton, k .

A good rule of thumb is that if $\sigma_{k+1} \approx \sigma_k$ (at whatever order you are calculating), then the perturbative series is converging too slowly for a fixed-order truncation of it to be reliable. For fixed-order perturbation theory to be applicable, you must place your cuts on the hard process such that $\sigma_{k+1} \ll \sigma_k$. In the discussion of parton showers in Section 3.2, we shall see how the region of applicability of perturbation theory can be extended.

The virtual amplitudes, for $\ell \geq 1$, are divergent for any point in phase space. However, as encapsulated by the famous KLN theorem [71, 72], unitarity (which essentially expresses probability conservation) puts a powerful constraint on the IR divergences¹⁸, forcing them to cancel exactly against those coming from the unresolved real emissions that we had to cut out above, order by order, making the complete answer for fixed $k + \ell = n$ finite¹⁹. Nonetheless, since this cancellation happens between contributions that formally live in different phase spaces, a main aspect of loop-level higher-order calculations is how to arrange for this cancellation in practice, either analytically or numerically, with many different methods currently on the market. We shall discuss the idea behind subtraction approaches in section 2.4.

A convenient way of illustrating the terms of the perturbative series that a given matrix-element-based calculation includes is given in figure 12. In the left-hand pane, the shaded box corresponds to the lowest-order “Born-level” matrix element squared. This coefficient is non-singular and hence can be integrated over all of phase space, which we illustrate by letting the shaded area fill all of the relevant box. A different kind of leading-order calculation

¹⁸The loop integrals also exhibit UV divergences, but these are dealt with by renormalization.

¹⁹Formally, the KLN theorem states that the sum over degenerate quantum states is finite. In context of fixed-order perturbation theory, this is exemplified by states with infinitely collinear and/or soft radiation being degenerate with the corresponding states with loop corrections; they cannot be told apart by any physical observable.

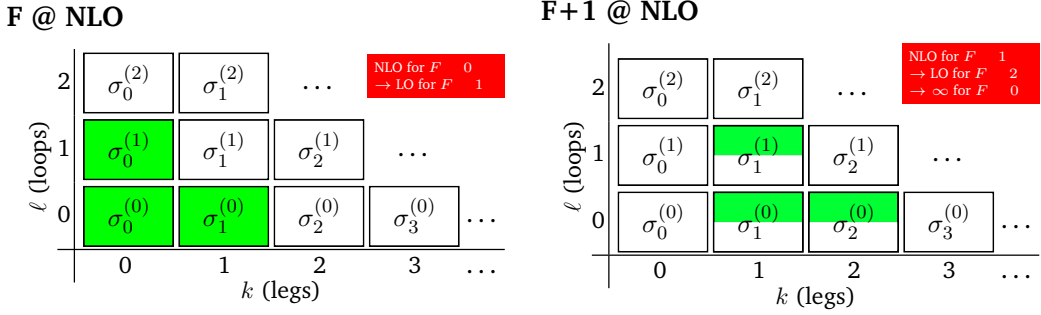


Figure 13: Coefficients of the perturbative series covered by NLO calculations. *Left:* F production at NLO. *Right:* $F + 1$ jet at NLO, with half-shaded boxes illustrating the restriction to the region of phase space with exactly 1 resolved jet. The total power of α_s for each coefficient is $n = k + \ell$.

is illustrated in the right-hand pane of figure 12, where the shaded box corresponds to the lowest-order matrix element squared for $F + 2$ jets. This coefficient diverges in the part of phase space where one or both of the jets are unresolved (i.e., soft or collinear), and hence integrations can only cover the hard part of phase space, which we reflect by only shading the upper half of the relevant box.

Figure 13 illustrates the inclusion of NLO virtual corrections. To prevent confusion, first a point on notation: by $\sigma_0^{(1)}$, we intend

$$\sigma_0^{(1)} = \int d\Phi_0 2\text{Re}[\mathcal{M}_0^{(1)} \mathcal{M}_0^{(0)*}] , \quad (47)$$

which is of order α_s relative to the Born level. Compare, e.g., with the expansion of equation (45) to order $k + \ell = 1$. In particular, $\sigma_0^{(1)}$ should *not* be confused with the integral over the 1-loop matrix element squared (which would be of relative order α_s^2 and hence forms part of the NNLO coefficient $\sigma_0^{(2)}$). Returning to figure 13, the unitary cancellations between real and virtual singularities imply that we can now extend the integration of the real correction in the left-hand pane over all of phase space, while retaining a finite total cross section,

$$\begin{aligned} \sigma_0^{\text{NLO}} &= \int d\Phi_0 |\mathcal{M}_0^{(0)}|^2 + \int d\Phi_1 |\mathcal{M}_1^{(0)}|^2 + \int d\Phi_0 2\text{Re}[\mathcal{M}_0^{(1)} \mathcal{M}_0^{(0)*}] \\ &= \sigma_0^{(0)} + \sigma_1^{(0)} + \sigma_0^{(1)} , \end{aligned} \quad (48)$$

with $\sigma_0^{(0)}$ the finite Born-level cross section, and the positive divergence caused by integrating the second term over all of phase space is canceled by a negative one coming from the integration over loop momenta in the third term. One method for arranging the cancellation of singularities — subtraction — is discussed in section 2.4.

However, if our starting point for the NLO calculation is a process which already has a non-zero number of hard jets, we must continue to impose that at least that number of jets

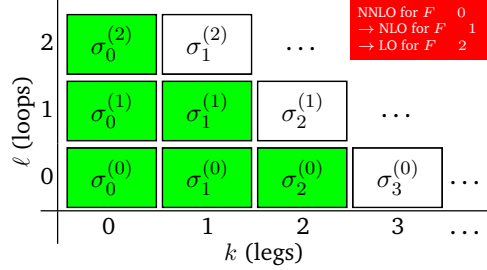
F @ NNLO

Figure 14: Coefficients of the perturbative series covered by an NNLO calculation. The total power of α_s for each coefficient is $n = k + \ell$. Green shading represents the full perturbative coefficient at the respective k and ℓ .

must still be resolved in the final-state integrations,

$$\begin{aligned} \sigma_1^{\text{NLO}}(p_{\perp \min}) &= \int_{p_{\perp} > p_{\perp \min}} d\Phi_1 |\mathcal{M}_1^{(0)}|^2 + \int_{p_{\perp 1} > p_{\perp \min}} d\Phi_2 |\mathcal{M}_2^{(0)}|^2 + \int_{p_{\perp} > p_{\perp \min}} d\Phi_1 2\text{Re}[\mathcal{M}_1^{(1)} \mathcal{M}_1^{(0)*}] \\ &= \sigma_1^{(0)}(p_{\perp} > p_{\perp \min}) + \sigma_2^{(0)}(p_{\perp 1} > p_{\perp \min}) + \sigma_1^{(1)}(p_{\perp} > p_{\perp \min}), \end{aligned} \quad (49)$$

where the restriction to at least one jet having $p_{\perp} > p_{\perp \min}$ has been illustrated in the right-hand pane of figure 13 by shading only the upper part of the relevant boxes. In the second term in equation (49), the notation $p_{\perp 1}$ is used to denote that the integral runs over the phase space in which at least one “jet” (which may consist of one or two partons) must be resolved with respect to $p_{\perp \min}$. Here, therefore, an explicit dependence on the algorithm used to define “a jet” enters for the first time. This is discussed in more detail in the 2009 ESHEP lectures by Salam [5].

To extend the integration to cover also the case of 2 unresolved jets, we must combine the left- and right-hand parts of figure 13 and add the new coefficient

$$\sigma_0^{(2)} = |\mathcal{M}_0^{(1)}|^2 + 2\text{Re}[\mathcal{M}_0^{(2)} \mathcal{M}_0^{(0)*}], \quad (50)$$

as illustrated by the diagram in figure 14.

2.4 The Subtraction Idea

According to the KLN theorem, the IR singularities coming from integrating over collinear and soft real-emission configurations should cancel, order by order, by those coming from the IR divergent loop integrals. This implies that we should be able to rewrite e.g. the NLO cross section, equation (48), as

$$\sigma^{\text{NLO}} = \sigma^{\text{Born}} + \text{Finite} \left\{ \int d\Phi_{F+1} |\mathcal{M}_{F+1}^{(0)}|^2 \right\} + \text{Finite} \left\{ \int d\Phi_F 2\text{Re}[\mathcal{M}_F^{(1)} \mathcal{M}_F^{(0)*}] \right\} \quad (51)$$

with the second and third terms having had their common (but opposite-sign) singularities canceled out and some explicitly finite quantities remaining.

The first step towards this goal is to classify all IR singularities that could appear in the amplitudes. We know that the IR limits are universal, so they can be classified using a set of process-independent functions that only has to be worked out once and for all. A widely used such set of functions are the *Catani-Seymour* (CS) dipole ones [73, 74], a method which by now has even been partially automated [75, 76]. Here, we shall instead use a formalism based on *antennae* [78–80]. The distinction between the two is basically that one antenna is made up of two dipole “ends”, hence the antenna formalism tends to generate somewhat fewer terms. At NLO, however, there is no fundamental incompatibility — the antennae we use here can always be partitioned into two dipole ends, if so desired. (Note: only the antenna method has been successfully generalized to NNLO [81, 82]. Other NNLO techniques, not covered here, are *sector decomposition*, see [83, 84], and the generic formalism for hadroproduction of colorless states presented in [85].)

At NLO, the idea with subtraction is thus to rewrite the NLO cross section by adding and subtracting a simple function, $d\sigma_S$, that encapsulates all the IR limits,

$$\begin{aligned} \sigma^{\text{NLO}} &= \sigma^{\text{Born}} + \underbrace{\int d\Phi_{F+1} \left(|\mathcal{M}_{F+1}^{(0)}|^2 - d\sigma_S^{\text{NLO}} \right)}_{\text{Finite by Universality}} \\ &\quad + \underbrace{\int d\Phi_F 2\text{Re}[\mathcal{M}_F^{(1)} \mathcal{M}_F^{(0)*}] + \int d\Phi_{F+1} d\sigma_S^{\text{NLO}}}_{\text{Finite by KLN}} . \end{aligned} \quad (52)$$

The task now is to construct a suitable form for $d\sigma_S$. A main requirement is that it should be sufficiently simple that the integral in the last term can be done analytically, in dimensional regularization, so that the IR poles it generates can be canceled against those from the loop term.

To build a set of universal terms that parametrize the IR singularities of any amplitude, we start from the observation that gauge theory amplitudes factorize in the *soft limit*, as follows:

$$|\mathcal{M}_{F+1}(\dots, i, j, k, \dots)|^2 \xrightarrow{j_g \rightarrow 0} g_s^2 N_C \begin{pmatrix} 2s_{ik} & 2m_i^2 & 2m_k^2 \\ s_{ij}s_{jk} & s_{ij}^2 & s_{jk}^2 \end{pmatrix} |\mathcal{M}_F(\dots, i, k, \dots)|^2 , \quad (53)$$

where parton j is a soft gluon, partons i, j , and k form a chain of color-space index contractions (we say they are *color-connected*), g_s is the strong coupling, and the terms in parenthesis are called the *soft eikonal factor*. We here show it including mass corrections, which appear if i and k have non-zero rest masses, with the invariants s_{ab} then defined as

$$s_{ab} \equiv 2p_a \cdot p_b = (p_a + p_b)^2 - m_a^2 - m_b^2 . \quad (54)$$

The color factor, N_C , is valid for the leading-color contribution, regardless of whether the i and k partons are quarks or gluons. At subleading color, an additional soft-eikonal factor identical to the one above but with a color factor proportional to $1/N_C$ arises for each $q\bar{q}$ pair combination. This, e.g., modifies the effective color factor for $q\bar{q} \rightarrow qg\bar{q}$ from N_C to $N_C(1 - 1/N_C) = 2C_F$, in agreement with the color factor for quarks being C_F rather than C_A .

Similarly, amplitudes also factorize in the *collinear limit* (partons i and j parallel, so $s_{ij} \rightarrow 0$), in which the eikonal factor above is replaced by the famous Dokshitzer-Gribov-Lipatov-Altarelli-Parisi (DGLAP) splitting kernels [56–58], which were already mentioned in

section 2.2, in the context of PDF evolution. They are also the basis of conventional parton-shower models, to which we return in section 3.2.

Essentially, what antenna functions, CS dipoles, and the like, all do, is to combine the soft (eikonal) and collinear (Altarelli-Parisi) limits into one universal set of functions that achieve the correct limiting behavior for *both* soft and collinear radiation. To give an explicit example, the *antenna function* for gluon emission from a color-connected $q\bar{q}$ pair can be derived from the matrix elements squared for the process $Z^0 \rightarrow q\bar{q} \rightarrow qg\bar{q}$ [86],

$$\frac{|\mathcal{M}(Z^0 \rightarrow q_i g_j \bar{q}_k)|^2}{|\mathcal{M}(Z^0 \rightarrow q_I \bar{q}_K)|^2} = g_s^2 2C_F \left[\underbrace{\frac{2s_{ik}}{s_{ij}s_{jk}}}_{\text{eikonal}} + \underbrace{\frac{1}{s_{IK}} \left(\frac{s_{jk}}{s_{ij}} + \frac{s_{ij}}{s_{jk}} \right)}_{\text{collinear}} \right], \quad (55)$$

where we have neglected mass corrections (see [87, 88] for massive expressions) and we recognize the universal eikonal soft factor from equation (53) in the first term. The two additional terms are less singular, and are required to obtain the correct collinear (Altarelli-Parisi) limits as $s_{ij} \rightarrow 0$ or $s_{jk} \rightarrow 0$.

However, since the singularity structure is universal, we could equally well have used the process $H^0 \rightarrow q\bar{q} \rightarrow qg\bar{q}$ to derive the antenna function. Our antenna function would then have come out as [88],

$$\frac{|\mathcal{M}(H^0 \rightarrow q_i g_j \bar{q}_k)|^2}{|\mathcal{M}(H^0 \rightarrow q_I \bar{q}_K)|^2} = g_s^2 2C_F \left[\underbrace{\frac{2s_{ik}}{s_{ij}s_{jk}}}_{\text{eikonal}} + \underbrace{\frac{1}{s_{IK}} \left(\frac{s_{jk}}{s_{ij}} + \frac{s_{ij}}{s_{jk}} \right)}_{\text{collinear}} + \underbrace{\frac{2}{s_{IK}}}_{\text{finite}} \right], \quad (56)$$

where the additional term $2/s_{IK}$ is non-singular (“finite”) over all of phase space. Thus, we here see an explicit example that the singularities are process-independent while the non-singular terms are process-dependent. Since we add and subtract the same term in equation (52), the final answer does not depend on the choice of finite terms. We say that they correspond to different *subtraction schemes*. One standard antenna subtraction scheme, which uses the antenna function defined in equation (55) rather than the one in equation (56), is the Gehrmann-Gehrmann-de Ridder-Glover (GGG) one, given in [80].

If there is more than one color antenna in the Born-level process, the form of $d\sigma_S$ is obtained as a sum over terms, each of which captures one specific soft limit and either all or “half” of a collinear one, depending on the specific scheme and the type of parton,

$$d\sigma_S = \sum_j A_{IK \rightarrow ijk} |\mathcal{M}_F(\dots, I, K, \dots)|^2, \quad (57)$$

with the sum running over all singular $3 \rightarrow 2$ “clusterings” of the $(F+1)$ -parton state to F partons. An analysis of the different ways of partitioning the collinear singularity of gluons among neighboring antenna is beyond the scope of this introduction, but useful discussions can be found in [89–91].

2.5 Infrared Safety

A further requirement for being able to perform calculations within perturbative QCD is that the observable be *infrared safe*. Note: by “infrared”, we here mean any limit that involves a

low scale (i.e., any non-UV limit), without regard to whether it is collinear or soft.

The property of infrared safety defines a special class of observables which have *minimal sensitivity* to long-distance physics, and which can be consistently computed in pQCD. An observable is infrared safe if:

1. (*Safety against soft radiation*): Adding any number of infinitely soft particles should not change the value of the observable.
2. (*Safety against collinear radiation*): Splitting an existing particle up into two comoving particles, with arbitrary fractions z and $1 - z$, respectively, of the original momentum, should not change the value of the observable.

If both of these conditions are satisfied, any long-distance non-perturbative corrections will be suppressed by the ratio of the long-distance scale to the short-distance one to some (observable-dependent) power, typically

$$\text{IR Safe Observables: IR corrections} \propto \frac{Q_{\text{IR}}^2}{Q_{\text{UV}}^2} \quad (58)$$

where Q_{UV} denotes a generic hard scale in the problem, and $Q_{\text{IR}} \sim \Lambda_{\text{QCD}} \sim \mathcal{O}(1 \text{ GeV})$.

Due to this *power suppression*, IR safe observables are not so sensitive to our lack of ability to solve the strongly coupled IR physics, unless of course we go to processes for which the relevant hard scale, Q_{UV} , is small (such as minimum-bias, soft jets, or small-scale jet substructure). Even when a high scale is present, however, as in resonance decays, jet fragmentation, or underlying-event-type studies, infrared safety only guarantees us that infrared corrections are small, not that they are zero. Thus, ultimately, we run into a precision barrier even for IR safe observables, which only a reliable understanding of the long-distance physics itself can address.

To constrain models of long-distance physics, one needs infrared *sensitive* observables. Hence it is not always the case that infrared safe observables are preferable — the purpose decides the tool. Instead of the suppressed corrections above, the perturbative prediction for such observables contains logarithms of the type already encountered in equation (46),

$$\text{IR Sensitive Observables: IR Corrections} \propto \alpha_s^n \log^{m \leq 2n} \left(\frac{Q_{\text{UV}}^2}{Q_{\text{IR}}^2} \right), \quad (59)$$

which grow increasingly large as $Q_{\text{IR}}/Q_{\text{UV}} \rightarrow 0$. As an example, consider such a fundamental quantity as particle multiplicities (= number of particles); in the absence of nontrivial infrared effects, the number of partons tends logarithmically to infinity as the IR cutoff is lowered. Similarly, the distinction between a charged and a neutral pion only occurs in the very last phase of hadronization, and hence observables that only include charged tracks, for instance, are always IR sensitive²⁰.

Two important categories of infrared safe observables that are widely used are *event shapes* and *jet algorithms*. Jet algorithms are perhaps nowhere as pedagogically described as in the 2009 ESHEP lectures by Salam [5, Chapter 5]. Event shapes in the context of hadron colliders

²⁰This remains true in principle even if the tracks are clustered into jets, although the energy clustered in this way does provide a lower bound on Q_{UV} in the given event, since “charged + neutral > charged-only”.

have not yet been as widely explored, but the basic phenomenology is introduced also by Salam and collaborators in [93], with first measurements reported by CMS and ATLAS [94, 95] and a proposal to use them also for the characterization of soft-QCD (“minimum-bias”) events put forth in [96].

Let us here merely emphasize that the real reason to prefer infrared safe jet algorithms over unsafe ones is not that they necessarily give very different or “better” answers in the experiment — experiments are infrared safe by definition, and the difference between infrared safe and unsafe algorithms may not even be visible when running the algorithm on experimental data — but that it is only possible to compute perturbative QCD predictions for the infrared safe ones. Any measurement performed with an infrared unsafe algorithm can only be compared to calculations that include a detailed hadronization model. This both limits the number of calculations that can be compared to and also adds an a priori unknown sensitivity to the details of the hadronization description, details which one would rather investigate and constrain separately, in the framework of more dedicated fragmentation studies.

For LHC phenomenology, the preferred IR safe algorithm for jet reconstruction is currently the *anti- kT* one [97], with size parameter R varying between 0.4 and 0.7, though larger sizes can be motivated in certain contexts, e.g., to look for highly energetic jets and/or the boosted decay products of high-mass objects [30, 98]. This algorithm generates circular-looking jets, so subtracting off the energy believed to be associated with the *underlying event* (UE, see section 5.2) is particularly simple.

For jet substructure, typically either the “ kT ” or “Cambridge/Aachen” algorithms are used, see e.g. [30, 98]. The clustering measures used in these algorithms more closely mimic the singularity structure of QCD bremsstrahlung and they are therefore particularly well suited to “unravel” a tree of QCD branchings [5], such as a parton shower generates. The Cambridge/Aachen algorithm may also be used to characterize the underlying event, see [99].

3 Monte Carlo Event Generators

In this section, we discuss the physics of Monte Carlo event generators and their mathematical foundations, at an introductory level. We shall attempt to convey the main ideas as clearly as possible without burying them in an avalanche of technical details. References to more detailed discussions are included where applicable. We assume the reader is already familiar with the contents of the preceding section on hard processes.

The task of a Monte Carlo event generator is to calculate everything that happens in a high-energy collision, from the hard short-distance physics to the long wavelengths of hadronisation and hadron decays. Obviously, this requires some compromises to be made. General-purpose generators like HERWIG [48, 100, 101], PYTHIA [102, 103], and SHERPA [104], start from low-order (LO or NLO) descriptions of the perturbative hard physics and then attempt to include the “most significant” corrections, such as higher-order matrix-element corrections and parton showers, resonance decays and finite-width effects, underlying event, beam remnants, hadronisation, and hadron decays. Each of them had slightly different origins, which carries through to the emphasis placed on various physics aspects today:

- PYTHIA. Successor to JETSET (begun in 1978). Originated in hadronisation studies. Main feature: the Lund string fragmentation model.
- HERWIG. Successor to EARWIG (begun in 1984). Originated in perturbative coherence studies. Main feature: angular-ordered parton showers.
- SHERPA. Begun in 2000. Originated in studies of the matching of hard-emission matrix elements with parton showers. Main feature: CKKW matching.

There is also a large number of more specialised generators, mainly for hard processes within and beyond the SM, a few that offer alternative shower models, and ones specializing in soft-inclusive and/or heavy-ion physics.

An important aspect of contemporary generators is the ability to combine specialised ones with general-purpose ones, via interfaces. The most common interface between partonic hard-process and parton-shower generators is the Les Houches Event File (LHEF) standard, defined in [105, 106] and “spoken” by most modern generator tools. For interfaces to experimental analysis packages (like RIVET [107]) and detector simulations (like GEANT [108]), typically the HepMC standard is used [109].

Hard processes were the topic of section 2. In this section, we shall focus mainly on parton showers, with some brief comments on resonance decays at the end. Section 4 then concerns the matching of matrix elements and parton showers. Finally, models of hadronisation and the underlying event are the topic of section 5.

Several of the discussions below rely on material from the section on Monte Carlo Event Generators in the PDG Review of Particle Physics [31] and on the more comprehensive review by the MCnet collaboration in [6]. The latter also contains brief descriptions of the physics implementations of each of the main general-purpose event generators on the market, together with a guide on how to use (and not use) them in various connections, and a collection of comparisons to important experimental distributions. We highly recommend readers to obtain a copy of that review, as it is the most comprehensive and up-to-date review of event generators currently available. Another useful and pedagogical review on event generators is contained in the 2006 ESHEP lectures by Torbjörn Sjöstrand [50], with a more recent update in [110].

Relative uncertainty with n points	1-Dim	d -Dim	$n_{\text{eval}}/\text{point}$
Trapezoidal Rule	$1/n^2$	$1/n^{2/d}$	2^d
Simpson's Rule	$1/n^4$	$1/n^{4/d}$	3^d
Monte Carlo	$1/\sqrt{n}$	$1/\sqrt{n}$	1

Table 2: Relative uncertainty after n evaluations, in 1 and d dimensions, for two traditional numerical integration methods and stochastic Monte Carlo. The last column shows the number of function evaluations that are required per point, in d dimensions.

3.1 The Monte Carlo Method

A ubiquitous problem in fundamental physics is the following: given a source located some distance from a detector, predict the number of counts that should be observed within the solid angle spanned by the detector (or within a bin of its phase-space acceptance), as a function of the properties of the source, the intervening medium, and the efficiency of the detector. Essentially, the task is to compute integrals of the form

$$N_{\text{Count}}(\Delta\Omega) = \int_{\Omega} d\Omega \frac{d\sigma}{d\Omega}, \quad (60)$$

with $d\sigma$ a differential cross section for the process of interest.

In particle physics, phase space has three dimensions per final-state particle (minus four for overall four-momentum-conservation). Thus, for problems with more than a few outgoing particles, the dimensionality of phase space increases rapidly. At LEP, for instance, the total multiplicity of neutral + charged hadrons (before weak decays) was typically ~ 30 particles, for about 86 dimensions.

The standard 1D numerical-integration methods give very slow convergence rates for higher-dimensional problems. For illustration, a table of convergence rates in 1 and d dimensions is given in table 2, comparing the Trapezoidal (2-point) rule and Simpson's (3-point) rule to random-number-based Monte Carlo. In 1D, the $1/n^2$ convergence rate of the Trapezoidal rule is much faster than the stochastic $1/\sqrt{n}$ of random-number Monte Carlo, and Simpson's rule converges even faster. However, as we go to d dimensions, the convergence rate of the n -point rules all degrade with d (while the number of function evaluations required for each “point” simultaneously increases). The MC convergence rate, on the other hand, remains the simple stochastic $1/\sqrt{n}$, independent of d , and each point still only requires one function evaluation. These are some of the main reasons that MC is the preferred numerical integration technique for high-dimensional problems. In addition, the random phase-space vectors it generates can be re-used in many ways, for instance as input to iterative solutions, to compute many different observables simultaneously, and/or to hand “events” to propagation and detector-simulation codes.

Therefore, virtually all numerical cross section calculations are based on Monte Carlo techniques in one form or another, the simplest being the RAMBO algorithm [111] which can be expressed in about half a page of code and generates a flat scan over n -body phase space²¹.

²¹Strictly speaking, RAMBO is only truly uniform for massless particles. Its massive variant makes up for phase-space biases by returning weighted momentum configurations.



This risk, that convergence is only given with a certain probability, is inherent in Monte Carlo calculations and is the reason why this technique was named after the world's most famous gambling casino. Indeed, the name is doubly appropriate because the style of gambling in the Monte Carlo casino, not to be confused with the noisy and tasteless gambling houses of Las Vegas and Reno, is serious and sophisticated.”

*F. James, “Monte Carlo theory and practice”,
Rept. Prog. Phys. 43 (1980) 1145*

Figure 15: *Left:* The casino in Monaco. *Right:* extract from [11] concerning the nature of Monte Carlo techniques.

However, due to the infrared singularities in perturbative QCD, and due to the presence of short-lived resonances, the functions to be integrated, $|\mathcal{M}_{F+k}|^2$, can be highly non-uniform, especially for large k . This implies that we will have to be clever in the way we sample phase space if we want the integration to converge in any reasonable amount of time — simple algorithms like RAMBO quickly become inefficient for k greater than a few. To address this bottleneck, the simplest step up from RAMBO is to introduce generic (i.e., automated) importance-sampling methods, such as offered by the VEGAS algorithm [112, 113]. This is still the dominant basic technique, although most modern codes do employ several additional refinements, such as several different copies of VEGAS running in parallel (multi-channel integration), to further optimise the sampling. Alternatively, a few algorithms incorporate the singularity structure of QCD explicitly in their phase-space sampling, either by directly generating momenta distributed according to the leading-order QCD singularities, in a sort of “QCD-preweighted” analog of RAMBO, called SARGE [114], or by using all-orders Markovian parton showers to generate them (VINCIA [90, 91, 115]).

The price of using random numbers is that we must generalise our notion of convergence. In calculus, we say that a sequence $\{A\}$ converges to B if an n exists for which the difference $|A_{i>n} - B| < \epsilon$ for any $\epsilon > 0$. In random-number-based techniques, we cannot completely rule out the possibility of very pathological sequences of “dice rolls” leading to large deviations from the true goal, hence we are restricted to say that $\{A\}$ converges to B if an n exists for which the probability for $|A_{i>n} - B| < \epsilon$, for any $\epsilon > 0$, is greater than P , for any $P \in [0, 1]$ [11]. This risk, that convergence is only given with a certain probability, is the reason why Monte Carlo techniques were named after the famous casino in Monaco, illustrated in figure 15.

3.2 Theoretical Basis of Parton Showers

In section 2, we noted two conditions that had to be valid for fixed-order truncations of the perturbative series to be valid: firstly, the strong coupling α_s must be small for perturbation theory to be valid at all. This restricts us to the region in which all scales $Q_i \gg \Lambda_{\text{QCD}}$. We shall maintain this restriction in this section, i.e., we are still considering perturbative QCD.

Secondly, however, in order to be allowed to *truncate* the perturbative series, we had to require $\sigma_{k+1} \ll \sigma_k$, i.e., the corrections at successive orders must become successively smaller, which — due to the enhancements from soft/collinear singular (conformal) dynamics — effectively restricted us to consider only the phase-space region in which all jets are “hard and well-separated”, equivalent to requiring all $Q_i/Q_j \approx 1$. In this section, we shall see how to lift this restriction, extending the applicability of perturbation theory into regions that include scale hierarchies, $Q_i \gg Q_j \gg \Lambda_{\text{QCD}}$, such as occur for soft jets, jet substructure, etc.

In fact, the simultaneous restriction to all resolved scales being larger than Λ_{QCD} and no large hierarchies is extremely severe, if taken at face value. Since we collide and observe hadrons (\rightarrow low scales) while simultaneously wishing to study short-distance physics processes (\rightarrow high scales), it would appear trivial to conclude that fixed-order pQCD is not applicable to collider physics at all. So why do we still use it?

The answer lies in the fact that we actually never truly perform a fixed-order calculation in QCD. Let us repeat the factorised formula for the cross section, equation (??), now inserting also a function, D , to represent the fragmentation of the final-state partons into observable hadrons,

$$\frac{d\sigma}{d\mathcal{O}} = \sum_{i,j} \int_0^1 dx_i dx_j \sum_f \int d\Phi_f f_{i/h_1}(x_i, \mu_F^2) f_{j/h_2}(x_j, \mu_F^2) \frac{d\hat{\sigma}_{ij \rightarrow f}}{d\hat{\mathcal{O}}} D_f(\hat{\mathcal{O}} \rightarrow \mathcal{O}, \mu_F^2), \quad (61)$$

with $\hat{\mathcal{O}}$ denoting the observable evaluated on the partonic final state, and \mathcal{O} the observable evaluated on the hadronic final state, after fragmentation. Although the partonic cross section, $d\hat{\sigma}_{ij \rightarrow f}$, does represent a fixed-order calculation, the parton densities, f_{i/h_1} and f_{j/h_2} , include so-called resummations of perturbative corrections to *all orders* from the initial scale of order the mass of the proton, up to the factorisation scale, μ_F (see section 2.2 and/or the TASI lectures by Sterman [52]). Note that the oft-stated mantra that the PDFs are purely non-perturbative functions is therefore misleading. True, they are defined as essentially non-perturbative functions at some very low scale, $\mu_0 \sim$ a few GeV, but, if μ_F is taken large, they necessarily incorporate a significant amount of perturbative physics as well. On the “fixed-order side”, all we have left to ensure in $d\hat{\sigma}_{ij \rightarrow f}$ is then that there are no large hierarchies remaining between μ_F and the QCD scales appearing in Φ_f . Likewise, in the final state, the fragmentation functions, D_f , include infinite-order resummations of perturbative corrections all the way *from* μ_F down to some low scale, with similar caveats concerning mantras about their non-perturbative nature as for the PDFs.

3.2.1 Step One: Infinite Legs

The infinite-order resummations that are included in objects such as the PDFs and FFs in equation (61) (and in their parton-shower equivalents) rely on some very simple and powerful properties of gauge field theories that were already touched on in section 2. In particular, we saw in section 2.4 that we can represent all the infrared (IR) limits of any NLO amplitude with a set of simple universal functions, based solely on knowing which partons are color-connected (i.e., have color-space index contractions) with one another.

The diagrams in figure 16 show the basic origin of the universal IR singularities of gauge theory amplitudes. On the left is shown a diagram (squared) in which an emission with small s_{ij} interferes with itself. In the collinear limit, $s_{ij} \rightarrow 0$, the propagator of the parent parton,

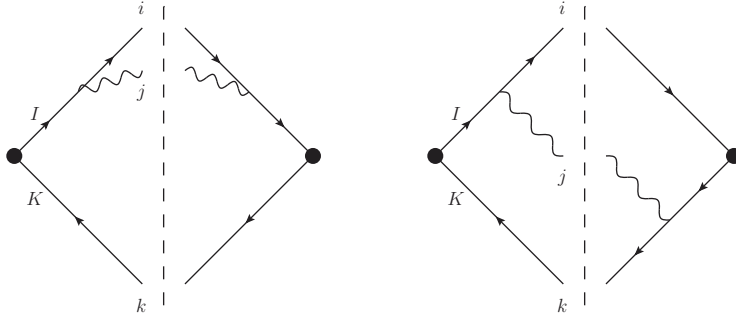


Figure 16: Diagrams (squared) giving rise to collinear (left) and soft (right) singularities.

I , goes on shell; the singularity of the associated propagator factor is the origin of the $1/s_{ij}$ collinear singularities. On the right is shown the interference between a diagram with emission from parton I and one with emission from parton K . The resulting term has propagator singularities when both partons I and K go on shell, which can happen simultaneously if parton j is soft. This generates the $2s_{ik}/(s_{ij}s_{jk})$ soft singularity, also called the soft eikonal factor or the dipole factor.

We now understand the fundamental origin of the IR singularities, why they are universal, and why amplitudes factorise in the soft and collinear limits — the singularities are simply generated by intermediate parton propagators going on shell, which is independent of the nature of the hard process, and hence can be factorised from it.

Thus, for each pair of (massless) color-connected partons I and K in F , the squared amplitude for $F + 1$ gluon, $|\mathcal{M}_{F+1}|^2$, will include a factor

$$|\mathcal{M}_{F+1}|^2 = \underbrace{g_s^2 N_C \left(\frac{2s_{ik}}{s_{ij}s_{jk}} + \text{collinear terms} \right)}_{\text{Antenna Function}} |\mathcal{M}_F|^2 , \quad (62)$$

where $g_s^2 = 4\pi\alpha_s$ is the strong coupling, i and k represent partons I and K after the branching (i.e., they include possible recoil effects) and s_{ij} is the invariant between parton i and the emitted parton, j .

The branching phase space of a color dipole (i.e., a pair of partons connected by a color-index contraction) is illustrated in figure 17. Expressed in the branching invariants, s_{ij} and s_{jk} , the phase space has a characteristic triangular shape, imposed by the relation $s = s_{ij} + s_{jk} + s_{ik}$ (assuming massless partons). Sketchings of the post-branching parton momenta have been inserted in various places in the figure, for illustration. The soft singularity is located at the origin of the plot and the collinear regions lie along the axes.

The collinear terms for a $q\bar{q} \rightarrow qg\bar{q}$ “antenna” are unambiguous and are given in section 2.4. Since gluons are in the adjoint representation, they carry both a color and an anticolor index (one corresponding to the rows and the other to the columns of the Gell-Mann matrices), and there is therefore some ambiguity concerning how to partition collinear radiation among the two antennae they participate in. This is discussed in more detail in [90]. Differences are subleading, however, and for our purposes here we shall consider gluon antenna ends as radiating just like quark ones. The difference between quark and gluon radiation then arise mainly because gluons participate in two antennae, while quarks only participate in one. This

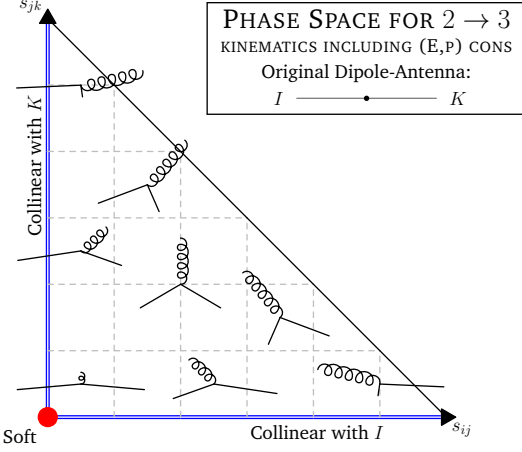


Figure 17: Illustration of the branching phase space for $q\bar{q} \rightarrow qg\bar{q}$, with the original dipole-antenna oriented horizontally, the two parents sharing the transverse component of recoil, and the azimuthal angle ϕ (representing rotations of the emitted parton around the dipole axis) chosen such that the gluon is radiated upwards. From [90].

is related to the difference between the color factors, $C_A \sim 2C_F$.

The problem that plagued the fixed-order truncations in section 2 is clearly visible in equation (62): if we integrate over the entire phase space including the region $s_{ij} \rightarrow 0, s_{jk} \rightarrow 0$, we end up with a double pole. If we instead regulate the divergence by cutting off the integration at some minimal *perturbative cutoff scale* μ_{IR}^2 , we end up with a logarithm squared of that scale. This is a typical example of “large logarithms” being generated by the presence of scale hierarchies. Also note that the precise definition of μ_{IR} is not unique. Any scale choice that properly isolates the singularities from the rest of phase space will do, with some typical choices being, for example, invariant-mass and/or transverse-momentum scales.

Before we continue, it is worth noting that equation (62) is often rewritten in other forms to emphasise specific aspects of it. One such rewriting is thus to reformulate the invariants s_{ij} appearing in it in terms of energies and angles,

$$s_{ij} = 2E_i E_j (1 - \cos \theta_{ij}) . \quad (63)$$

Rewritten in this way, the differentials can be partial-fractioned,

$$\frac{ds_{ij}}{s_{ij}} \frac{ds_{jk}}{s_{jk}} \propto \frac{dE_j}{E_j} \frac{d\theta_{ij}}{\theta_{ij}} + \frac{dE_j}{E_j} \frac{d\theta_{jk}}{\theta_{jk}} . \quad (64)$$

This kind of rewriting enables an intuitively appealing categorisation of the singularities as related to vanishing energies and angles, explaining why they are called *soft* and *collinear*, respectively. Arguments based on this rewriting have led to important insights in QCD. For instance, within the framework of conventional parton showers, it was shown in a sequence of publications (see [116, 117] and references therein) that the destructive interference effects between two colour-connected partons (*coherence*) can be described, on average²², by using

²²Averaged over azimuthal emission angles.

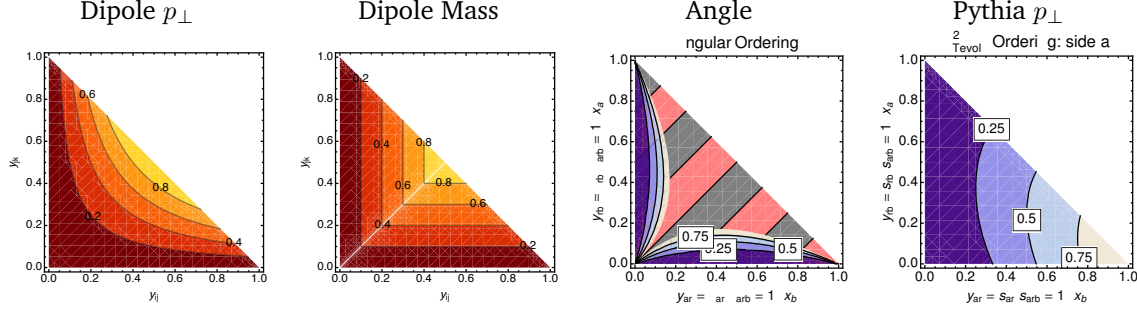


Figure 18: A selection of parton-shower evolution variables, represented as contours over the dipole phase space. Note: the right-most variable corresponds to evolution of only one of the parents, the one with no collinear singularity along the bottom of the plot.

the opening angle of the emissions as the shower ordering variable. One should still keep in mind, however, that Lorentz non-invariant formulations come with similar caveats and warnings as do gauge non-invariant formulations of quantum field theory: while they can be practical to work with at intermediate stages of a calculation, one should be careful with any physical conclusions that rely explicitly on them.

We shall therefore here restrict ourselves to a Lorentz-invariant formalism based directly on equation (62), pioneered by the dipole formulation of QCD cascades [86]. The collinear limit is then replaced by a more general *single-pole* limit in which a single parton-parton invariant vanishes (as, *for instance*, when a pair of partons become collinear), while the soft limit is replaced by one in which two (or more) invariants involving the same parton vanish simultaneously (as, for instance by that parton becoming soft in a frame defined by two or more hard partons). This avoids frame-dependent ambiguities from entering into the language, at the price of a slight reinterpretation of what is meant by collinear and soft.

In the generator landscape, *angular ordering* is used by the HERWIG [117] and HERWIG++ [118] programs, and an *angular veto* is imposed on the virtuality-ordered evolution in PYTHIA 6 [119]. Variants of the dipole/antenna approach is used by the ARIADNE [120], SHERPA [121, 122], and VINCIA [115] programs, while the p_{\perp} -ordered showers in PYTHIA 6 and 8 represent a hybrid, combining collinear splitting kernels with dipole kinematics [123]. Phase-space contours of equal value of some of these choices are illustrated in figure 18. During the shower evolution, each model effectively “sweeps” over phase space in the order implied by these contours. E.g., a p_{\perp} -ordered dipole shower (leftmost plot in figure 18) will treat a hard-collinear branching as occurring “earlier” than a soft one, while a mass-ordered dipole shower (second plot) will tend to do the opposite. This affects the tower of virtual corrections generated by each shower model via the so-called Sudakov factor, discussed below. Experimental tests of the subleading aspects of shower models can therefore quite important, see e.g. [124] for a recent example.

Independently of rewritings and philosophy, the real power of equation (62) lies in the fact that it is *universal*. Thus, for *any* process F , we can apply equation (62) in order to get an approximation for $d\sigma_{F+1}$. We may then, for instance, take our newly obtained expression for $F + 1$ as our arbitrary process and crank equation (62) again, to obtain an approximation for $d\sigma_{F+2}$, and so forth. What we have here is therefore a very simple recursion relation that can be used to generate approximations to leading-order cross sections with arbitrary numbers of

additional legs. The quality of this approximation is governed by how many terms besides the leading one shown in equation (53) are included in the game. Including all possible terms, the most general form for the cross section at $F + n$ jets, restricted to the phase-space region above some infrared cutoff scale μ_{IR} , has the following algebraic structure,

$$\sigma_{F+n}^{(0)} = \alpha_s^n \ln^{2n} + \ln^{2n-1} + \ln^{2n-2} + \dots + \ln + \mathcal{F} \quad (65)$$

where we use the notation \ln^λ without an argument to denote generic functions of *transcendentality* λ (the logarithmic function to the power λ being a “typical” example of a function with transcendentality λ appearing in cross section expressions, but also dilogarithms and higher logarithmic functions²³ of transcendentality > 1 should be implicitly understood to belong to our notation \ln^λ). The last term, \mathcal{F} , represents a rational function of transcendentality 0. We shall also use the nomenclature *singular* and *finite* for the \ln^λ and \mathcal{F} terms, respectively, a terminology which reflects their respective behavior in the limit $\mu_{\text{IR}} \rightarrow 0$.

The simplest approximation one can build on equation (65), dropping all but the leading \ln^{2n} term in the parenthesis, is thus the *leading-transcendentality* approximation. This approximation is better known as the DLA (double logarithmic approximation), since it generates the correct coefficient for terms which have two powers of logarithms for each power of α_s , while terms of lower transcendentality are not guaranteed to have the correct coefficients. In so-called LL (leading-logarithmic) parton shower algorithms, one generally expects to reproduce the correct coefficients for the \ln^{2n} and \ln^{2n-1} terms. In addition, several formally subleading improvements are normally also introduced in such algorithms (such as explicit momentum conservation, gluon polarisation and other spin-correlation effects [125–127], higher-order coherence effects [116], renormalisation scale choices [128], finite-width effects [129], etc), as a means to improve the agreement with some of the more subleading coefficients as well, if not in every phase-space point then at least on average. Though LL showers do not magically acquire NLL (next-to-leading-log) precision from such procedures, one therefore still expects a significantly better average performance from them than from corresponding “strict” LL analytical resummations. A side effect of this is that it is often possible to “tune” shower algorithms to give better-than-nominal agreement with experimental distributions, by adjusting the parameters controlling the treatment of subleading effects. One should remember, however, that there is a limit to how much can be accomplished in this way — at some point, agreement with one process will only come at the price of disagreement with another, and at this point further tuning would be meaningless.

Applying such an iterative process on a Born-level cross section, one obtains the description of the full perturbative series illustrated in figure 19. The yellow (lighter) shades used here for $k \geq 1$ indicate that the coefficient obtained is not the exact one, but rather an approximation to it that only gets its leading singularities right. However, since this is still only an approximation to infinite-order *tree-level* cross sections (we have not yet included any virtual corrections), we cannot yet integrate this approximation over all of phase space, as illustrated by the yellow boxes being only half filled in figure 19; otherwise, the summed total cross section would still be infinite. This particular approximation would therefore still appear to be very useless indeed — on one hand, it is only guaranteed to get the singular terms right, but on the other, it does

²³Note: due to the theorems that allow us, for instance, to rewrite dilogarithms in different ways with logarithmic and lower “spillover” terms, the coefficients at each λ are only well-defined up to reparametrisation ambiguities involving the terms with transcendentality greater than λ .

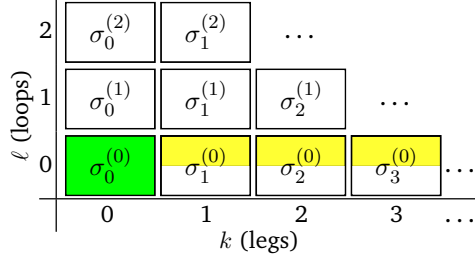
F @ LO \times LL(non-unitary)

Figure 19: Coefficients of the perturbative series covered by LO + LL approximations to higher-multiplicity tree-level matrix elements. Green (darker) shading represents the full perturbative coefficient at the respective k and ℓ . Yellow (lighter) shading represents an LL approximation to it. Half-shaded boxes indicate phase spaces in which we are prohibited from integrating over the IR singular region, as discussed in sections 2.3 and 4.

not actually allow us to integrate over the singular region. In order to obtain a truly *all-orders* calculation, the constraint of unitarity must also be explicitly imposed, which furnishes an approximation to all-orders loop corrections as well. Let us therefore emphasise that figure 19 is included for pedagogical purposes only; all resummation calculations, whether analytical or parton-shower based, include virtual corrections as well and consequently yield finite total cross sections, as will now be described.

3.2.2 Step Two: Infinite Loops

Order-by-order unitarity, such as used in the KLN theorem, implies that the singularities caused by integration over unresolved radiation in the tree-level matrix elements must be canceled, order by order, by equal but opposite-sign singularities in the virtual corrections at the same order. That is, from equation (62), we immediately know that the 1-loop correction to $d\sigma_F$ *must* contain a term,

$$2\text{Re}[\mathcal{M}_F^{(0)} \mathcal{M}_F^{(1)*}] \supset g_s^2 N_C \left| \mathcal{M}_F^{(0)} \right|^2 \int \frac{ds_{ij} ds_{jk}}{16\pi^2 s_{ijk}} \left(\frac{2s_{ik}}{s_{ij}s_{jk}} + \text{less singular terms} \right), \quad (66)$$

that cancels the divergence coming from equation (62) itself. Further, since this is universally true, we may apply equation (66) again to get an approximation to the corrections generated by equation (62) at the next order and so on. By adding such terms explicitly, order by order, we may now bootstrap our way around the entire perturbative series, using equation (62) to move horizontally and equation (66) to move along diagonals of constant $n = k + \ell$. Since real-virtual cancellations are now explicitly restored, we may finally extend the integrations over all of phase space, resulting in the picture shown in figure 20.

The picture shown in figure 20, not the one in figure 19, corresponds to what is actually done in *resummation* calculations, both of the analytic and parton-shower types²⁴. Physically, there is a significant and intuitive meaning to the imposition of unitarity, as follows.

²⁴In the way these calculations are formulated in practice, they in fact rely on one additional property, called exponentiation, that allows us to move along straight vertical lines in the loops-and-legs diagrams. However, since the two different directions furnished by equations (62) and (66) are already sufficient to move freely in the full 2D coefficient space, we shall use exponentiation without extensively justifying it here.

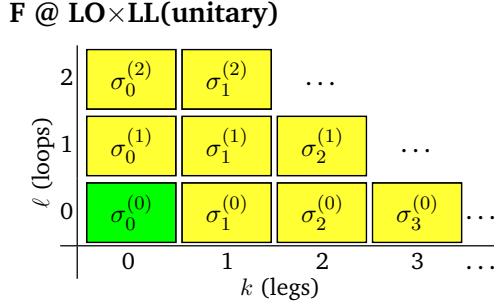


Figure 20: Coefficients of the perturbative series covered by LO + LL calculations, imposing unitarity order by order for each $n = k + \ell$. Green (darker) shading represents the full perturbative coefficient at the respective k and ℓ . Yellow (lighter) shading represents an LL approximation to it.

Take a jet algorithm, with some measure of jet resolution, Q , and apply it to an arbitrary sample of events, say dijets. At a very crude resolution scale, corresponding to a high value for Q , you find that everything is clustered back to a dijet configuration, and the 2-jet cross section is equal to the total inclusive cross section,

$$\sigma_{\text{tot}} = \sigma_{F;\text{incl}} . \quad (67)$$

At finer resolutions, decreasing Q , you see that some events that were previously classified as 2-jet events contain additional, lower-scale jets, that you can now resolve, and hence those events now migrate to the 3-jet bin, while the total inclusive cross section of course remains unchanged,

$$\sigma_{\text{tot}} = \sigma_{F;\text{incl}} = \sigma_{F;\text{excl}}(Q) + \sigma_{F+1;\text{incl}}(Q) , \quad (68)$$

where “incl” and “excl” stands for inclusive and exclusive cross sections²⁵, respectively, and the Q -dependence in the two terms on the right-hand side must cancel so that the total inclusive cross section is independent of Q . Later, some 3-jet events now migrate further, to 4 and higher jets, while still more 2-jet events migrate *into* the 3-jet bin, etc. For arbitrary n and Q , we have

$$\sigma_{F+n;\text{incl}}(Q) = \sigma_{F;\text{incl}} - \sum_{m=0}^{n-1} \sigma_{F+m;\text{excl}}(Q) . \quad (69)$$

This equation expresses the trivial fact that the cross section for n or more jets can be computed as the total inclusive cross section for F minus a sum over the cross sections for $F + m$ jets including all $m < n$. On the theoretical side, it is these negative terms which must be included in the calculation, for each order $n = k + \ell$, to restore unitarity. Physically, they express that, at a given scale Q , each event will be classified as having *either* 0, 1, 2, or whatever jets. Or, equivalently, for each event we gain in the 3-jet bin as Q is lowered, we must lose one event in the 2-jet one; the negative contribution to the 2-jet bin is exactly minus the integral of the positive contribution to the 3-jet one, and so on. We may perceive of this *detailed balance* as an *evolution* of the event structure with Q , for each event, which is effectively what is done in parton-shower algorithms, to which we shall return in Section 3.3.

²⁵ F inclusive = F plus anything. F exclusive = F and only F . Thus, $\sigma_{F;\text{incl}} = \sum_{k=0}^{\infty} \sigma_{F+k;\text{excl}}$

3.3 Perturbation Theory with Markov Chains

Consider again the Born-level cross section for an arbitrary hard process, F , differentially in an arbitrary infrared-safe observable \mathcal{O} , as obtained from equation (45):

$$\frac{d\sigma_F^{(0)}}{d\mathcal{O}} \Big|_{\text{Born}} = \int d\Phi_F |\mathcal{M}_F^{(0)}|^2 \delta(\mathcal{O} - \mathcal{O}(\Phi_F)), \quad (70)$$

where the integration runs over the full final-state on-shell phase space of F (this expression and those below would also apply to hadron collisions were we to include integrations over the parton distribution functions in the initial state), and the δ function projects out a 1-dimensional slice defined by \mathcal{O} evaluated on the set of final-state momenta which we denote Φ_F .

To make the connection to parton showers, we insert an operator, \mathcal{S} , that acts on the Born-level final state *before* the observable is evaluated, i.e.,

$$\frac{d\sigma_F}{d\mathcal{O}} \Big|_{\mathcal{S}} = \int d\Phi_F |\mathcal{M}_F^{(0)}|^2 \mathcal{S}(\Phi_F, \mathcal{O}). \quad (71)$$

Formally, this operator — the evolution operator — will be responsible for generating all (real and virtual) higher-order corrections to the Born-level expression. The measurement δ function appearing explicitly in equation (70) is now implicit in \mathcal{S} .

Algorithmically, parton showers cast \mathcal{S} as an iterative Markov (i.e., history-independent) chain, with an evolution parameter, Q_E , that formally represents the factorisation scale of the event, below which all structure is summed over inclusively. Depending on the particular choice of shower algorithm, Q_E may be defined as a parton virtuality (virtuality-order showers), as a transverse-momentum scale (p_\perp -ordered showers), or as a combination of energies times angles (angular ordering). Regardless of the specific form of Q_E , the evolution parameter will go towards zero as the Markov chain develops, and the event structure will become more and more exclusively resolved. A transition from a perturbative evolution to a non-perturbative one can also be inserted, when the evolution reaches an appropriate scale, typically around 1 GeV. This scale, called the *hadronisation scale*, thus represents the lowest perturbative scale that can appear in the calculations, with all perturbative corrections below it summed over inclusively.

Working out the precise form that \mathcal{S} must have in order to give the correct expansions discussed in section 3.2 takes a bit of algebra, and is beyond the scope we aim to cover in these lectures. Heuristically, the procedure is as follows. We noted that the singularity structure of QCD is universal and that at least its first few terms are known to us. We also saw that we could iterate that singularity structure, using universality and unitarity, thereby bootstrapping our way around the entire perturbative series. This was illustrated by figure 20 in section 3.2.

Skipping intermediate steps, the form of the all-orders pure-shower Markov chain, for the

evolution of an event between two scales $Q_1 > Q_E > Q_2$, is,

$$\begin{aligned} \mathcal{S}(\Phi_F, Q_1, Q_2, \mathcal{O}) &= \underbrace{\Delta(\Phi_F, Q_1, Q_2) \delta(\mathcal{O} - \mathcal{O}(\Phi_F))}_{F + 0 \text{ exclusive above } Q_2} \\ &\quad + \underbrace{\sum_r \int_{Q_{E2}}^{Q_{E1}} \frac{d\Phi_{F+1}^r}{d\Phi_F} S_r(\Phi_{F+1}) \Delta(\Phi_F, Q_1, Q_{F+1}) \mathcal{S}(\Phi_{F+1}, Q_{F+1}, Q_2, \mathcal{O})}_{F + 1 \text{ inclusive above } Q_2}, \end{aligned} \quad (72)$$

with the so-called *Sudakov factor*,

$$\Delta(\Phi_F, Q_1, Q_2) = \exp \left[\sum_r \int_{Q_2}^{Q_1} \frac{d\Phi_{F+1}^r}{d\Phi_F} S_r(\Phi_{F+1}) \right], \quad (73)$$

defining the probability that there is *no evolution* (i.e., no emissions) between the scales Q_1 and Q_2 , according to the *radiation functions* S_r to which we shall return below. The term on the first line of equation (72) thus represents all events that *did not* evolve as the resolution scale was lowered from Q_1 to Q_2 , while the second line contains a sum and phase-space integral over those events that *did* evolve — including the insertion of $\mathcal{S}(\Phi_{F+1})$ representing the possible further evolution of the event and completing the iterative definition of the Markov chain.

The factor $d\Phi_{F+1}^r / d\Phi_F$ defines the chosen phase space factorisation. Our favorite is the so-called dipole-antenna factorisation, whose principal virtue is that it is the simplest Lorentz invariant factorisation which is simultaneously exact over all of phase space while only involving on-shell momenta. For completeness, its form is

$$\frac{d\Phi_{F+1}^r}{d\Phi_F} = \frac{d\Phi_3^r}{d\Phi_2} = ds_{a1} ds_{1b} \frac{d\phi}{2\pi} \frac{1}{16\pi^2 s_r}, \quad (74)$$

which involves just one color-anticolor pair for each r , with invariant mass squared $s_r = (p_a + p_1 + p_b)^2$. Other choices, such as purely collinear ones (only exact in the collinear limit or involving explicitly off-shell momenta), more global ones involving all partons in the event (more complicated, in our opinion), or less global ones with a single parton playing the dominant role as emitter, are also possible, again depending on the specific algorithm considered.

The radiation functions S_r obviously play a crucial role in these equations, driving the emission probabilities. For example, if $S_r \rightarrow 0$, then $\Delta \rightarrow \exp(0) = 1$ and all events stay in the top line of equation (72). Thus, in regions of phase space where S_r is small, there is little or no evolution. Conversely, for $S_r \rightarrow \infty$, we have $\Delta \rightarrow 0$, implying that *all* events evolve. One possible choice for the radiation functions S_r was implicit in equation (62), in which we took them to include only the leading (double) singularities, with r representing color-anticolor pairs. In general, the shower may exponentiate the entire set of universal singular terms, or only a subset of them (for example, the terms leading in the number of colors N_C), which is why we here let the explicit form of S_r be unspecified. Suffice it to say that in traditional parton showers, S_r would simply be the DGLAP splitting kernels (see, e.g., [4]), while they would be so-called dipole or antenna radiation functions in the various dipole-based approaches to QCD (see, e.g., [73, 77, 80, 86, 90, 91, 122, 130]).

The procedure for how to technically “construct” a shower algorithm of this kind, using random numbers to generate scales distributed according to equation (72), is described more fully in [90], using a notation that closely parallels the one used here. The procedure is also described at a more technical level in the review [6], though using a slightly different notation. Various aspects of the Sudakov veto algorithm are discussed in [13–15]. Finally, pedagogical introduction to Monte Carlo methods in general can be found in [11, 12].

3.4 Decays of Unstable Particles

In most BSM processes and some SM ones, an important aspect of the event simulation is how decays of short-lived particles, such as top quarks, EW and Higgs bosons, and new BSM resonances, are handled. We here briefly summarise the spectrum of possibilities, but emphasise that there is no universal standard. Users are advised to check whether the treatment of a given code is adequate for the physics study at hand.

The appearance of an unstable resonance as a physical particle at some intermediate stage of the event generation implies that its production and decay processes are treated as being factorised. This is called the *narrow width approximation* and is valid up to corrections of order $/m_0$, with the width and m_0 the pole mass of the particle. States whose widths are a substantial fraction of their mass should not be treated in this way, but rather as intrinsically virtual internal propagator lines.

For states treated as physical particles, two aspects are relevant: the mass distribution of the decaying particle itself and the distributions of its decay products. For the mass distribution, the simplest is to use a δ function at m_0 . The next level up, typically used in general-purpose Monte Carlos, is to use a Breit-Wigner distribution (relativistic or non-relativistic), which formally resums higher-order virtual corrections to the mass distribution. Note, however, that this still only generates an improved picture for *moderate* fluctuations away from m_0 . Similarly to above, particles that are significantly off-shell (in units of) should not be treated as resonant, but rather as internal off-shell propagator lines. In most Monte Carlo codes, some further refinements are also included, for instance by letting be a function of m (“running widths”) and by limiting the magnitude of the allowed fluctuations away from m_0 . See also [131] for an elaborate discussion of the Higgs boson lineshape.

For the distributions of the decay products, the simplest treatment is again to assign them their respective m_0 values, with a uniform (i.e., isotropic, or “flat”) phase-space distribution. A more sophisticated treatment distributes the decay products according to the differential decay matrix elements, capturing at least the internal dynamics and helicity structure of the decay process, including EPR-like correlations. Further refinements include polarisations of the external states [125–127] (see also [132–134] for phenomenological studies) and assigning the decay products their own Breit-Wigner distributions, the latter of which opens the possibility to include also intrinsically off-shell decay channels, like $H \rightarrow WW^*$. Please refer to the physics manual of the code you are using and/or make simple cross checks like plotting the distribution of phase-space invariants it produces.

During subsequent showering of the decay products, most parton-shower models will preserve the total invariant mass of each resonance-decay system separately, so as not to skew the original resonance shape.

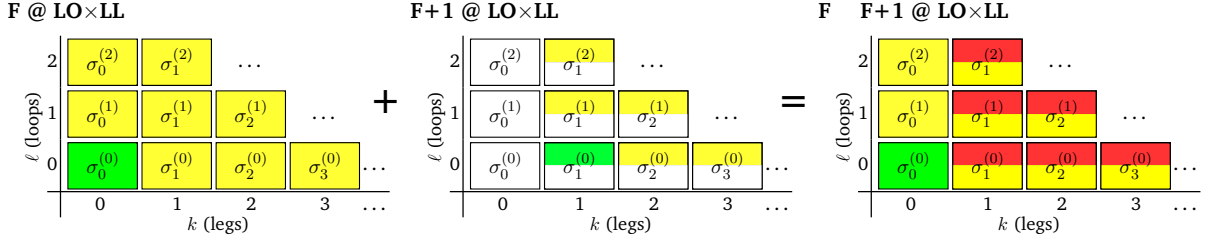


Figure 21: The double-counting problem caused by naively adding cross sections involving matrix elements with different numbers of legs.

4 Matching at LO and NLO

The essential problem that leads to matrix-element/parton-shower matching can be illustrated in a very simple way. Assume we have computed the LO cross section for some process, F , and that we have added an LL shower to it, as in the left-hand pane of figure 21. We know that this only gives us an LL description of $F + 1$. We now wish to improve this from LL to LO by adding the actual LO matrix element for $F + 1$. Since we also want to be able to hadronize these events, etc, we again add an LL shower off them. However, since the matrix element for $F + 1$ is divergent, we must restrict it to cover only the phase-space region with at least one hard resolved jet, illustrated by the half-shaded boxes in the middle pane of figure 21.

Adding these two samples, however, we end up counting the LL terms of the inclusive cross section for $F + 1$ twice, since we are now getting them once from the shower off F and once from the matrix element for $F + 1$, illustrated by the dark shaded (red) areas of the right-hand pane of figure 21. This *double-counting* problem would grow worse if we attempted to add more matrix elements, with more legs. The cause is very simple. Each such calculation corresponds to an *inclusive* cross section, and hence naive addition would give

$$\sigma_{\text{tot}} = \sigma_{0;\text{incl}} + \sigma_{1;\text{incl}} = \sigma_{0;\text{excl}} + 2\sigma_{1;\text{incl}}. \quad (75)$$

Recall the definition of inclusive and exclusive cross sections, equation (68): F *inclusive* = F plus anything. F *exclusive* = F and only F . Thus, $\sigma_{F;\text{incl}} = \sum_{k=0}^{\infty} \sigma_{F+k;\text{excl}}$.

Instead, we must *match* the coefficients calculated by the two parts of the full calculation — showers and matrix elements — more systematically, for each order in perturbation theory, so that the nesting of inclusive and exclusive cross sections is respected without overcounting.

Given a parton shower and a matrix-element generator, there are fundamentally three different ways in which we can consider matching the two [90]: slicing, subtraction, and unitarity. The following subsections will briefly introduce each of these.

4.1 Slicing

The most commonly encountered matching type is currently based on separating (slicing) phase space into two regions, one of which is supposed to be mainly described by hard matrix elements and the other of which is supposed to be described by the shower. This type of approach was first used in HERWIG [100], to include matrix-element corrections for one emission beyond the basic hard process [135, 136]. This is illustrated in figure 22. The method

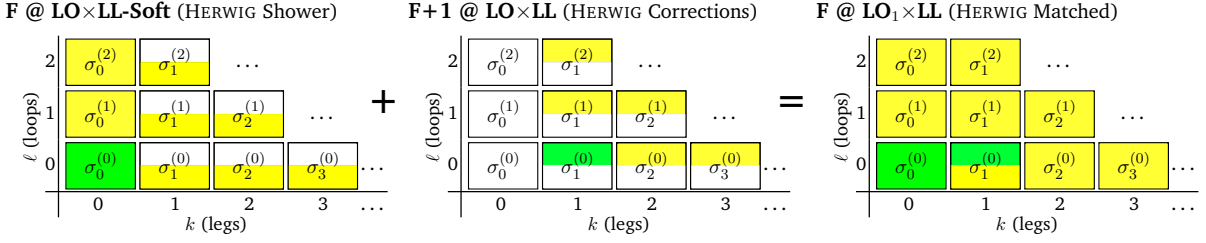


Figure 22: HERWIG’s original matching scheme [135, 136], in which the dead zone of the HERWIG shower was used as an effective “matching scale” for one emission beyond a basic hard process.

has since been generalized by several independent groups to include arbitrary numbers of additional legs, the most well-known of these being the CKKW [137], CKKW-L [138, 139], and MLM [140, 141] approaches.

Effectively, the shower approximation is set to zero above some scale, either due to the presence of explicit dead zones in the shower, as in HERWIG, or by vetoing any emissions above a certain *matching scale*, as in the (L)-CKKW and MLM approaches. The empty part of phase space can then be filled by separate events generated according to higher-multiplicity tree-level matrix elements (MEs). In the (L)-CKKW and MLM schemes, this process can be iterated to include arbitrary numbers of additional hard legs (the practical limit being around 3 or 4, due to computational complexity).

In order to match smoothly with the shower calculation, the higher-multiplicity matrix elements must be associated with Sudakov form factors (representing the virtual corrections that would have been generated if a shower had produced the same phase-space configuration), and their α_s factors must be chosen so that, at least at the matching scale, they become identical to the choices made on the shower side [142]. The CKKW and MLM approaches do this by constructing “fake parton-shower histories” for the higher-multiplicity matrix elements. By applying a sequential jet clustering algorithm, a tree-like branching structure can be created that at least has the same dominant structure as that of a parton shower. Given the fake shower tree, α_s factors can be chosen for each vertex with argument $\alpha_s(p_\perp)$ and Sudakov factors can be computed for each internal line in the tree. In the CKKW method, these Sudakov factors are estimated analytically, while the MLM and CKKW-L methods compute them numerically, from the actual shower evolution.

Thus, the matched result is identical to the matrix element (ME) in the region above the matching scale, modulo higher-order (Sudakov and α_s) corrections. We may sketch this as

$$\text{Matched (above matching scale)} = \underbrace{\text{Exact}}_{\text{ME}} \times \overbrace{(1 + \mathcal{O}(\alpha_s))}^{\text{corrections}}, \quad (76)$$

where the “shower-corrections” include the approximate Sudakov factors and α_s reweighting factors applied to the matrix elements in order to obtain a smooth transition to the shower-dominated region.

Below the matching scale, the small difference between the matrix elements and the shower approximation can be dropped (since their leading singularities are identical and this

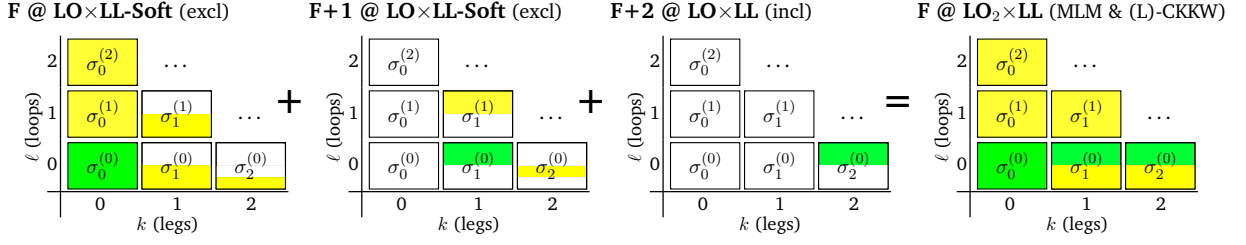


Figure 23: Slicing, with up to two additional emissions beyond the basic process. The showers off F and $F + 1$ are set to zero above a specific “matching scale”. (The number of coefficients shown was reduced a bit in these plots to make them fit in one row.)

region by definition includes no hard jets), yielding the pure shower answer in that region,

$$\begin{aligned}
 \text{Matched (below matching scale)} &= \overbrace{\text{Approximate}}^{\text{shower}} + (\text{Exact} \quad \overbrace{\text{Approximate}}^{\text{correction}}) \\
 &= \text{Approximate} + \text{non-singular} \\
 &\rightarrow \text{Approximate} .
 \end{aligned} \tag{77}$$

This type of strategy is illustrated in figure 23.

As emphasized above, since this strategy is discontinuous across phase space, a main point here is to ensure that the behavior across the matching scale be as smooth as possible. CKKW showed [137] that it is possible to remove any dependence on the matching scale through NLL precision by careful choices of all ingredients in the matching; technical details of the implementation (affecting the $\mathcal{O}(\alpha_s)$ terms in eq. (76)) are important, and the dependence on the unphysical matching scale may be larger than NLL unless the implementation matches the theoretical algorithm precisely [138, 139, 143]. Furthermore, since the Sudakov factors are generally computed using showers (MLM, L-CKKW) or a shower-like formalism (CKKW), while the real corrections are computed using matrix elements, care must be taken not to (re-)introduce differences that could break the detailed real-virtual balance that ensures unitarity among the singular parts, see e.g., [142].

It is advisable not to choose the matching scale too low. This is again essentially due to the approximate scale invariance of QCD imploring us to write the matching scale as a ratio, rather than as an absolute number. If one uses a very low matching scale, the higher-multiplicity matrix elements will already be quite singular, leading to very large LO cross sections before matching. After matching, these large cross sections are tamed by the Sudakov factors produced by the matching scheme, and hence the final cross sections may still look reasonable. But the higher-multiplicity matrix elements in general contain subleading singularity structures, beyond those accounted for by the shower, and hence the delicate line of detailed balance that ensures unitarity has most assuredly been overstepped. We therefore recommend not to take the matching scale lower than about an order of magnitude below the characteristic scale of the hard process.

One should also be aware that all strategies of this type are quite computing intensive. This is basically due to the fact that a separate phase-space generator is required for each of the n -parton correction terms, with each such sample a priori consisting of weighted events

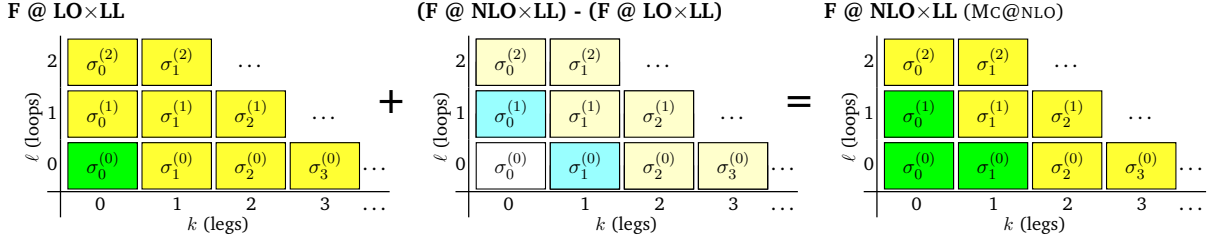


Figure 24: MC@NLO. In the middle pane, cyan boxes denote non-singular correction terms, while the egg-colored ones denote showers off such corrections, which cannot lead to double-counting at the LL level.

such that a separate unweighting step (often with quite low efficiency) is needed before an unweighted sample can be produced.

4.2 Subtraction

Another way of matching two calculations is by subtracting one from the other and correcting by the difference, schematically

$$\text{Matched} = \underbrace{\text{Approximate}}_{\text{shower}} + \underbrace{(\text{Exact} - \text{Approximate})}_{\text{correction}}. \quad (78)$$

This looks very much like the structure of a subtraction-based NLO fixed-order calculation, section 2.4, in which the shower approximation here plays the role of subtraction terms, and indeed this is what is used in strategies like MC@NLO [144–146], illustrated in figure 24. In this type of approach, however, negative-weight events will generally occur, for instance in phase-space points where the approximation is larger than the exact answer.

Negative weights are not in principle an insurmountable problem. Histograms can be filled with each event counted according to its weight, as usual. However, negative weights do affect efficiency. Imagine a worst-case scenario in which 1000 positive-weight events have been generated, along with 999 negative-weight ones (assuming each event weight has the same absolute value, the closest one can get to an unweighted sample in the presence of negative weights). The statistical precision of the MC answer would be equivalent to one event, for 2000 generated, i.e., a big loss in convergence rate.

In practice, generators like MC@NLO “only” produce around 10 or less events with negative weights, so the convergence rate should not be severely affected for ordinary applications. Nevertheless, the problem of negative weights motivated the development of the so-called POWHEG approach [147], illustrated in figure 25, which is constructed specifically to prevent negative-weight events from occurring and simultaneously to be more independent of which parton-shower algorithm it is used with. In the POWHEG method, one effectively modifies the real-emission probability for the first emission to agree with the $F + 1$ matrix element (this is covered under unitarity, below). One is then left with a purely virtual correction, which will typically be positive, at least for processes for which the NLO cross section is larger than the LO one.

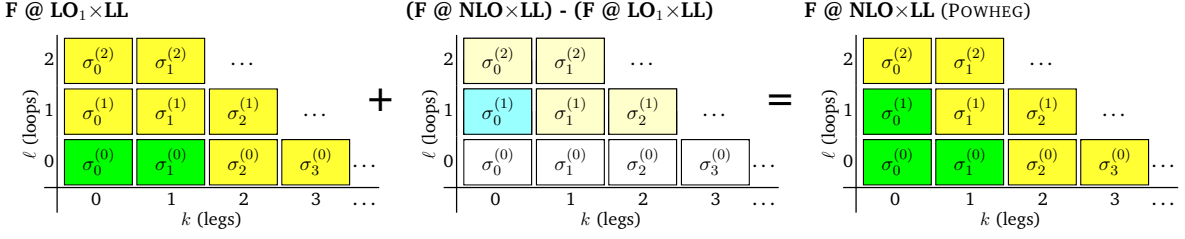


Figure 25: POWHEG. In the middle pane, cyan boxes denote non-singular correction terms, while the egg-colored ones denote showers off such corrections, which cannot lead to double-counting at the LL level.

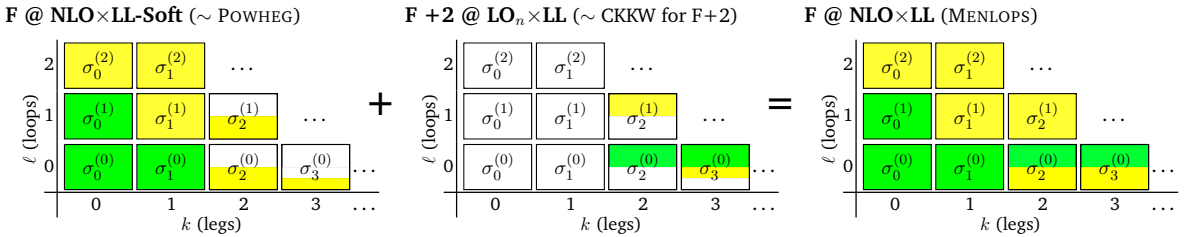


Figure 26: MENLOPS. Note that each of the POWHEG and CKKW samples are composed of separate sub-samples, as illustrated in figures 23 and 25.

The advantage of these methods is obviously that NLO corrections to the Born level can be systematically incorporated. However, a systematic way of extending this strategy beyond the first additional emission is not available, save for combining them with a slicing-based strategy for the additional legs, as in MENLOPS [148], illustrated in figure 26. These issues are, however, no more severe than in ordinary fixed-order NLO approaches, and hence they are not viewed as disadvantages if the point of reference is an NLO computation.

4.3 Unitarity

The oldest, and in my view most attractive, approach [119, 149] consists of working out the shower approximation to a given fixed order, and correcting the shower splitting functions at that order by a multiplicative factor given by the ratio of the matrix element to the shower approximation, phase-space point by phase-space point. We may sketch this as

$$\text{Matched} = \overbrace{\text{Approximate}}^{\text{shower}} \times \underbrace{\frac{\text{Exact}}{\text{Approximate}}}_{\text{correction}}. \quad (79)$$

When these correction factors are inserted back into the shower evolution, they guarantee that the shower evolution off $n-1$ partons correctly reproduces the n -parton matrix elements, without the need to generate a separate n -parton sample. That is, the shower approximation is essentially used as a pre-weighted (stratified) all-orders phase-space generator, on which a more exact answer can subsequently be imprinted order by order in perturbation theory. Since

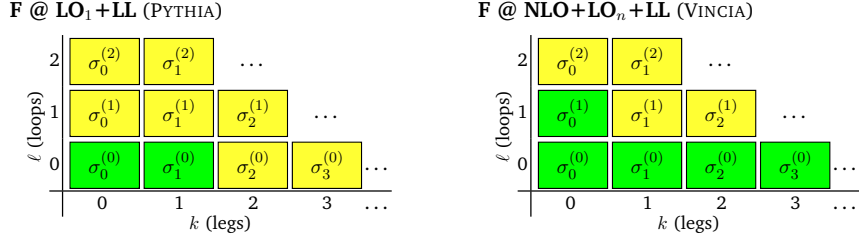


Figure 27: PYTHIA (left) and VINCIA (right). Unitarity-based. Only one event sample is produced by each of these methods, and hence no sub-components are shown.

the shower is already optimized for exactly the kind of singular structures that occur in QCD, very fast computational speeds can therefore be obtained with this method [91].

In the original approach [119, 149], used by PYTHIA [102, 103], this was only worked out for one additional emission beyond the basic hard process. In POWHEG [147, 150], it was extended to include also virtual corrections to the Born-level matrix element. Finally, in VINCIA, it has been extended to include arbitrary numbers of emissions at tree level [90, 91] and one emission at loop level [151], though that method has so far only been applied to final-state showers.

An illustration of the perturbative coefficients that can be included in each of these approaches is given in figure 27, as usual with green (darker shaded) boxes representing exact coefficients and yellow (light shaded) boxes representing logarithmic approximations.

Finally, two more properties unique to this method deserve mention. Firstly, since the corrections modify the actual shower evolution kernels, the corrections are automatically *resummed* in the Sudakov exponential, which should improve the logarithmic precision once $k \geq 2$ is included, and secondly, since the shower is *unitary*, an initially unweighted sample of $(n - 1)$ -parton configurations remains unweighted, with no need for a separate event-unweighting or event-rejection step.

5 Hadronisation and Soft Hadron-Hadron Physics

We here give a very brief overview of the main aspects of soft QCD that are relevant for hadron-hadron collisions, such as hadronisation, minimum-bias and soft-inclusive physics, and the so-called underlying event. This will be kept at a pedestrian level and is largely based on the reviews in [6, 31, 152].

In the context of event generators, *hadronisation* denotes the process by which a set of coloured partons (*after showering*) is transformed into a set of colour-singlet *primary* hadrons, which may then subsequently decay further. This non-perturbative transition takes place at the *hadronisation scale* Q_{had} , which by construction is identical to the infrared cutoff of the parton shower. In the absence of a first-principles solution to the relevant dynamics, event generators use QCD-inspired phenomenological models to describe this transition.

The problem can be stated as follows: given a set of partons resolved at a scale of $Q_{\text{had}} \sim 1 \text{ GeV}$, we need a “mapping” from this set onto a set of on-shell colour-singlet (i.e., confined) hadronic states. MC models do this in three steps:

1. Map the partonic system onto a continuum of high-mass hadronic states (called “strings” or “clusters”).
2. Iteratively map strings/clusters onto discrete set of primary hadrons (via string breaks / cluster splittings / cluster decays).
3. Sequential decays into secondaries ($\rho \rightarrow \pi\pi$, $\Lambda \rightarrow n\pi$, $\pi^0 \rightarrow \gamma\gamma$, ...).

The physics governing this mapping is non-perturbative. However, we do have some knowledge of the properties that such a solution must have. For instance, Poincaré invariance, unitarity, and causality are all concepts that apply beyond perturbation theory. In addition, lattice QCD provides us a means of making explicit quantitative studies in a genuinely non-perturbative setting (albeit only of certain questions).

An important result in “quenched” lattice QCD²⁶ is that the potential of the colour-dipole field between a charge and an anticharge appears to grow linearly with the separation of the charges, at distances greater than about 0.5 femtometers; this behavior is illustrated by the plot shown in figure 28, from [153]. (Note that the axes are scaled by units of the string tension $\sqrt{\kappa} \sim 420 \text{ MeV}$. Additional labels corresponding to 1 GeV and 2 GeV are also provided, on the y axis, and to 1 fm and 2 fm, on the x axis.) This is known as “linear confinement”, and it forms the starting point for the *string model of hadronisation*, discussed below in section 5.1. Alternatively, a property of perturbative QCD called “preconfinement” [154] is the basis of the *cluster model of hadronisation*, described in [6, 31].

In the generator landscape, PYTHIA [102, 103], QGSJET [155], and SIBYLL [156] use string fragmentation models (as do ARIADNE [120], DPMJET [157], PHOJET [158], and VINCIA [115] via interfaces to PYTHIA), while HERWIG [101] and SHERPA [104] use cluster fragmentation. EPOS [159] uses a combination of string hadronisation and a hydrodynamics-inspired statistical hadronisation model.

It should be emphasised that the so-called *parton level* that can be obtained by switching off hadronisation in an MC generator, is not a universal concept, since each model defines

²⁶Quenched QCD implies no “dynamical” quarks, i.e., no $g \rightarrow q\bar{q}$ splittings allowed.

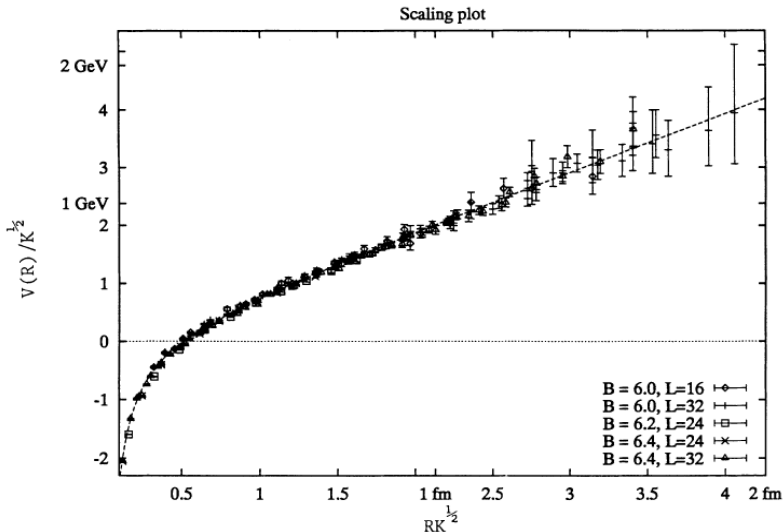


Figure 28: Static quark-antiquark potential, as a function of separation distance, in quenched lattice QCD, from [153]. Note that the axes are scaled by units of the string tension $\sqrt{\kappa} \sim 420$ MeV. Additional labels corresponding to 1 GeV and 2 GeV are also provided, on the y axis, and to 1 fm and 2 fm, on the x axis. A constant term, V_0 , has been subtracted from all the results. The dashed line corresponds to $V(R) = R - \pi/(12R)$.

the hadronisation scale differently. E.g., the hadronisation scale can be defined by a cutoff in invariant mass, transverse momentum, or some other quantity, with different tunes using different values for the cutoff. The former is equivalent to using different effective factorisation schemes, and the latter corresponds to different factorisation scales, for the soft non-perturbative component of the modelling. Comparisons to distributions at this level (i.e., with hadronisation switched off) may therefore be used to provide an idea of the overall impact of hadronisation corrections within a given model, but should be avoided in the context of physical observables. Note also that the corresponding MC *fragmentation functions* are intrinsically defined at the hadronisation scale. They can therefore not be compared directly to those that are used in fixed-order / analytical-resummation contexts, which are typically defined at a factorisation scale of order the scale of the hard process.

We use the term “soft hadron-hadron physics” to comprise all scattering processes for which a hard, perturbative scale is not required to be present²⁷. This includes elastic, diffractive, minimum-bias, and pile-up processes, as well as the physics contributing to the so-called underlying event. We give a brief introduction to such processes in section 5.2.

We round off with a discussion of the data constraints that enter in the tuning of Monte Carlo models in section 5.4, and give an outline of a procedure that could be followed in a realistic set-up.

²⁷Note, however, that while a hard scale is not *required* to be present, it is not explicitly required to be absent either. Thus, both diffractive, minimum-bias, pile-up and underlying-event processes will have tails towards high- p_\perp physics as well. For example, even $t\bar{t}$ pair production can be viewed as a tail of minimum-bias interactions, and there is a tail of diffractive processes in which hard dijets can be produced diffractively (see, e.g., [160]).

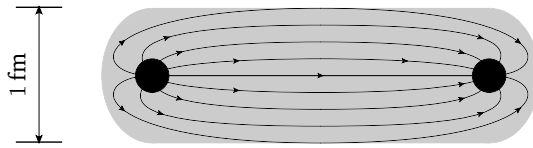


Figure 29: Illustration of the transition between a Coulomb potential at short distances to the string-like one of equation (80) at large $q\bar{q}$ separations.

5.1 The String Model of Hadronisation

Starting from early concepts developed by Artru and Mennessier [161], several hadronisation models based on strings were proposed in the late 1970's and early 80's. Of these, the most widely used today is the so-called Lund model, implemented in the PYTHIA code. We shall therefore concentrate on that particular model here, though many of the overall concepts would be shared by any string-inspired method. (More extended discussions can be found in Andersson's book [8] and in an older comprehensive Physics Reports review [7].)

Consider the production of a $q\bar{q}$ pair from vacuum, for instance in the process $e^+e^- \rightarrow \gamma^*/Z \rightarrow q\bar{q} \rightarrow \text{hadrons}$. As the quarks move apart, linear confinement implies that a potential

$$V(R) = \kappa R \quad (80)$$

is asymptotically reached for large distances, R . At short distances, there is a Coulomb term proportional to $1/R$ as well, cf. figure 28, but this is neglected in the Lund model. Such a potential describes a string with tension (energy per unit length) κ , with the value [153]

$$\kappa \sim (420 \text{ MeV})^2 \sim 0.18 \text{ GeV}^2 \sim 0.9 \text{ GeV/fm}, \quad (81)$$

which, for comparison with the world of macroscopic objects, would be sufficient to lift a 16-ton truck [162].

The string can be thought of as parameterizing the position of the axis of a cylindrically symmetric flux tube, illustrated in figure 29. Such simple $q - \bar{q}$ strings form the starting point for the string model. More complicated multi-parton topologies are treated by representing gluons as transverse “kinks”, e.g., $q - g - \bar{q}$. The space-time evolution is then slightly more involved [8], and modifications to the fragmentation model to handle stepping across gluon corners have to be included, but the main point is that there are no separate free parameters for gluon jets. Differences with respect to quark fragmentation arise simply because quarks are only connected to a single string piece, while gluons have one on either side, increasing the energy loss per unit (invariant) time from a gluon to the string by a factor of 2 relative to quarks, which can be compared to the ratio of colour Casimirs $C_A/C_F = 2.25$. Another appealing feature of the model is that low-energy gluons are absorbed smoothly into the string, without leading to modifications. This improves the stability of the model with respect to variations of the infrared behavior of the parton shower.

As the partonic string endpoints move apart, their kinetic energy is gradually converted to potential energy, stored in the growing string spanned between them. In the “quenched” approximation, in which $g \rightarrow q\bar{q}$ splittings are not allowed, this process would continue until the endpoint quarks have lost *all* their momentum, at which point they would reverse direction and be accelerated by the now shrinking string.

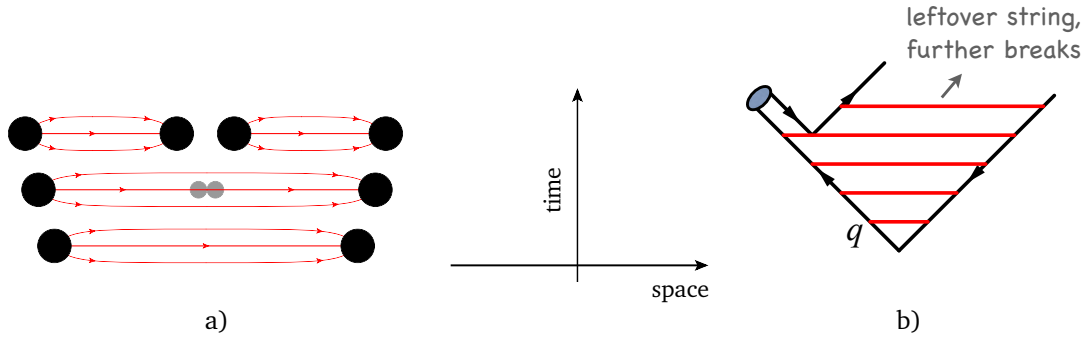


Figure 30: a) Illustration of string breaking by quark pair creation in the string field. b) Illustration of the algorithmic choice to process the fragmentation from the outside-in, splitting off a single on-shell hadron in each step.

In the real world, quark-antiquark fluctuations inside the string field can make the transition to become real particles by absorbing energy from the string, thereby screening the original endpoint charges from each other and breaking the string into two separate colour-singlet pieces, $(q\bar{q}) \rightarrow (q\bar{q}') + (q'\bar{q})$, illustrated in figure 30 a. This process then continues until only ordinary hadrons remain. (We will give more details on the individual string breaks below.)

Since the string breaks are causally disconnected (as can easily be realised from space-time diagrams like the one in figure 30, see also [8]), they do not have to be considered in any specific time-ordered sequence. In the Lund model, the string breaks are instead generated starting with the leading (“outermost”) hadrons, containing the endpoint quarks, and iterating inwards towards the center of the string, alternating randomly between fragmentation off the left- and right-hand sides, respectively, figure 30b. One can thereby split off a single well-defined hadron in each step, with a mass that, for unstable hadrons, is selected according to a Breit-Wigner distribution.

The details of the individual string breaks are not known from first principles. The Lund model invokes the idea of quantum mechanical tunneling, with a Gaussian suppression of the transverse momenta and masses imparted to the produced quarks²⁸,

$$\text{Prob}(m_q^2, p_{\perp q}^2) \propto \ln \left[1 - \exp \left(-\frac{\pi(m_q^2 + p_{\perp q}^2)}{\kappa} \right) \right] = \sum_{n=1}^{\infty} \frac{1}{n} \exp \left(-\frac{n\pi(m_q^2 + p_{\perp q}^2)}{\kappa} \right)$$

$$\stackrel{m_q^2 \gg \kappa/\pi}{\rightarrow} \exp \left(-\frac{\pi m_q^2}{\kappa} \right) \exp \left(-\frac{\pi p_{\perp q}^2}{\kappa} \right), \quad (82)$$

where m_q is the mass of the produced quark (the relevant range of values for the constituent up, down, and strange quark masses is typically taken to be $\sim 300 - 500$ MeV) and p_{\perp} is the transverse momentum imparted to it by the breakup process (with the \bar{q} having the opposite p_{\perp}).

²⁸The full form of the series essentially accounts for the probability that no string-decay event already happened and incorporates the exclusion principle that no more than one event can occur for each given quantum state of the produced pair, while the limiting Gaussian form is the naive probability per phase-space volume; see [163].

This form of the suppression factor was originally derived in 1951 by Schwinger in QED, for creation of electron-positron pairs in a strong constant electric field [164]²⁹. Its generalisation to QCD was first treated using WKB tunneling approximations [163, 166], and there is also a more recent claim of an exact path-integral solution [167], in all cases finding the same basic form as in the QED case³⁰. Since the Schwinger tunneling probability is derived for an infinitely extended constant field, while QCD flux tubes in nature have a finite size, modifications to the above baseline picture may be considered. E.g., a flux tube with radius r_s could imply a cutoff for momenta $p_{\perp \max} \sim 2r_s \kappa / \pi$ [163]. It is not straightforward to define the relevant radius unambiguously, however, and we note that, within the effective description in an MC program, tails to higher p_{\perp} values may be justified anyway due to unresolved perturbative effects below the shower cutoff. A high- p_{\perp} cutoff is therefore typically not imposed in the MC implementation. See [168] for a phenomenological study that explores some alternative assumptions (e.g., a thermal suppression) in an event-generator context.

Due to the factorisation of the p_{\perp} and m dependence implied by equation (82), the p_{\perp} spectrum of produced quarks in this model is independent of the quark flavour, with a universal average value of

$$\sigma^2 \equiv \langle p_{\perp q}^2 \rangle = \langle p_x^2 + p_y^2 \rangle \quad (83)$$

$$= \frac{\pi}{\kappa} \int_{-\infty}^{\infty} dp_x \int_{-\infty}^{\infty} dp_y (p_x^2 + p_y^2) \exp\left(-\frac{\pi(p_x^2 + p_y^2)}{\kappa}\right) \quad (84)$$

$$= \frac{\pi}{\kappa} \int_0^{\infty} dp_{\perp}^2 p_{\perp}^2 \exp(-\pi p_{\perp}^2 / \kappa) \quad (85)$$

$$= \kappa/\pi \sim (240 \text{ MeV})^2. \quad (86)$$

Bear in mind that “transverse” is here defined with respect to the string axis. Thus, the p_{\perp} in a frame where the string is moving is modified by a Lorentz boost factor. Also bear in mind that σ^2 is here a purely non-perturbative parameter. In a Monte Carlo model with a fixed shower cutoff Q_{had} , the effective amount of “non-perturbative” p_{\perp} may be larger than this, due to effects of additional unresolved soft-gluon radiation below Q_{had} (for example, the “Monash Tune” of PYTHIA 8 [169] has a final-state shower cutoff at $p_{\perp \min} = 500$ MeV and uses a value of $\sigma = 335$ MeV). In principle, the magnitude of this additional component should scale with the cutoff, but in practice it is up to the user to enforce this by retuning (see section 5.4) the effective σ parameter when changing the hadronisation scale. Since hadrons receive p_{\perp} contributions from two breakups, one on either side, their average transverse momentum squared will be twice as large,

$$\langle p_{\perp h}^2 \rangle = 2\sigma^2. \quad (87)$$

Finally, we note that the assumption $m_q^2 \gg \kappa/\pi$ which is used to justify neglecting the sub-leading terms equation (82) may be open to question and could lead to deviations of order 10% from the universal Gaussian spectrum, for realistic constituent masses.

The mass suppression implied by equation (82) is however less straightforward to interpret. Integrated over p_{\perp} , the Schwinger prediction is that the differential string decay proba-

²⁹Note that extremely strong electric fields are required, so the effect has not been observed in the lab yet, although attempts are being made at large laser facilities, see e.g. [165].

³⁰We note that the form in [167] also contains a term proportional to $|d_{abc} E^a E^b E^c|^2$ with d_{abc} the symmetric structure constants of QCD and E_a the chromoelectric field with index $a \in [1, 8]$.

bility (per unit space-time volume) via pair production of quarks with constituent mass m_q , is proportional to

$$P(m_q^2) \propto \sum_{n=1}^{\infty} \frac{1}{n^2} \exp\left(-\frac{n\pi m_q^2}{\kappa}\right) \xrightarrow{m_q^2 \gg \kappa/\pi} \exp\left(-\frac{\pi m_q^2}{\kappa}\right). \quad (88)$$

However, since quark masses are notoriously difficult to define for light quarks, the value of the strangeness suppression must effectively be extracted from experimental measurements, e.g., of the K/π ratio, with a resulting suppression of roughly $s/u \sim s/d \sim 0.2 - 0.3$. Inserting even comparatively low values for the charm quark mass in equation (82), however, one obtains a relative suppression of charm of the order of 10^{-11} . Heavy quarks can therefore safely be considered to be produced only in the perturbative stages and not by the soft fragmentation.

Baryon production can be incorporated in the same basic picture [170], by allowing string breaks to occur also by the production of pairs of so-called *diquarks*, loosely bound states of two quarks in an overall $\bar{3}$ representation (e.g., “red + blue \sim antigreen”, cf. the rules for colour combinations in section 1.2). Again, the relative rate of diquark-to-quark production is not known a priori and must be extracted from experimental measurements, e.g., of the p/π ratio. More advanced scenarios for baryon production have also been proposed, in particular the so-called popcorn model [171, 172], which is normally used in addition to the diquark picture and then acts to decrease the correlations among neighboring baryon-antibaryon pairs by allowing mesons to be formed in between them. Within the PYTHIA framework, a fragmentation model including explicit *string junctions* [173] has so far only been applied to baryon-number-violating new-physics processes and to the description of beam remnants (and then acts to increase baryon stopping [174]).

This brings us to the next step of the algorithm: assignment of the produced quarks within hadron multiplets. Using a nonrelativistic classification of spin states, the fragmenting q (\bar{q}) may combine with the \bar{q}' (q') from a newly created breakup to produce either a vector or a pseudoscalar meson, or, if diquarks are involved, either a spin-1/2 or spin-3/2 baryon. Unfortunately, the string model is entirely unpredictable in this respect, and this is therefore the sector that contains the largest amount of free parameters. From spin counting alone, one would expect the ratio V/S of vectors to pseudoscalars to be 3, but this is modified by the $V-S$ mass splittings, which implies a phase-space suppression of vector production, with corresponding suppression parameters to be extracted from data.

Especially for the light flavours, the substantial difference in phase space caused by the $V-S$ mass splittings implies a rather large suppression of vector production. Thus, for D^*/D , the effective ratio is already reduced to about $\sim 1.0 - 2.0$, while for K^*/K and ρ/π , extracted values range from $0.3 - 1.0$. (Recall, as always, that these are production ratios of *primary hadrons*, hence feed-down from secondary decays of heavier hadrons complicates the extraction of these parameters from experimental data, in particular for the lighter hadron species.)

The production of higher meson resonances is assumed to be low in a string framework³¹. For diquarks, separate parameters control the relative rates of spin-1 diquarks vs. spin-0 ones and, likewise, have to be extracted from data, with resulting values of order $(qq)_1/(qq)_0 \sim 0.075 - 0.15$.

³¹The four $L = 1$ multiplets are implemented in PYTHIA, but are disabled by default, largely because several states are poorly known and thus may result in a worse overall description when included.

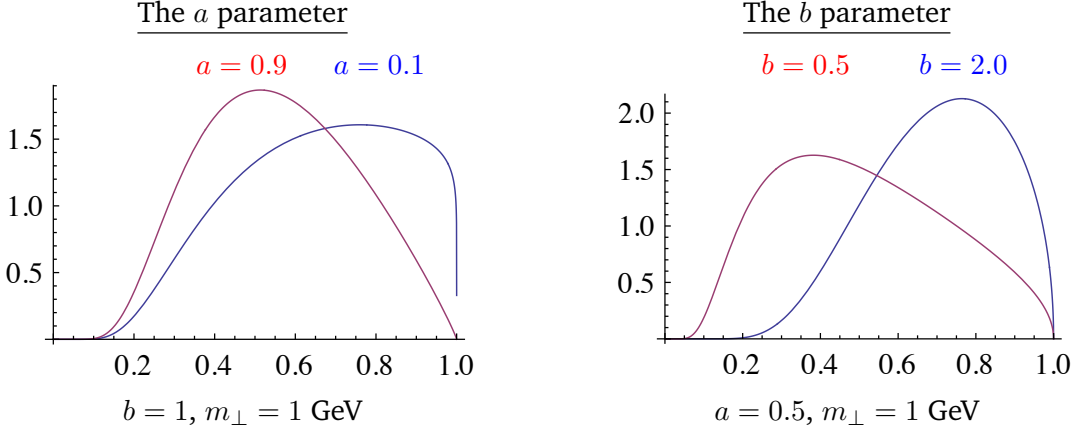


Figure 31: Normalised Lund symmetric fragmentation function, for fixed $m_{\perp} = 1 \text{ GeV}$. *Left:* variation of the a parameter, from 0.1 (blue) to 0.9 (red), with fixed $b = 1 \text{ GeV}^2$. *Right:* variation of the b parameter, from 0.5 (red) to 2 (blue) GeV^2 , with fixed $a = 0.5$.

With p_{\perp}^2 and m^2 now fixed, the final step is to select the fraction, z , of the fragmenting endpoint quark's longitudinal momentum that is carried by the created hadron. In this respect, the string picture is substantially more predictive than for the flavour selection. Firstly, the requirement that the fragmentation be independent of the sequence in which breakups are considered (causality) imposes a “left-right symmetry” on the possible form of the fragmentation function, $f(z)$, with the solution [175]

$$f(z) \propto \frac{1}{z} (1-z)^a \exp\left(-\frac{b(m_h^2 + p_{\perp h}^2)}{z}\right), \quad (89)$$

which is known as the *Lund symmetric fragmentation function* (normalised to unit integral). The a and b parameters, illustrated in figure 31, are the only free parameters of the fragmentation function, though a may in principle be flavour-dependent. Note that the explicit mass dependence in $f(z)$ implies a harder fragmentation function for heavier hadrons (in the rest frame of the string).

For massive endpoints (e.g., c and b quarks), which do not move along straight lightcone sections, the exponential suppression with string area leads to modifications of the form [176],

$$f(z) \rightarrow f(z)/z^{b m_Q^2}, \quad (90)$$

with m_Q the heavy-quark mass. Strictly speaking, this is the only fragmentation function that is consistent with causality in the string model, though a few alternative forms are typically provided as well.

As a by-product, the probability distribution in invariant time τ of $q'\bar{q}'$ breakup vertices, or equivalently $= (\kappa\tau)^2$, is also obtained, with $dP/d \propto e^{-a} \exp(-b)$ implying an area law for the colour flux [177], and the average breakup time lying along a hyperbola of constant invariant time $\tau_0 \sim 10^{-23} \text{s}$ [8].

We may also ask, e.g., how many units of rapidity does the particle production from a string span? Measuring p_z along the string direction and defining rapidity by

$$y = \frac{1}{2} \ln \left(\frac{E + p_z}{E - p_z} \right), \quad (91)$$

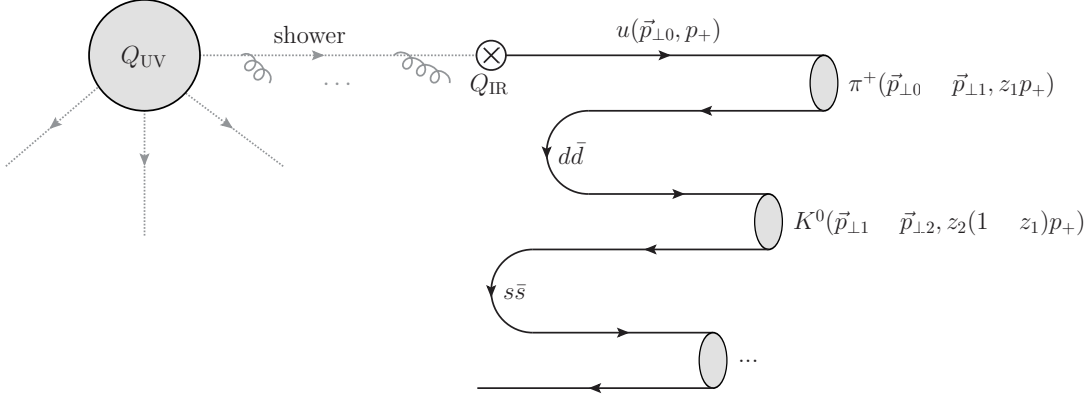


Figure 32: Iterative selection of flavours and momenta in the Lund string-fragmentation model.

the absolute highest rapidity that can be reached, by a pion traveling exactly along the string direction and taking all of the endpoint quark's energy, is $y_{\max} = \ln(2E_q/m_\pi)$. I.e., the rapidity region covered by a fragmenting string scales logarithmically with the energy, and since the density of hadrons produced per unit rapidity is roughly constant (modulo endpoint effects), the average number of hadrons produced by string fragmentation likewise scales logarithmically with energy.

The iterative selection of flavours, p_\perp , and z values is illustrated in figure 32. A parton produced in a hard process at some high scale Q_{UV} emerges from the parton shower, at the hadronisation scale Q_{IR} , with 3-momentum $\vec{p} = (\vec{p}_{\perp 0}, p_+)$, where the “+” on the third component denotes “light-cone” momentum, $p_+ = E \pm p_z$. Next, an adjacent $d\bar{d}$ pair from the vacuum is created, with relative transverse momenta $\pm p_{\perp 1}$. The fragmenting quark combines with the \bar{d} from the breakup to form a π^+ , which carries off a fraction z_1 of the total lightcone momentum p_+ . The next hadron carries off a fraction z_2 of the remaining momentum, etc.

5.2 Soft Hadron-Hadron Processes

The total hadron-hadron (hh) cross section is around 100 mb at LHC energies [178], growing slowly with the CM energy, $\sigma_{\text{tot}}(s) \propto s^{0.096}$ [179]. There are essentially four types of physics processes, which together make up σ_{tot} :

1. Elastic scattering: $hh \rightarrow hh$;
2. Single diffractive dissociation: $hh \rightarrow h + \text{gap} + X$, with “gap” denoting an empty rapidity region, and X anything that is not the original beam particle;
3. Double diffractive dissociation: $hh \rightarrow X + \text{gap} + X$ (both hadrons “blow up”);
4. Inelastic non-diffractive scattering: everything else.

In principle, higher “multi-gap” diffractive components may be defined as well, the most important one being central diffraction: $hh \rightarrow h + \text{gap} + X + \text{gap} + h$, see the discussion of diffraction in section 5.2.1 below.

Some important differences exist between theoretical and experimental terminology [180]. In the experimental setting, diffraction is defined by an observable rapidity gap, with $|\Delta y|_{\text{gap}} \gtrsim 3$ typically giving clean diffractive samples. In the MC context, however, each diffractive process type produces a whole spectrum of gaps, with small ones suppressed but not excluded. Likewise, events of non-diffractive origin may produce accidental rapidity gaps, now with large ones suppressed (exponentially) but not excluded, and in the transition region there could even be quantum mechanical interference between the two. Due to this unphysical model dependence of theoretical definitions of diffraction, we strongly advise to phrase measurements first and foremost in terms of physical observables, and only seek to connect with theory models as a second, separate, step.

The distinction between elastic and inelastic events is, however, unambiguous (modulo $pp \rightarrow pp\gamma$ events); the final state either contains just two protons, or not. The total hadron-hadron cross section can therefore be written as a sum of these two physically distinguishable components,

$$\sigma_{\text{tot}}(s) = \sigma_{\text{el}}(s) + \sigma_{\text{inel}}(s), \quad (92)$$

where $s = (p_A + p_B)^2$ is the beam-beam center-of-mass energy squared.

Another potentially confusing term is “minimum bias” (MB). This originates from the experimental requirement of a minimal energy or number of hits in a given (experiment-dependent) instrumented region near the beam, used to determine whether there was any non-trivial activity in the event, or not. This represents the smallest possible “trigger bias” that the corresponding experiment is capable of. There is thus no universal definition of “min-bias”; each experiment has its own. We give a brief discussion of minimum bias in section 5.2.2 below.

Finally, in events containing a hard parton-parton interaction, the *underlying event* (UE) can be roughly conceived of as the *difference* between QCD with and without including the remnants of the original beam hadrons. Without such “beam remnants”, only the hard interaction itself, and its associated parton showers and hadronisation, would contribute to the observed particle production. In reality, after the partons that participate in the hard interaction have been taken out, the remnants still contain whatever is left of the incoming beam hadrons, including also a partonic substructure, which leads to the possibility of *multiple parton interactions* (MPI). We discuss MPI-based models of the UE in section 5.3 below. Other useful reviews of MPI-based MC models can be found in [6, 152]. Analytical models are mostly formulated only for double parton scattering, see e.g., [181–184].

5.2.1 Diffractive Scattering

As mentioned above, if the beam particles A and/or B are not elementary, the inelastic final states may be divided into “diffractive” and “non-diffractive” topologies. This is a qualitative classification, usually based on whether the final state looks like the decay of an excitation of the beam particles (diffractive³²), or not (non-diffractive), or upon the presence of a large rapidity gap somewhere in the final state which would separate such excitations.

³²An example of a process that would be labeled as diffractive would be if one proton is excited to a $p \rightarrow p + \pi^0$, which then decays back to $p + \pi^0$, without anything else happening in the event. In general, a whole tower of possible diffractive excitations are available, which in the continuum limit can be described by a mass spectrum falling roughly as dM^2/M^2 .

Given that an event has been labeled as diffractive, either within the context of a theoretical model, or by a final-state observable, we may distinguish between three different classes of diffractive topologies, which it is possible to distinguish between physically, at least in principle. In double-diffractive (DD) events, both of the beam particles are diffractively excited and hence none of them survive the collision intact. In single-diffractive (SD) events, only one of the beam particles gets excited and the other survives intact. The last diffractive topology is central diffraction (CD), in which both of the beam particles survive intact, leaving an excited system in the central region between them. (This latter topology includes “central exclusive production” where a single particle is produced in the central region.) That is,

$$\sigma_{\text{inel}}(s) = \sigma_{\text{SD}}(s) + \sigma_{\text{DD}}(s) + \sigma_{\text{CD}}(s) + \sigma_{\text{ND}}(s) , \quad (93)$$

where “ND” (non-diffractive, here understood not to include elastic scattering) contains no gaps in the event consistent with the chosen definition of diffraction. Further, each of the diffractively excited systems in the events labeled SD, DD, and CD, respectively, may in principle consist of several subsystems with gaps between them. Eq. (93) may thus be defined to be exact, within a specific definition of diffraction, even in the presence of multi-gap events. Note, however, that different theoretical models almost always use different (model-dependent) definitions of diffraction, and therefore the individual components in one model are in general not directly comparable to those of another. It is therefore important that data be presented at the level of physical observables if unambiguous conclusions are to be drawn from them.

5.2.2 Minimum Bias

In principle, *everything* that produces a hit in a given experiment’s minimum-bias trigger, is a subset of minimum-bias (MB). In particular, since there is no explicit veto on hard activity, it is useful to keep in mind that minimum bias includes a diverse mixture of both soft and hard processes, though the fraction that is made up of hard high- p_{\perp} processes is only a small tail compared to the total minimum-bias cross section³³.

In theoretical contexts, the term “minimum-bias” is often used with a slightly different meaning; to denote specific (classes of) inclusive soft-QCD subprocesses in a given model. Since these two usages are not exactly identical, in these lectures we have chosen to reserve the term “minimum bias” to pertain strictly to definitions of experimental measurements, and instead use the term “soft inclusive” physics as a generic descriptor for the class of processes which generally dominate the various experimental “minimum-bias” measurements in theoretical models. This parallels the terminology used in the review [6], from which most of the discussion here has been adapted. See equation (93) above for a compact overview of the types of physical processes that contribute to minimum-bias data samples. For a more detailed description of Monte Carlo models of this physics, see [6].

³³ Furthermore, since only a tiny fraction of the total minimum-bias rate can normally be stored, the minimum-bias sample would give quite poor statistics if used for hard physics studies. Instead, separate dedicated hard-process triggers are typically included in addition to the minimum-bias one, in order to ensure maximal statistics also for hard physics processes.

5.3 Underlying Event and Multiple Parton Interactions

In this subsection, we focus on the physics of multiple parton interactions (MPI) as a theoretical basis for understanding both inelastic, non-diffractive processes (minimum-bias), as well as the so-called underlying event (a.k.a. the jet pedestal effect). **Keep in mind, however, that especially at low multiplicities, and when rapidity gaps are present, the contributions from diffractive processes should not be ignored.**

Due to the simple fact that hadrons are composite, multi-parton interactions (several distinct parton-parton interactions in one and the same hadron-hadron collision) will always be there — but how many, and how much additional energy and tracks do they deposit in a given measurement region? The first detailed Monte Carlo model for perturbative MPI was proposed by Sjöstrand in [9], and with some variation this still forms the basis for most modern implementations [6].

The first crucial observation is that the t -channel propagators appearing in perturbative QCD $2 \rightarrow 2$ scattering almost go on shell at low p_\perp , causing the differential cross sections to become very large, behaving roughly as

$$d\sigma_{2 \rightarrow 2} \propto \frac{dt}{t^2} \sim \frac{dp_\perp^2}{p_\perp^4}. \quad (94)$$

At LHC energies, this *parton-parton* cross section becomes larger than the total *hadron-hadron* cross section at p_\perp scales of order 4–5 GeV. This is illustrated in figure 33, in which we compare the integrated QCD parton-parton cross section (with two different α_s and PDF choices) to the total inelastic cross section measured by TOTEM [178], for pp collisions at $\sqrt{s} = 8$ TeV. In the context of MPI models, this is interpreted straightforwardly to mean that **each hadron-hadron collision contains several few-GeV parton-parton collisions.**

In the limit that all the partonic interactions are independent and equivalent, one would simply have a Poisson distribution in the number of MPI, with average

$$\langle n \rangle(p_{\perp\text{min}}) = \frac{\sigma_{2 \rightarrow 2}(p_{\perp\text{min}})}{\sigma_{\text{tot}}}, \quad (95)$$

with $p_{\perp\text{min}}$ a lower cutoff scale which we shall return to below, and σ_{tot} a measure of the inelastic hadron-hadron cross section. This simple reinterpretation in fact expresses unitarity; instead of the total interaction cross section diverging as $p_{\perp\text{min}} \rightarrow 0$ (which would violate unitarity), we have restated the problem so that it is now the *number of MPI per collision* that diverges, with the total cross section remaining finite.

Two important ingredients remain to fully regulate the remaining divergence. Firstly, the interactions cannot use up more momentum than is available in the parent hadron. This suppresses the large- n tail of the estimate above. In PYTHIA-based models, the MPI are ordered in p_\perp [9, 123], and the parton densities for each successive interaction are explicitly constructed so that the sum of x fractions can never be greater than unity. In the HERWIG models [185, 186], instead the uncorrelated estimate of $\langle n \rangle$ above is used as an initial guess, but the generation of actual MPI is stopped once the energy-momentum conservation limit is reached.

The second ingredient invoked to suppress the number of interactions, at low p_\perp and x , is colour screening; if the wavelength $\sim 1/p_\perp$ of an exchanged coloured parton becomes

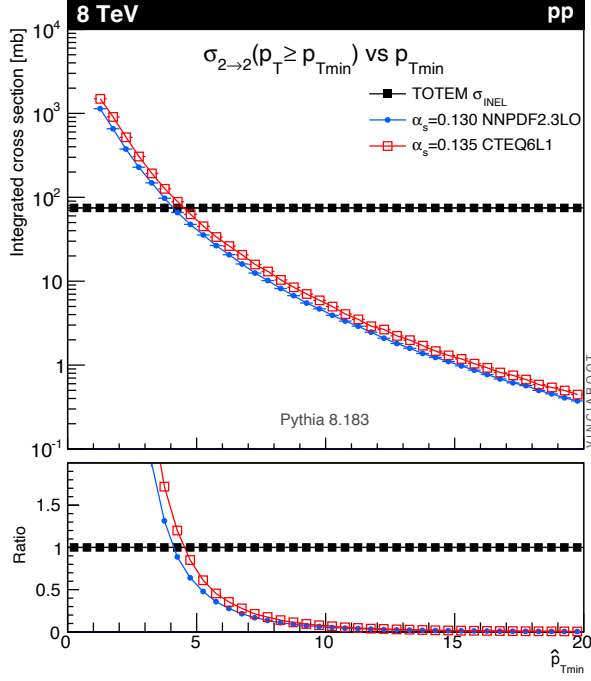


Figure 33: Proton-proton collisions at 8 TeV. LO QCD parton-parton cross section (integrated above $p_{T\text{min}}$, for two different α_s and PDF choices) compared to the total inelastic hadron-hadron cross section. Towards the right of the plot, we see, as expected, that hard dijet events is only a tiny fraction of the total cross section. The fact that the curves cross at a scale of order 5 GeV is interpreted to mean that this is a characteristic scale relevant for MPI. [169].

larger than a typical colour-anticolour separation distance, it will only see an *average* colour charge that vanishes in the limit $p_\perp \rightarrow 0$, hence leading to suppressed interactions. This provides an infrared cutoff for MPI similar to that provided by the hadronisation scale for parton showers. A first estimate of the colour-screening cutoff would be the proton size, $p_{\perp\text{min}} \approx /r_p \approx 0.3 \text{ GeV} \approx \Lambda_{\text{QCD}}$, but empirically this appears to be far too low. In current models, one replaces the proton radius r_p in the above formula by a “typical colour screening distance,” i.e., an average size of a region within which the net compensation of a given colour charge occurs. This number is not known from first principles, though it may be related to saturation [187]. In current MPI models, it is perceived of simply as an effective cutoff parameter, to be determined from data.

Note that the partonic cross sections depend upon the PDF set used, and therefore the optimal value to use for the cutoff will also depend on this choice [188]. Note also that the cutoff does not have to be energy-independent. Higher energies imply that parton densities can be probed at smaller x values, where the number of partons rapidly increases. Partons then become closer packed and the colour-screening distance d decreases. The uncertainty on the scaling of the cutoff is a major concern when extrapolating between different collider energies [188–190].

We now turn to the origin of the observational fact that hard jets appear to sit on top of a “pedestal” of underlying activity, which on average appears to be distributed evenly at all

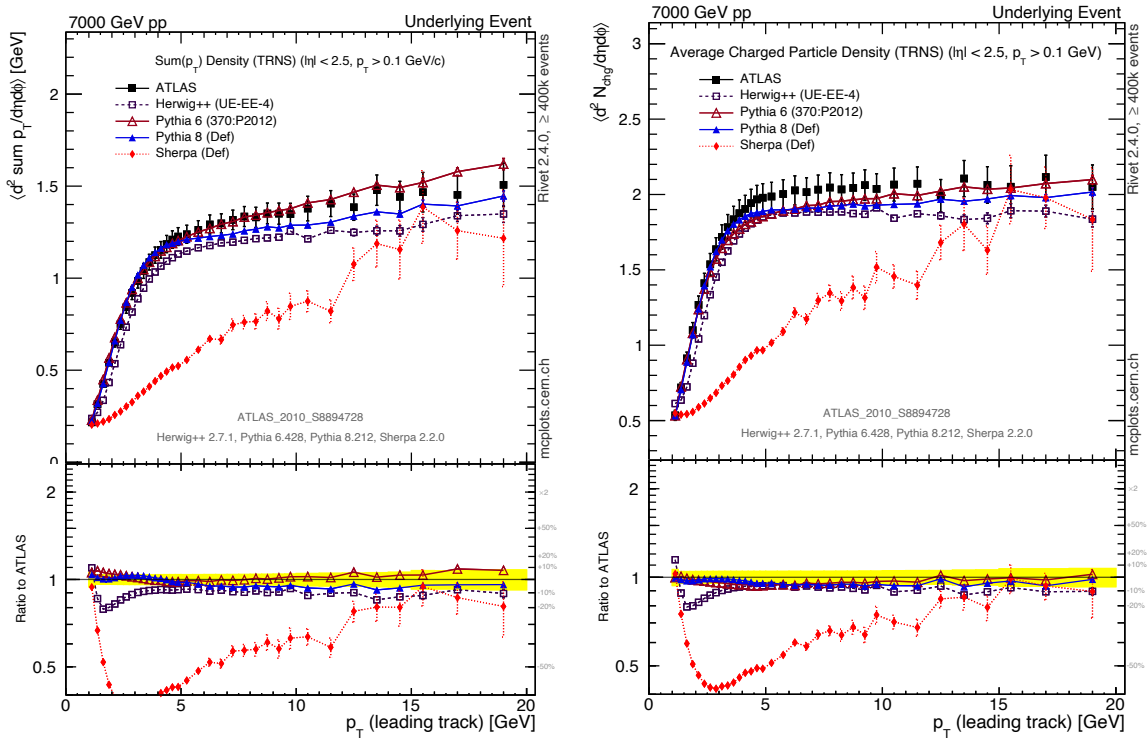


Figure 34: The rise of the Underlying Event, as a function of leading-track p_\perp , as measured in the “Transverse Region” defined by azimuthal angles $60^\circ < \Delta\phi < 120^\circ$ from the leading track, averaged over the available rapidity region. Left: average summed p_\perp (per unit $\Delta\eta\Delta\phi$) for all tracks with $p_\perp > 0.1$ GeV. Right: average number of charged tracks (per unit $\Delta\eta\Delta\phi$) with $p_\perp > 0.1$ GeV. Plots from mcplots.cern.ch [192].

rapidities (i.e., also far from the jet cores).

“Outside the [jet], a constant ET plateau is observed, whose height is independent of the jet ET. Its value is substantially higher than the one observed for minimum bias events.” (UA1 Collaboration (1983) [191])

That is, the so-called “underlying event” (UE) is substantially more active, with larger fluctuations, than the average min-bias event. In the MPI context, this is interpreted as a consequence of impact-parameter-dependence: in peripheral collisions, only a small fraction of events contain any high- p_\perp activity, whereas central collisions are more likely to contain at least one hard scattering; a high- p_\perp triggered sample will therefore be biased towards small impact parameters, b , with a larger number of MPI (and associated increased activity).

The rise of the pedestal level from low to high trigger-object³⁴ p_\perp is illustrated in figure 34. The leveling off of the distributions above leading-track p_\perp values ~ 5 GeV can be interpreted as an effect of “maximum bias”; when the trigger p_\perp is high enough, the selected events are

³⁴Different measurements and detectors employ different types of trigger objects, such as the leading track, leading track-jet, leading calorimeter jet, etc. In principle, the more inclusive (IR safe) the trigger is defined, the cleaner the measurement of the pedestal rise will be.

essentially already maximally biased to small impact parameters, and from that point onwards the UE essentially becomes “independent of the jet ET” [191] (modulo spillover of bremsstrahlung radiation from the hard-jet regions, which will still increase with the trigger-jet p_\perp ; this component can be partially suppressed e.g. by vetoing events with bremsstrahlung; by considering only the least active of the two UE regions; or by systematically classifying all of the activity in the event as either “jet-like” or “plateau-like” [99]). The ability of a theory model to describe the rise of the pedestal from the min-bias level to the UE plateau therefore depends upon its modeling of the b -dependence, and correspondingly the impact-parameter distribution (or, equivalently, the assumed mass distributions of the proton in b -space) constitutes another main tuning parameter. A detailed discussion of impact-parameter dependent models goes beyond the scope of these lectures; see [9, 174, 193].

For hard processes at the LHC at 13 TeV, the transverse energy, E_T , in the UE is expected to be about 3.3 GeV per unit $\Delta R = \sqrt{\Delta\phi^2 + \Delta\eta^2}$ area [190] (for a reference case of 100-GeV dijets, including both charged and neutral particles, with no cut on p_\perp), though with large event-to-event fluctuations of order ± 2 GeV [194]. Thus, for example, the total E_T originating from the UE, in a cone with radius 0.4 can be estimated to be $E_{TUE}(R = 0.4) \sim 1.6 \pm 1$ GeV, while the E_T in a cone with radius 1.0 would be $E_{TUE}(R = 1.0) \sim 10 \pm 6$ GeV. Note that the magnetic field in realistic detectors will deflect some fraction of the soft charged component of the underlying event into helix trajectories that will hence not contribute to the energy deposition in the calorimeters.

5.4 Tuning

A main virtue of general-purpose Monte Carlo event generators is their ability to provide a complete and fully differential picture of collider final states, down to the level of individual particles. As has been emphasised in these lectures, the achievable accuracy depends both on the inclusiveness of the chosen observable and on the sophistication of the simulation itself. An important driver for the latter is obviously the development of improved theoretical models, e.g., by including matching to higher-order matrix elements, more accurate resummations, or better non-perturbative models, as discussed in the previous sections; but it also depends crucially on the available constraints on the remaining free parameters of the model. Using existing data (or more precise calculations) to constrain these is referred to as generator tuning.

Keep in mind that generators attempt to deliver a *global* description of the data; a tune is no good if it fits one distribution perfectly, but not any others. It is therefore crucial to study the simultaneous degree of agreement or disagreement over many, mutually complementary, distributions. A useful online resource for making such comparisons can be found at the MCPLOTS web site [192] (which relies on computing power donated by volunteers, via the LHC@home project [195]). The analyses come from the comprehensive RIVET analysis toolkit [107], which can also be run stand-alone to make your own MC tests and comparisons.

Although MC models may appear to have a bewildering number of independently adjustable parameters, it is worth noting that most of these only control relatively small (exclusive) details of the event generation. The majority of the (inclusive) physics is determined by only a few, very important ones, such as the value of the strong coupling, in the perturbative domain, and the form of the fragmentation function for massless partons, in the non-perturbative one.

Armed with a good understanding of the underlying model, an expert would therefore normally take a highly factorised approach to constraining the parameters, first constraining the perturbative ones (using IR safe observables and/or more precise theory calculations) and thereafter the non-perturbative ones, each ordered in a measure of their relative significance to the overall modeling. This allows one to concentrate on just a few parameters and a few carefully chosen distributions at a time, reducing the full parameter space to manageable-sized chunks. Still, each step will often involve more than one single parameter, and non-factorisable correlations may still necessitate additional iterations from the beginning before a fully satisfactory set of parameters is obtained.

Recent years have seen the emergence of automated tools that attempt to reduce the amount of both computer and manpower required for this task, for instance by making full generator runs only for a limited set of parameter points, and then interpolating between these to obtain approximations to what the true generator result would have been for any intermediate parameter point, as, e.g., in PROFESSOR [196]. Automating the human expert input is more difficult. Currently, this is addressed by a combination of input solicited from the generator authors (e.g., which parameters and ranges to consider, which observables constitute a complete set, etc) and the elaborate construction of non-trivial weighting functions that determine how much weight is assigned to each individual bin in each distribution. The field is still burgeoning, and future sophistications are to be expected. Nevertheless, at this point the overall quality of the tunes obtained with automated methods appear to at least be competitive with the manual ones.

However, though we have very good LHC tunes for essentially all the general-purpose generators by now, there are two important aspects which have so far been neglected, and which it is becoming increasingly urgent to address. The first is that a central tune is not really worth much, unless you know what the uncertainty on it is. A few individual proposals for systematic tuning variations have been made [189, 197], but so far there is no general approach for establishing MC uncertainties by tune variations. (Note: in 2016 all of the general-purpose MC collaborations published strategies for automated evaluations of perturbative shower uncertainties, which we highly recommend the community to start using, see [15, 198, 199].) The second issue is that virtually all generator tuning is done at the “pure” LL shower level, and not much is known about what happens to the tuning when matrix-element matching is subsequently included³⁵.

Finally, rather than performing one global tune to all the data, as is usually done, a more systematic check on the validity of the underlying physics model could be obtained by instead performing several independent optimisations of the model parameters for a range of different phase-space windows and/or collider environments. In regions in which consistent parameter sets are obtained (with reasonable $\Delta\chi^2$ values), the underlying model can be considered as interpolating well, i.e., it is universal. If not, a breakdown in the ability of the model to span different physical regimes has been identified, and can be addressed, with the nature of the deviations giving clues as to the nature of the breakdown. With the advent of automated tools, such systematic studies are now becoming feasible, with a first example given in [188].

We round off by giving a sketch of a reasonably complete tuning procedure, without going into details about the parameters that control each of these sectors in individual Monte Carlo models (a recent detailed discussion in the context of PYTHIA 8 can be found in [169]):

³⁵One aspect, consistent α_s variations, is discussed in [142].

1) Keep in mind that inabilities of models to describe data is a vital part of the feedback cycle between theory and experiment. Also keep in mind that perturbation theory at (N)LO+LL is doing *very well* if it gets within 10% of a given IR safe measurement. An agreement of 5% should be considered the absolute sanity limit, beyond which it does not make any sense to tune further. For some quantities, e.g., ones for which the underlying modeling is known to be poor, an order-of-magnitude agreement or worse may have to be accepted.

2) Final-State Radiation and Hadronisation: mainly using LEP and other e^+e^- collider data. On the IR safe side, there are event shapes and jet observables. On the IR sensitive side, multiplicities and particle spectra. Pay attention to the high- z tail of the fragmentation, where a single hadron carries a large fraction of an entire jet's momentum (most likely to give “fakes”). Depending on the focus of the tuning, attention should also be paid to identified-particle rates and ratios (perhaps with a nod to hadron-collider measurements), and to fragmentation in events containing heavy quarks and/or gluon jets. Usually, more weight is given to those particles that are most copiously produced. The scaling properties of IR safe vs. IR sensitive contributions can be tested by comparing data at several different e^+e^- collider energies.

3) Initial-State Radiation, and “Primordial”³⁶ k_T : the main constraining distribution is the dilepton p_{\perp} distribution in Drell-Yan events in hadron-hadron collisions. Ideally, one would like to use several different Q^2 values, and/or complementary processes, like $p_{\perp}(\text{dijet})$ or $p_{\perp}(t\bar{t})$. For any observables containing explicit jets, be aware that the UE can produce small horizontal shifts in jet p_{\perp} distributions, which may in turn result in larger-than-expected vertical changes if the distributions are falling sharply. Also note that the ISR evolution is sensitive to the choice of PDFs.

4) Initial-Final Connections: (radiation from colour lines connecting the initial and final states): DIS and jet broadening in hadron collisions. This is one of the most poorly controlled parts of most MC models, highly sensitive to the treatment of coherence (see e.g. [200] for illustrations). Keep in mind that it is *not* directly constrained by pure final-state observables, such as LEP fragmentation, nor by pure initial-state observables, such as the Drell-Yan p_{\perp} spectrum, which is why we list it as a separate item here. The modeling of this aspect can have important effects on specific observables, a recent example being the $t\bar{t}$ forward-backward asymmetry at the Tevatron [201].

5) Underlying Event: Good constraints on the overall level of the underlying event can be obtained by counting the summed transverse energy (more IR safe) and/or particle multiplicities and average transverse momenta (more IR sensitive) in regions transverse to a hard trigger jet (more IR safe) or particle (more IR sensitive), see e.g. [202]. Constraints on the *fluctuations* of the underlying event are also important, and can be obtained, e.g., by comparing to measurements of the RMS of such distributions [194] or by plotting salient quantities along an axis from low to high UE activity [203]. Again, note that the UE modelling can be very sensitive to the choice of PDFs [169, 188]. Finally, the modeling of the UE should be *universal*, hence the same UE model should — ideally — be able to describe UE distributions not only in inclusive-jet events, but also the UE in processes like Drell-Yan [204–207] or $t\bar{t}$ production [208, 209].

6) Colour (Re-)Connections and other Final-State Interactions: By Final-State Inter-

³⁶Primordial k_T : an additional soft p_{\perp} component that is injected on top of the p_{\perp} generated by the initial-state shower itself, see [6, Section 7.1].

actions, we intend a broad spectrum of possible collective effects that may be included to a greater or lesser extent in various models. These effects include: Bose-Einstein correlations (see, e.g., [210]), rescattering (see, e.g., [211]), colour reconnections / string interactions (see, e.g., [212–216]), hydrodynamics (see, e.g., [217]), etc. As a rule, these effects are soft and/or non-perturbative and hence should not modify hard IR safe observables appreciably. They can, however, have *drastic* effects on IR sensitive ones, such as particle multiplicities, momentum distributions, and correlations, wherefore useful constraints are typically furnished by measurements of spectra and correlations as functions of quantities believed to serve as indicators of the strength of these phenomena (such as event multiplicity [218–220] or underlying-event activity [203]), and/or by collective-flow-type measurements. Finally, if the model includes a universal description of underlying-event and soft-inclusive QCD, as many MPI-based models do, then minimum-bias data can also be used as a control sample, though one must then be careful either to address diffractive contributions properly or to include only gap-suppressed data samples. A complete MB and UE model should also be able to describe the rise of the pedestal from MB to UE, e.g., in the transverse UE observables (see above).

7) Beam Remnants: Constraints on beam-remnant fragmentation (see, e.g., [174]) are most directly obtained in the forward region [221–227]. Especially for soft-inclusive triggers, cuts designed to isolate diffractive topologies are then required to distinguish effectively between the fragmentation of a (diffractive) colour-singlet excitation of the beam particle and that of a (non-diffractive) colour-charged remnant having exchanged some (non-zero) net amount of colour charge with the other colliding beam hadron. To lowest order, the remnant should be in a triplet (octet) colour state after having exchanged a quark (gluon) with the other beam particle, but taking MPI into account much larger amounts of colour may be transferred, with correspondingly larger possible colour representations of the remnant (see, e.g., [216]). The amount of baryon transport from the remnant to a given rapidity region [228–230] can also be used to probe how much the colour structure of the remnant was effectively disturbed, with more baryon transport indicating a larger amount of “beam baryon blowup”. Ideally one would also correlate the forward activity with a (central) measure of how much total colour charge is scattered out of the remnant(s), such as an observable sensitive to the number of MPI.

Acknowledgments

Thanks to C. Brust, M. Cacciari, Y. Dokshitzer, L. Hartgring, A. Kronfeld, A. Larkoski, J. Lopez-Villarejo, C. Murphy, P. Nason, P. Pigard, S. Prestel, G. Salam, and T. Sjöstrand whose valuable comments and sharing of insight contributed to these lectures. In addition, I have used material from my 2010 ESHEP lectures [152] and 2014 AEPSHEP lectures, and from the ESHEP lectures by Mangano [231], by Salam [5, 232], by Sjöstrand [50], and by Stirling [233], as well as the recent review on Monte Carlo event generators by the MCnet collaboration [6].

References

- [1] M. E. Peskin and D. V. Schroeder, *An Introduction to quantum field theory*. Addison-Wesley, 1995.
- [2] R. D. Field, “Applications of Perturbative QCD,” *Front. Phys.* **77** (1989) 1–366.
- [3] R. Ellis, W. Stirling, and B. Webber, *QCD and collider physics*. Camb. Monogr. Part. Phys. Nucl. Phys. Cosmol., 1996.
- [4] G. Dissertori, I. Knowles, and M. Schmelling, *Quantum Chromodynamics — High energy experiments and theory*. Oxford Science Publications, 2003.
- [5] G. P. Salam, “Elements of QCD for hadron colliders,” 1011.5131. In Proceedings of the 17th European school on high-energy physics (ESHEP), Bautzen, Germany, 14 - 27 June, 2009, arXiv:1012.4643.
- [6] **MCnet** Collaboration, A. Buckley, J. Butterworth, S. Gieseke, D. Grellscheid, S. Höche, *et al.*, “General-purpose event generators for LHC physics,” *Phys.Rept.* **504** (2011) 145–233, 1101.2599.
- [7] B. Andersson, G. Gustafson, G. Ingelman, and T. Sjöstrand, “Parton Fragmentation and String Dynamics,” *Phys. Rept.* **97** (1983) 31–145.
- [8] B. Andersson, *The Lund model*. Camb. Monogr. Part. Phys. Nucl. Phys. Cosmol., 1997.
- [9] T. Sjöstrand and M. van Zijl, “A multiple-interaction model for the event structure in hadron collisions,” *Phys. Rev.* **D36** (1987) 2019.
- [10] T. Sjöstrand, “The Development of MPI Modelling in PYTHIA,” 1706.02166.
- [11] F. James, “Monte Carlo theory and practice,” *Rept. Prog. Phys.* **43** (1980) 1145.
- [12] S. Weinzierl, “Introduction to Monte Carlo methods,” hep-ph/0006269.
- [13] S. Plätzer and M. Sjödahl, “The Sudakov Veto Algorithm Reloaded,” *Eur. Phys. J. Plus* **127** (2012) 26, 1108.6180.
- [14] L. Lönnblad, “Fooling Around with the Sudakov Veto Algorithm,” *Eur. Phys. J.* **C73** (2013), no. 3, 2350, 1211.7204.
- [15] S. Mrenna and P. Skands, “Automated Parton-Shower Variations in Pythia 8,” 1605.08352.
- [16] K. A. Brueckner, “Meson-Nucleon Scattering and Nucleon Isobars,” *Phys.Rev.* **86** (1952) 106–109.
- [17] C. Chedester, P. Isaacs, A. Sachs, and J. Steinberger, “Total cross sections of pi-mesons on protons and several other nuclei,” *Phys.Rev.* **82** (1951) 958–959.
- [18] E. Fermi, H. Anderson, A. Lundby, D. Nagle, and G. Yodh, “Ordinary and Exchange Scattering of Negative Pions by Hydrogen,” *Phys.Rev.* **85** (1952) 935–936.

- [19] H. Anderson, E. Fermi, E. Long, and D. Nagle, “Total Cross-sections of Positive Pions in Hydrogen,” *Phys.Rev.* **85** (1952) 936.
- [20] H. Anderson, E. Fermi, D. Nagle, and G. Yodh, “Deuterium Total Cross Sections for Positive and Negative Pions,” *Phys.Rev.* **86** (1952) 413–413.
- [21] D. E. Nagle, *The Delta: The First Pion Nucleon Resonance: Its Discovery and Applications*. 1984. LALP-84-27, DE84 017107, based on a lecture given at the University of Chicago Symposium in honor of H.L. Anderson, May 11, 1982.
- [22] O. Greenberg, “Spin and Unitary Spin Independence in a Paraquark Model of Baryons and Mesons,” *Phys.Rev.Lett.* **13** (1964) 598–602.
- [23] M. Han and Y. Nambu, “Three Triplet Model with Double SU(3) Symmetry,” *Phys.Rev.* **139** (1965) B1006–B1010.
- [24] S. Drell and T.-M. Yan, “Massive Lepton Pair Production in Hadron-Hadron Collisions at High-Energies,” *Phys.Rev.Lett.* **25** (1970) 316–320.
- [25] T. Plehn, D. Rainwater, and P. Z. Skands, “Squark and gluino production with jets,” *Phys.Lett.* **B645** (2007) 217–221, hep-ph/0510144.
- [26] J. Alwall, S. de Visscher, and F. Maltoni, “QCD radiation in the production of heavy colored particles at the LHC,” *JHEP* **0902** (2009) 017, 0810.5350.
- [27] A. Papaefstathiou and B. Webber, “Effects of QCD radiation on inclusive variables for determining the scale of new physics at hadron colliders,” *JHEP* **06** (2009) 069, 0903.2013.
- [28] D. Krohn, L. Randall, and L.-T. Wang, “On the Feasibility and Utility of ISR Tagging,” 1101.0810.
- [29] C. K. Vermilion, “Jet Substructure at the Large Hadron Collider: Harder, Better, Faster, Stronger,” 1101.1335.
- [30] A. Altheimer, S. Arora, L. Asquith, G. Brooijmans, J. Butterworth, *et al.*, “Jet Substructure at the Tevatron and LHC: New results, new tools, new benchmarks,” *J.Phys.G* **G39** (2012) 063001, 1201.0008.
- [31] **Particle Data Group** Collaboration, J. Beringer *et al.*, “Review of particle physics,” *Phys. Rev.* **D86** (2012) 010001.
- [32] S. P. Martin, “A Supersymmetry primer,” hep-ph/9709356.
- [33] P. Langacker, *The standard model and beyond*. 2010.
<http://www.sns.ias.edu/~pgl/SMB>.
- [34] S. Bethke, “World Summary of α_s (2012),” *Nucl.Phys.Proc.Suppl.* **234** (2013) 229–234, 1210.0325.
- [35] D. d’Enterria and P. Z. Skands, eds., *Proceedings, High-Precision α_s Measurements from LHC to FCC-ee*, CERN. CERN, Geneva, 2015. arXiv:1512.05194.

- [36] S. Bethke, “The 2009 World Average of alpha(s),” *Eur.Phys.J.* **C64** (2009) 689–703, 0908.1135.
- [37] G. Dissertori, A. Gehrmann-De Ridder, T. Gehrmann, E. Glover, G. Heinrich, *et al.*, “Determination of the strong coupling constant using matched NNLO+NLLA predictions for hadronic event shapes in e+e- annihilations,” *JHEP* **0908** (2009) 036, 0906.3436.
- [38] A. Young, “Quantitative substitutional analysis I,” *Proc. London Math. Soc.* **33** (1901) 97.
- [39] B. Sagan, “The ubiquitous young tableaux.” in *Invariant Theory and Tableaux*, ed. D. Stanton, Springer Verlag, 1990, p.262.
<http://www.math.msu.edu/users/sagan/Papers/0ld/uyt.pdf>.
- [40] J. Alwall, M. Herquet, F. Maltoni, O. Mattelaer, and T. Stelzer, “MadGraph 5 : Going Beyond,” *JHEP* **1106** (2011) 128, 1106.0522.
- [41] A. Pukhov, “Calchep 2.3: MSSM, structure functions, event generation, 1, and generation of matrix elements for other packages,” [hep ph/0412191](#).
- [42] **CompHEP** Collaboration, E. Boos *et al.*, “CompHEP 4.4: Automatic computations from Lagrangians to events,” *Nucl.Instrum.Meth.* **A534** (2004) 250–259, [hep ph/0403113](#).
- [43] A. Kanaki and C. G. Papadopoulos, “HELAC: A Package to compute electroweak helicity amplitudes,” *Comput.Phys.Commun.* **132** (2000) 306–315, [hep ph/0002082](#).
- [44] F. Krauss, R. Kuhn, and G. Soff, “AMEGIC++ 1.0: A Matrix element generator in C++,” *JHEP* **0202** (2002) 044, [hep ph/0109036](#).
- [45] M. Moretti, T. Ohl, and J. Reuter, “O’Mega: An Optimizing matrix element generator,” [hep ph/0102195](#).
- [46] W. Kilian, T. Ohl, and J. Reuter, “WHIZARD: Simulating Multi-Particle Processes at LHC and ILC,” *Eur.Phys.J.* **C71** (2011) 1742, 0708.4233.
- [47] A. Cafarella, C. G. Papadopoulos, and M. Worek, “Helac-Phegas: A Generator for all parton level processes,” *Comput.Phys.Commun.* **180** (2009) 1941–1955, 0710.2427.
- [48] M. Bähr, S. Gieseke, M. Gigg, D. Grellscheid, K. Hamilton, *et al.*, “Herwig++ Physics and Manual,” *Eur.Phys.J.* **C58** (2008) 639–707, 0803.0883.
- [49] T. Gleisberg and S. Hoeche, “Comix, a new matrix element generator,” *JHEP* **0812** (2008) 039, 0808.3674.
- [50] T. Sjöstrand, “Monte Carlo Generators,” [hep ph/0611247](#).
- [51] J. C. Collins and D. E. Soper, “Parton Distribution and Decay Functions,” *Nucl.Phys.* **B194** (1982) 445.
- [52] G. F. Sterman, “Partons, factorization and resummation, TASI 95,” [hep ph/9606312](#).

- [53] CTEQ Collaboration, R. Brock *et al.*, “Handbook of perturbative QCD: Version 1.1,” *Rev.Mod.Phys.* **67** (1995) 157–248.
- [54] T. Plehn, “LHC Phenomenology for Physics Hunters,” 0810.2281.
- [55] J. C. Collins, D. E. Soper, and G. F. Sterman, “Transverse Momentum Distribution in Drell-Yan Pair and W and Z Boson Production,” *Nucl.Phys.* **B250** (1985) 199.
- [56] G. Altarelli and G. Parisi, “Asymptotic freedom in parton language,” *Nucl. Phys.* **B126** (1977) 298–318.
- [57] V. N. Gribov and L. N. Lipatov, “Deep inelastic e - p scattering in perturbation theory,” *Sov. J. Nucl. Phys.* **15** (1972) 438.
- [58] Y. L. Dokshitzer, “Calculation of the structure functions for deep inelastic scattering and e^+e^- annihilation by perturbation theory in quantum chromodynamics,” *Sov. Phys. JETP* **46** (1977) 641–653.
- [59] NuTeV Collaboration, D. Mason *et al.*, “Measurement of the Nucleon Strange-Antistrange Asymmetry at Next-to-Leading Order in QCD from NuTeV Dimuon Data,” *Phys.Rev.Lett.* **99** (2007) 192001.
- [60] A. Cooper-Sarkar, “What did HERA teach us about the structure of the proton?,” 1206.0894.
- [61] S. Alekhin, K. Melnikov, and F. Petriello, “Fixed target Drell-Yan data and NNLO QCD fits of parton distribution functions,” *Phys.Rev.* **D74** (2006) 054033, [hep ph/0606237](#).
- [62] E. de Oliveira, A. Martin, and M. Ryskin, “Drell-Yan as a probe of small x partons at the LHC,” 1205.6108.
- [63] S. Alekhin, S. Alioli, R. D. Ball, V. Bertone, J. Blumlein, *et al.*, “The PDF4LHC Working Group Interim Report,” 1101.0536.
- [64] A. Buckley and M. Whalley, “HepData reloaded: reinventing the HEP data archive,” 1006.0517. <http://hepdata.cedar.ac.uk>.
- [65] A. Martin, W. Stirling, R. Thorne, and G. Watt, “Parton distributions for the LHC,” *Eur.Phys.J.* **C63** (2009) 189–285, 0901.0002.
- [66] J. Pumplin, D. Stump, J. Huston, H. Lai, P. M. Nadolsky, *et al.*, “New generation of parton distributions with uncertainties from global QCD analysis,” *JHEP* **0207** (2002) 012, [hep ph/0201195](#).
- [67] G. Watt and R. Thorne, “Study of Monte Carlo approach to experimental uncertainty propagation with MSTW 2008 PDFs,” *JHEP* **1208** (2012) 052, 1205.4024.
- [68] M. Bengtsson, T. Sjöstrand, and M. van Zijl, “Initial State Radiation Effects on W and Jet Production,” *Z. Phys.* **C32** (1986) 67.
- [69] S. Gieseke, “Uncertainties of Sudakov form-factors,” *JHEP* **0501** (2005) 058, [hep ph/0412342](#).

- [70] **NLO Multileg Working Group** Collaboration, Z. Bern *et al.*, “The NLO multileg working group: Summary report,” 0803.0494.
- [71] T. Kinoshita, “Mass singularities of Feynman amplitudes,” *J. Math. Phys.* **3** (1962) 650–677.
- [72] T. D. Lee and M. Nauenberg, “Degenerate Systems and Mass Singularities,” *Phys. Rev.* **133** (1964) B1549–B1562.
- [73] S. Catani and M. H. Seymour, “A general algorithm for calculating jet cross sections in NLO QCD,” *Nucl. Phys.* **B485** (1997) 291–419, hep-ph/9605323.
- [74] S. Catani and M. H. Seymour, “The Dipole Formalism for the Calculation of QCD Jet Cross Sections at Next-to-Leading Order,” *Phys. Lett.* **B378** (1996) 287–301, hep-ph/9602277.
- [75] Z. Nagy, “Next-to-leading order calculation of three jet observables in hadron hadron collision,” *Phys. Rev.* **D68** (2003) 094002, hep-ph/0307268.
- [76] R. Frederix, T. Gehrmann, and N. Greiner, “Automation of the Dipole Subtraction Method in MadGraph/MadEvent,” *JHEP* **09** (2008) 122, 0808.2128.
- [77] Y. I. Azimov, Y. L. Dokshitzer, V. A. Khoze, and S. I. Troian, “The String Effect and QCD Coherence,” *Phys. Lett. B* **165** (1985) 147–150.
- [78] D. A. Kosower, “Antenna factorization of gauge-theory amplitudes,” *Phys. Rev.* **D57** (1998) 5410–5416, hep-ph/9710213.
- [79] D. A. Kosower, “Antenna factorization in strongly-ordered limits,” *Phys. Rev.* **D71** (2005) 045016, hep-ph/0311272.
- [80] A. Gehrmann-De Ridder, T. Gehrmann, and E. W. N. Glover, “Antenna subtraction at NNLO,” *JHEP* **09** (2005) 056, hep-ph/0505111.
- [81] A. Gehrmann-De Ridder, T. Gehrmann, E. Glover, and G. Heinrich, “NNLO corrections to event shapes in e+ e- annihilation,” *JHEP* **0712** (2007) 094, 0711.4711.
- [82] S. Weinzierl, “NNLO corrections to 3-jet observables in electron-positron annihilation,” *Phys. Rev. Lett.* **101** (2008) 162001, 0807.3241.
- [83] G. Heinrich, “Sector Decomposition,” *Int.J.Mod.Phys.* **A23** (2008) 1457–1486, 0803.4177.
- [84] R. Boughezal, K. Melnikov, and F. Petriello, “A subtraction scheme for NNLO computations,” *Phys. Rev.* **D85** (2012) 034025, 1111.7041.
- [85] S. Catani and M. Grazzini, “An NNLO subtraction formalism in hadron collisions and its application to Higgs boson production at the LHC,” *Phys. Rev. Lett.* **98** (2007) 222002, hep-ph/0703012.
- [86] G. Gustafson and U. Pettersson, “Dipole formulation of QCD cascades,” *Nucl. Phys.* **B306** (1988) 746.

- [87] A. Gehrmann-De Ridder and M. Ritzmann, “NLO Antenna Subtraction with Massive Fermions,” *JHEP* **0907** (2009) 041, 0904.3297.
- [88] A. Gehrmann-De Ridder, M. Ritzmann, and P. Skands, “Timelike Dipole-Antenna Showers with Massive Fermions,” *Phys.Rev.* **D85** (2012) 014013, 1108.6172.
- [89] A. J. Larkoski and M. E. Peskin, “Spin-Dependent Antenna Splitting Functions,” *Phys.Rev.* **D81** (2010) 054010, 0908.2450.
- [90] W. Giele, D. Kosower, and P. Skands, “Higher-Order Corrections to Timelike Jets,” *Phys.Rev.* **D84** (2011) 054003, 1102.2126.
- [91] J. Lopez-Villarejo and P. Skands, “Efficient Matrix-Element Matching with Sector Showers,” *JHEP* **1111** (2011) 150, 1109.3608.
- [92] G. F. Sterman, “Resummation, power corrections and prediction in perturbative QCD,” in *QCD and high energy hadronic interactions. Proceedings, 33rd Rencontres de Moriond, Les Arcs, France, March 21-28, 1998*, pp. 511–518. 1998. hep ph/9806533.
- [93] A. Banfi, G. P. Salam, and G. Zanderighi, “Phenomenology of event shapes at hadron colliders,” *JHEP* **1006** (2010) 038, 1001.4082.
- [94] CMS Collaboration, V. Khachatryan *et al.*, “First Measurement of Hadronic Event Shapes in pp Collisions at $\sqrt{s} = 7$ TeV,” *Phys.Lett.* **B699** (2011) 48–67, 1102.0068.
- [95] ATLAS Collaboration, G. Aad *et al.*, “Measurement of event shapes at large momentum transfer with the ATLAS detector in pp collisions at $\sqrt{s} = 7$ TeV,” *Eur.Phys.J.* **C72** (2012) 2211, 1206.2135.
- [96] K. Wraight and P. Skands, “Forward-Backward Correlations and Event Shapes as probes of Minimum-Bias Event Properties,” *Eur.Phys.J.* **C71** (2011) 1628, 1101.5215.
- [97] M. Cacciari, G. P. Salam, and G. Soyez, “The Anti- $k(t)$ jet clustering algorithm,” *JHEP* **0804** (2008) 063, 0802.1189.
- [98] A. Abdesselam, E. B. Kuutmann, U. Bitenc, G. Brooijmans, J. Butterworth, *et al.*, “Boosted objects: A Probe of beyond the Standard Model physics,” *Eur.Phys.J.* **C71** (2011) 1661, 1012.5412.
- [99] M. Cacciari, G. P. Salam, and S. Sapeta, “On the characterisation of the underlying event,” *JHEP* **04** (2010) 065, 0912.4926.
- [100] G. Corcella *et al.*, “HERWIG 6: an event generator for hadron emission reactions with interfering gluons (including supersymmetric processes),” *JHEP* **01** (2001) 010, hep ph/0011363.
- [101] J. Bellm *et al.*, “Herwig 7.0/Herwig++ 3.0 release note,” *Eur. Phys. J.* **C76** (2016), no. 4, 196, 1512.01178.
- [102] T. Sjöstrand, S. Mrenna, and P. Skands, “PYTHIA 6.4 physics and manual,” *JHEP* **05** (2006) 026, hep ph/0603175.

- [103] T. Sjöstrand, S. Ask, J. R. Christiansen, R. Corke, N. Desai, *et al.*, “An Introduction to PYTHIA 8.2,” 1410.3012.
- [104] T. Gleisberg, S. Höche, F. Krauss, M. Schönher, S. Schumann, F. Siegert, and J. Winter, “Event generation with Sherpa 1.1,” *JHEP* **02** (2009) 007, 0811.4622.
- [105] E. Boos *et al.*, “Generic user process interface for event generators,” [hep ph/0109068](#).
- [106] J. Alwall *et al.*, “A standard format for Les Houches Event Files,” *Comput. Phys. Commun.* **176** (2007) 300–304, [hep ph/0609017](#).
- [107] A. Buckley *et al.*, “Rivet user manual,” 1003.0694.
- [108] **GEANT4** Collaboration, S. Agostinelli *et al.*, “GEANT4: A Simulation toolkit,” *Nucl.Instrum.Meth.* **A506** (2003) 250.
- [109] M. Dobbs and J. B. Hansen, “The HepMC C++ Monte Carlo event record for High Energy Physics,” *Comput. Phys. Commun.* **134** (2001) 41–46.
- [110] T. Sjöstrand, “Monte Carlo Tools,” 0911.5286.
- [111] R. Kleiss, W. Stirling, and S. Ellis, “A NEW MONTE CARLO TREATMENT OF MULTIPARTICLE PHASE SPACE AT HIGH-ENERGIES,” *Comput.Phys.Commun.* **40** (1986) 359.
- [112] G. Lepage, “A New Algorithm for Adaptive Multidimensional Integration,” *J.Comput.Phys.* **27** (1978) 192. Revised version.
- [113] G. P. Lepage, “VEGAS - An Adaptive Multi-dimensional Integration Program,” CLNS-80/447.
- [114] P. D. Draggiotis, A. van Hameren, and R. Kleiss, “SARGE: An Algorithm for generating QCD antennas,” *Phys.Lett.* **B483** (2000) 124–130, [hep ph/0004047](#).
- [115] N. Fischer, S. Prestel, M. Ritzmann, and P. Skands, “Vincia for Hadron Colliders,” 1605.06142.
- [116] G. Marchesini and B. Webber, “Simulation of QCD Jets Including Soft Gluon Interference,” *Nucl.Phys.* **B238** (1984) 1.
- [117] G. Marchesini and B. R. Webber, “Monte Carlo Simulation of General Hard Processes with Coherent QCD Radiation,” *Nucl. Phys.* **B310** (1988) 461.
- [118] S. Gieseke, P. Stephens, and B. Webber, “New formalism for QCD parton showers,” *JHEP* **12** (2003) 045, [hep ph/0310083](#).
- [119] M. Bengtsson and T. Sjöstrand, “A comparative study of coherent and non-coherent parton shower evolution,” *Nucl. Phys.* **B289** (1987) 810.
- [120] L. Lönnblad, “Ariadne version 4: A program for simulation of QCD cascades implementing the colour dipole model,” *Comput. Phys. Commun.* **71** (1992) 15–31.

- [121] Z. Nagy and D. E. Soper, “Matching parton showers to NLO computations,” *JHEP* **10** (2005) 024, [hep ph/0503053](#).
- [122] S. Schumann and F. Krauss, “A Parton shower algorithm based on Catani-Seymour dipole factorisation,” *JHEP* **0803** (2008) 038, [0709.1027](#).
- [123] T. Sjöstrand and P. Z. Skands, “Transverse-momentum-ordered showers and interleaved multiple interactions,” *Eur. Phys. J.* **C39** (2005) 129–154, [hep ph/0408302](#).
- [124] N. Fischer, S. Gieseke, S. Plätzer, and P. Skands, “Revisiting radiation patterns in e^+e^- collisions,” *Eur.Phys.J.* **C74** (2014) 2831, [1402.3186](#).
- [125] J. C. Collins, “SPIN CORRELATIONS IN MONTE CARLO EVENT GENERATORS,” *Nucl.Phys.* **B304** (1988) 794.
- [126] I. Knowles, “Spin Correlations in Parton - Parton Scattering,” *Nucl.Phys.* **B310** (1988) 571.
- [127] P. Richardson, “Spin correlations in Monte Carlo simulations,” *JHEP* **11** (2001) 029, [hep ph/0110108](#).
- [128] S. Catani, B. R. Webber, and G. Marchesini, “QCD coherent branching and semiinclusive processes at large x ,” *Nucl. Phys.* **B349** (1991) 635–654.
- [129] M. A. Gigg and P. Richardson, “Simulation of Finite Width Effects in Physics Beyond the Standard Model,” [0805.3037](#).
- [130] W. T. Giele, D. A. Kosower, and P. Z. Skands, “A Simple shower and matching algorithm,” *Phys. Rev.* **D78** (2008) 014026, [0707.3652](#).
- [131] M. H. Seymour, “The Higgs boson line shape and perturbative unitarity,” *Phys.Lett.* **B354** (1995) 409–414, [hep ph/9505211](#).
- [132] T. Stelzer and S. Willenbrock, “Spin correlation in top quark production at hadron colliders,” *Phys.Lett.* **B374** (1996) 169–172, [hep ph/9512292](#).
- [133] S. J. Parke and Y. Shadmi, “Spin correlations in top quark pair production at e^+e^- colliders,” *Phys.Lett.* **B387** (1996) 199–206, [hep ph/9606419](#).
- [134] J. M. Smillie and B. R. Webber, “Distinguishing spins in supersymmetric and universal extra dimension models at the large hadron collider,” *JHEP* **0510** (2005) 069, [hep ph/0507170](#).
- [135] M. H. Seymour, “A simple prescription for first-order corrections to quark scattering and annihilation processes,” *Nucl. Phys.* **B436** (1995) 443–460, [hep ph/9410244](#).
- [136] M. H. Seymour, “Matrix-element corrections to parton shower algorithms,” *Comp. Phys. Commun.* **90** (1995) 95–101, [hep ph/9410414](#).
- [137] S. Catani, F. Krauss, R. Kuhn, and B. R. Webber, “QCD matrix elements + parton showers,” *JHEP* **11** (2001) 063, [hep ph/0109231](#).

- [138] L. Lönnblad, “Correcting the colour-dipole cascade model with fixed order matrix elements,” *JHEP* **05** (2002) 046, [hep ph/0112284](#).
- [139] N. Lavesson and L. Lönnblad, “ $W + \text{jets}$ matrix elements and the dipole cascade,” *JHEP* **07** (2005) 054, [hep ph/0503293](#).
- [140] M. L. Mangano, M. Moretti, F. Piccinini, and M. Treccani, “Matching matrix elements and shower evolution for top-pair production in hadronic collisions,” *JHEP* **01** (2007) 013, [hep ph/0611129](#).
- [141] S. Mrenna and P. Richardson, “Matching matrix elements and parton showers with HERWIG and PYTHIA,” *JHEP* **05** (2004) 040, [hep ph/0312274](#).
- [142] B. Cooper, J. Katzy, M. Mangano, A. Messina, L. Mijovic, *et al.*, “Importance of a consistent choice of alpha(s) in the matching of AlpGen and Pythia,” *Eur.Phys.J.* **C72** (2012) 2078, [1109.5295](#).
- [143] N. Lavesson and L. Lönnblad, “Extending CKKW-merging to one-loop matrix elements,” *JHEP* **12** (2008) 070, [0811.2912](#).
- [144] S. Frixione and B. R. Webber, “Matching NLO QCD computations and parton shower simulations,” *JHEP* **06** (2002) 029, [hep ph/0204244](#).
- [145] S. Frixione, P. Nason, and B. R. Webber, “Matching NLO QCD and parton showers in heavy flavour production,” *JHEP* **08** (2003) 007, [hep ph/0305252](#).
- [146] S. Frixione and B. R. Webber, “The MC@NLO 3.4 Event Generator,” [0812.0770](#).
- [147] S. Frixione, P. Nason, and C. Oleari, “Matching NLO QCD computations with parton shower simulations: the POWHEG method,” *JHEP* **11** (2007) 070, [0709.2092](#).
- [148] K. Hamilton and P. Nason, “Improving NLO-parton shower matched simulations with higher order matrix elements,” *JHEP* **06** (2010) 039, [1004.1764](#).
- [149] M. Bengtsson and T. Sjöstrand, “Coherent Parton Showers Versus Matrix Elements: Implications of PETRA - PEP Data,” *Phys. Lett.* **B185** (1987) 435.
- [150] S. Alioli, P. Nason, C. Oleari, and E. Re, “A general framework for implementing NLO calculations in shower Monte Carlo programs: the POWHEG BOX,” *JHEP* **06** (2010) 043, [1002.2581](#).
- [151] L. Hartgring, E. Laenen, and P. Skands, “Antenna Showers with One-Loop Matrix Elements,” *JHEP* **1310** (2013) 127, [1303.4974](#).
- [152] P. Z. Skands, “QCD for Collider Physics,” [1104.2863](#). In 18th European school on high-energy physics (ESHEP), Raseborg, Finland, 20 June - 3 July, 2010, arXiv:1202.1629.
- [153] G. Bali and K. Schilling, “Static quark - anti-quark potential: Scaling behavior and finite size effects in SU(3) lattice gauge theory,” *Phys.Rev.* **D46** (1992) 2636–2646.

- [154] D. Amati and G. Veneziano, “Preconfinement as a Property of Perturbative QCD,” *Phys. Lett.* **B83** (1979) 87.
- [155] S. Ostapchenko, “Status of QGSJET,” *AIP Conf. Proc.* **928** (2007) 118–125, 0706.3784.
- [156] F. Riehn, R. Engel, A. Fedynitch, T. K. Gaisser, and T. Stanev, “A new version of the event generator Sibyll,” 1510.00568.
- [157] F. W. Bopp, J. Ranft, R. Engel, and S. Roesler, “Antiparticle to Particle Production Ratios in Hadron-Hadron and d-Au Collisions in the DPMJET-III Monte Carlo,” *Phys. Rev.* **C77** (2008) 014904, hep-ph/0505035.
- [158] F. W. Bopp, R. Engel, and J. Ranft, “Rapidity gaps and the PHOJET Monte Carlo,” in *High energy physics. Proceedings, LAFEX International School, Session C, Workshop on Diffractive Physics, LISHEP 98, Rio de Janeiro, Brazil, February 16-20, 1998*, pp. 729–741. 1998. hep-ph/9803437.
- [159] T. Pierog, I. Karpenko, J. M. Katzy, E. Yatsenko, and K. Werner, “EPOS LHC: Test of collective hadronization with data measured at the CERN Large Hadron Collider,” *Phys. Rev.* **C92** (2015), no. 3, 034906, 1306.0121.
- [160] S. Navin, “Diffraction in Pythia,” 1005.3894.
- [161] X. Artru and G. Mennessier, “String model and multiproduction,” *Nucl. Phys.* **B70** (1974) 93–115.
- [162] M. Travis, T. E. Ford, F. Laine, E. Presley, J. Cash, *et al.*, “Sixteen Tons.” Originally recorded for Folk Songs of the Hills, Capitol Records, 1946. Capitol T-891.
- [163] A. Casher, H. Neuberger, and S. Nussinov, “Chromoelectric Flux Tube Model of Particle Production,” *Phys. Rev.* **D20** (1979) 179–188.
- [164] J. S. Schwinger, “On gauge invariance and vacuum polarization,” *Phys. Rev.* **82** (1951) 664–679.
- [165] G. V. Dunne, “New Strong-Field QED Effects at ELI: Nonperturbative Vacuum Pair Production,” *Eur. Phys. J.* **D55** (2009) 327–340, 0812.3163.
- [166] N. K. Glendenning and T. Matsui, “CREATION OF ANTI-Q Q PAIR IN A CHROMOELECTRIC FLUX TUBE,” *Phys. Rev.* **D28** (1983) 2890–2891.
- [167] G. C. Nayak, “Non-perturbative quark-antiquark production from a constant chromo-electric field via the Schwinger mechanism,” *Phys. Rev.* **D72** (2005) 125010, hep-ph/0510052.
- [168] N. Fischer and T. Sjöstrand, “Thermodynamical String Fragmentation,” *JHEP* **01** (2017) 140, 1610.09818.
- [169] P. Skands, S. Carrazza, and J. Rojo, “Tuning PYTHIA 8.1: the Monash 2013 Tune,” *Eur.Phys.J.* **C74** (2014), no. 8, 3024, 1404.5630.

- [170] B. Andersson, G. Gustafson, and T. Sjöstrand, “A Model for Baryon Production in Quark and Gluon Jets,” *Nucl. Phys.* **B197** (1982) 45.
- [171] B. Andersson, G. Gustafson, and T. Sjöstrand, “BARYON PRODUCTION IN JET FRAGMENTATION AND UPSILON DECAY,” *Phys. Scripta* **32** (1985) 574.
- [172] P. Eden and G. Gustafson, “Baryon production in the string fragmentation picture,” *Z.Phys.* **C75** (1997) 41–49, hep ph/9606454.
- [173] T. Sjöstrand and P. Z. Skands, “Baryon number violation and string topologies,” *Nucl. Phys.* **B659** (2003) 243, hep ph/0212264.
- [174] T. Sjöstrand and P. Z. Skands, “Multiple interactions and the structure of beam remnants,” *JHEP* **03** (2004) 053, hep ph/0402078.
- [175] B. Andersson, G. Gustafson, and B. Söderberg, “A General Model for Jet Fragmentation,” *Z.Phys.* **C20** (1983) 317.
- [176] M. G. Bowler, “ e^+e^- production of heavy quarks in the string model,” *Z. Phys.* **C11** (1981) 169.
- [177] K. G. Wilson, “Confinement of Quarks,” *Phys.Rev.* **D10** (1974) 2445–2459.
- [178] **TOTEM** Collaboration, G. Antchev *et al.*, “Luminosity-Independent Measurement of the Proton-Proton Total Cross Section at $\sqrt{s} = 8$ TeV,” *Phys.Rev.Lett.* **111** (2013), no. 1, 012001.
- [179] A. Donnachie and P. Landshoff, “ $p\bar{p}$ and $\bar{p}p$ total cross sections and elastic scattering,” *Phys.Lett.* **B727** (2013) 500–505, 1309.1292.
- [180] V. Khoze, F. Krauss, A. Martin, M. Ryskin, and K. Zapp, “Diffraction and correlations at the LHC: Definitions and observables,” *Eur.Phys.J.* **C69** (2010) 85–93, 1005.4839.
- [181] B. Blok, Y. Dokshitzer, L. Frankfurt, and M. Strikman, “The Four jet production at LHC and Tevatron in QCD,” *Phys.Rev.* **D83** (2011) 071501, 1009.2714.
- [182] B. Blok, Y. Dokshitser, L. Frankfurt, and M. Strikman, “pQCD physics of multiparton interactions,” *Eur.Phys.J.* **C72** (2012) 1963, 1106.5533.
- [183] J. R. Gaunt and W. J. Stirling, “Single and Double Perturbative Splitting Diagrams in Double Parton Scattering,” 1202.3056.
- [184] A. V. Manohar and W. J. Waalewijn, “A QCD Analysis of Double Parton Scattering: Color Correlations, Interference Effects and Evolution,” *Phys.Rev.* **D85** (2012) 114009, 1202.3794.
- [185] J. M. Butterworth, J. R. Forshaw, and M. H. Seymour, “Multiparton Interactions in Photoproduction at HERA,” *Z. Phys.* **C72** (1996) 637–646, hep ph/9601371.
- [186] M. Bähr, J. M. Butterworth, S. Gieseke, and M. H. Seymour, “Soft interactions in Herwig++,” 0905.4671.

- [187] M. Ryskin, A. Martin, and V. Khoze, “High-energy strong interactions: from ‘hard’ to ‘soft’,” *Eur.Phys.J.* **C71** (2011) 1617, 1102.2844.
- [188] H. Schulz and P. Skands, “Energy Scaling of Minimum-Bias Tunes,” *Eur.Phys.J.* **C71** (2011) 1644, 1103.3649.
- [189] P. Z. Skands, “Tuning Monte Carlo Generators: The Perugia Tunes,” *Phys.Rev.* **D82** (2010) 074018, 1005.3457.
- [190] P. Z. Skands, “Soft-QCD and UE spectra in pp collisions at very high CM energies (a Snowmass white paper),” 1308.2813.
- [191] UA1 Collaboration, G. Arnison *et al.*, “Hadronic Jet Production at the CERN Proton - anti-Proton Collider,” *Phys. Lett.* **132B** (1983) 214.
- [192] A. Karneyeu, L. Mijovic, S. Prestel, and P. Skands, “MCPLOTS: a particle physics resource based on volunteer computing,” *Eur.Phys.J.* **C74** (2014) 2714, 1306.3436.
- [193] R. Corke and T. Sjöstrand, “Multiparton Interactions with an x-dependent Proton Size,” *JHEP* **1105** (2011) 009, 1101.5953.
- [194] ATLAS Collaboration, G. Aad *et al.*, “Measurement of underlying event characteristics using charged particles in pp collisions at $\sqrt{s} = 900\text{GeV}$ and 7 TeV with the ATLAS detector,” *Phys.Rev.* **D83** (2011) 112001, 1012.0791.
- [195] D. Lombrana Gonzalez, L. Rivkin, M. Zacharov, I. an Giovannozzi, E. McIntosh, *et al.*, “LHC@home: a Volunteer Computing System for Massive Numerical Simulations of Beam Dynamics and High Energy Physics Events,” *Conf.Proc.* **C1205201** (2012) 505–507.
- [196] A. Buckley, H. Hoeth, H. Lacker, H. Schulz, and J. E. von Seggern, “Systematic event generator tuning for the LHC,” *Eur. Phys. J.* **C65** (2010) 331–357, 0907.2973.
- [197] P. Richardson and D. Winn, “Investigation of Monte Carlo Uncertainties on Higgs Boson searches using Jet Substructure,” 1207.0380.
- [198] J. R. Andersen *et al.*, “Les Houches 2015: Physics at TeV Colliders Standard Model Working Group Report,” in *9th Les Houches Workshop on Physics at TeV Colliders (PhysTeV 2015) Les Houches, France, June 1-19, 2015.* 2016. 1605.04692.
- [199] J. Bellm, S. Platzer, P. Richardson, A. Siódmiak, and S. Webster, “Reweighting Parton Showers,” 1605.08256.
- [200] M. Ritzmann, D. Kosower, and P. Skands, “Antenna Showers with Hadronic Initial States,” *Phys.Lett.* **B718** (2013) 1345–1350, 1210.6345.
- [201] P. Skands, B. Webber, and J. Winter, “QCD Coherence and the Top Quark Asymmetry,” *JHEP* **1207** (2012) 151, 1205.1466.
- [202] R. Field, “Min-Bias and the Underlying Event at the LHC,” *Acta Phys.Polon.* **B42** (2011) 2631–2656, 1110.5530.

- [203] T. Martin, P. Skands, and S. Farrington, “Probing Collective Effects in Hadronisation with the Extremes of the Underlying Event,” *Eur. Phys. J.* **C76** (2016), no. 5, 299, 1603.05298.
- [204] CDF Collaboration, T. Aaltonen *et al.*, “Studying the Underlying Event in Drell-Yan and High Transverse Momentum Jet Production at the Tevatron,” *Phys. Rev.* **D82** (2010) 034001, 1003.3146.
- [205] CMS Collaboration, S. Chatrchyan *et al.*, “Measurement of the underlying event in the Drell-Yan process in proton-proton collisions at $\sqrt{s} = 7$ TeV,” *Eur. Phys. J.* **C72** (2012) 2080, 1204.1411.
- [206] ATLAS Collaboration, G. Aad *et al.*, “Measurement of distributions sensitive to the underlying event in inclusive Z-boson production in pp collisions at $\sqrt{s} = 7$ TeV with the ATLAS detector,” *Eur. Phys. J.* **C74** (2014), no. 12, 3195, 1409.3433.
- [207] S. Alioli, C. W. Bauer, S. Guns, and F. J. Tackmann, “Underlying event sensitive observables in Drell-Yan production using GENEVA,” 1605.07192.
- [208] CMS Collaboration, “Study of the underlying event, b-quark fragmentation and hadronization properties in tbart events,” . CMS-PAS-TOP-13-007.
- [209] CMS Collaboration, “Underlying event measurement with ttbar+X events with p-p collision data at $\text{sqrt}(s)=13$ TeV,” . CMS-PAS-TOP-15-017.
- [210] L. Lönnblad and T. Sjöstrand, “Modelling Bose-Einstein correlations at LEP 2,” *Eur. Phys. J.* **C2** (1998) 165–180, hep ph/9711460.
- [211] R. Corke and T. Sjöstrand, “Multiparton interactions and rescattering,” *JHEP* **01** (2009) 035, 0911.1909.
- [212] J. Rathsman, “A generalised area law for hadronic string reinteractions,” *Phys. Lett.* **B452** (1999) 364–371, hep ph/9812423.
- [213] P. Z. Skands and D. Wicke, “Non-perturbative QCD effects and the top mass at the Tevatron,” *Eur.Phys.J.* **C52** (2007) 133–140, hep ph/0703081.
- [214] F. Bopp and J. Ranft, “Inclusive distributions in p-p collisions at LHC energies compared with an adjusted DPMJET-III model with chain fusion,” in *Proceedings, 3rd International Workshop on Multiple Partonic Interactions at the LHC (MPI@LHC 2011)*, pp. 41–49. 2011. 1110.6403.
- [215] S. Gieseke, C. Rohr, and A. Siódak, “Colour reconnections in Herwig++,” *Eur.Phys.J.* **C72** (2012) 2225, 1206.0041.
- [216] J. R. Christiansen and P. Z. Skands, “String Formation Beyond Leading Colour,” *JHEP* **08** (2015) 003, 1505.01681.
- [217] K. Werner, I. Karpenko, and T. Pierog, “Hydrodynamical evolution in heavy ion collisions and p p scatterings at the LHC: Ridges in A A and p p scattering,” *Acta Phys.Polon.Supp.* **4** (2011) 629–634.

- [218] P. R. Petrov, *Strangeness enhancement in high multiplicity proton-proton collisions at $\sqrt{s} = 7$ TeV with the ALICE detector at the LHC*. PhD thesis, Birmingham U., 2012-11-28.
- [219] C. Bierlich and J. R. Christiansen, “Effects of color reconnection on hadron flavor observables,” *Phys. Rev.* **D92** (2015), no. 9, 094010, 1507.02091.
- [220] **ALICE** Collaboration, J. Adam *et al.*, “Multiplicity-dependent enhancement of strange and multi-strange hadron production in proton-proton collisions at $\sqrt{s} = 7$ TeV,” 1606.07424.
- [221] **CMS** Collaboration, S. Chatrchyan *et al.*, “Measurement of energy flow at large pseudorapidities in pp collisions at $\sqrt{s} = 0.9$ and 7 TeV,” *JHEP* **11** (2011) 148, 1110.0211. [Erratum: JHEP02,055(2012)].
- [222] **CMS** Collaboration, S. Chatrchyan *et al.*, “Forward Energy Flow, Central Charged-Particle Multiplicities, and Pseudorapidity Gaps in W and Z Boson Events from pp Collisions at $\sqrt{s} = 7$ TeV,” *Eur. Phys. J.* **C72** (2012) 1839, 1110.0181.
- [223] **TOTEM** Collaboration, G. Antchev *et al.*, “Measurement of the forward charged particle pseudorapidity density in pp collisions at $\sqrt{s} = 7$ TeV with the TOTEM experiment,” *Europhys. Lett.* **98** (2012) 31002, 1205.4105.
- [224] **CMS** Collaboration, S. Chatrchyan *et al.*, “Study of the underlying event at forward rapidity in pp collisions at $\sqrt{s} = 0.9$, 2.76, and 7 TeV,” *JHEP* **04** (2013) 072, 1302.2394.
- [225] **LHCb** Collaboration, R. Aaij *et al.*, “Measurement of charged particle multiplicities and densities in pp collisions at $\sqrt{s} = 7$ TeV in the forward region,” *Eur. Phys. J.* **C74** (2014), no. 5, 2888, 1402.4430.
- [226] **CMS, TOTEM** Collaboration, S. Chatrchyan *et al.*, “Measurement of pseudorapidity distributions of charged particles in proton-proton collisions at $\sqrt{s} = 8$ TeV by the CMS and TOTEM experiments,” *Eur. Phys. J.* **C74** (2014), no. 10, 3053, 1405.0722.
- [227] **TOTEM** Collaboration, G. Antchev *et al.*, “Measurement of the forward charged particle pseudorapidity density in pp collisions at $\sqrt{s} = 8$ TeV using a displaced interaction point,” *Eur. Phys. J.* **C75** (2015), no. 3, 126, 1411.4963.
- [228] S. Erhan, W. S. Lockman, T. Meyer, J. Rander, P. Schlein, R. Webb, and J. Zsemenyi, “HYPERON PRODUCTION IN P P INTERACTIONS AT $S^{**}(1/2) = 53$ -GEV AND 62-GEV,” *Phys. Lett.* **B85** (1979) 447–451.
- [229] **LHCb** Collaboration, R. Aaij *et al.*, “Measurement of V^0 production ratios in pp collisions at $\sqrt{s} = 0.9$ and 7 TeV,” *JHEP* **08** (2011) 034, 1107.0882.
- [230] **D0** Collaboration, V. M. Abazov *et al.*, “Measurement of the forward-backward asymmetry of Λ and $\bar{\Lambda}$ production in $p\bar{p}$ collisions,” *Phys. Rev.* **D93** (2016), no. 3, 032002, 1511.05113.

- [231] N. Ellis, R. Fleischer, *et al.*, “Proceedings of the 2008 European School of High-Energy Physics (ESHEP), Herbeumont-sur-Semois, Belgium, 8 - 21 June 2008,”. CERN-2009-002.
- [232] C. Grojean, M. Spiropulu, *et al.*, “Proceedings of the 2009 European School of High-Energy Physics (ESHEP), Bautzen, Germany, 14 - 27 June 2009,” 1012.4643.
- [233] N. Ellis, R. Fleischer, *et al.*, “2007 European School of High-Energy Physics, Trest, Czech Republic, 19 August - 1 September 2007,”. CERN-2008-007.

Index

- Adjoint representation, 5
- α_s , 5, 10–14
 - beta function, 11
 - Λ_{QCD} , 13, 14
 - Landau Pole, *see* Λ_{QCD}
 - Running coupling, 10–14
- Altarelli-Parisi, *see* DGLAP
- Angular ordering, 32, 37, 42
- Antenna functions, *see* Antennae
- Antennae, 28, 29, 36, 43
- Anti-kT algorithm, *see* Jets
- Area law, 57
- Asymptotic freedom, 12, 13
- Baryons, 4, 56
- Beta function, 11
- Bjorken scaling, *see* QCD Scale invariance
- Breit-Wigner distribution, 44
- Bremsstrahlung, *see* Parton showers
- C_A , 8, 10, 28
- Casimirs, 6, 8
- Catani-Seymour dipoles, 28
- Causality, 54
- C_F , 8, 10, 28
- CKKW, *see* Matching, 47
- Cluster model, 51
- Coherence, 15, 37
- Collinear limit, 24, 26, 28, 30, 35, 36
- Color connections, 28
- Color factors, 28
- Colour connections, 8, 66
- Colour factors, 6, 7, 10
- Colour-space indices, *see* Colour connections
- Confinement, 51, 53
- Conformal invariance, 10
- Convergence, 33, 34
- Decuplet, 4, 16
- Deep inelastic scattering, *see* DIS
- Detailed balance, 41
- DGLAP equation, 20
- DGLAP kernels, 20, 28, 43
- Diffractive scattering, 58, 59
- Diquarks, 16, 56
- DIS, 7, 18, 20, 66
- Double counting, 45
- Drell-Yan, 7, 20
- Eightfold way, 4
- Eikonal, 28, 29, 36
- Elastic scattering, 58
- Event evolution, *see* Evolution
- Event generators, *see* Monte Carlo
- Event shapes, 30
- Evolution, 40–42
- Exclusive cross sections, 40, 41, 45
- Factorisation, 18, 35
 - Caveats, 20
 - Factorisation scale, 19, 35, 42
- Flavour, 4, 12, 14
 - In string breaks, 55, 56
- Fragmentation functions, 35, 52, 56
- Fundamental representation, 5
- Gell-Mann matrices, *see* SU(3)
- Gluons, 6, 8, 9
 - As kinks on strings, 53
 - Contribution to beta function, 11
 - PDFs, 21
- Hadronisation, 31, 51
- Hadronisation scale, 42, 51, 55
- HERWIG, 32, 45, 46, 51
- Inclusive cross sections, 20, 40, 41, 45
- Inelastic scattering, 58
- Infrared divergences, 24, 25, 33
- Infrared safety, 29–31
- Jets, 10, 24, 27, 35, 40
 - Algorithms, *see* [5]
 - Anti-kT algorithm, 31
 - Cambridge/Aachen algorithm, 31
 - Definitions, *see* [5]
 - Infrared safety, 29, 30
 - kT algorithm, 31

- Kinoshita-Lee-Nauenberg, *see* KLN theorem
- KLN theorem, 25, 27, 28, 40
- Λ_{QCD} , *see* α_s
- Landau pole, *see* α_s
- Lattice QCD, 15, 51
- Les Houches Event Files, *see* LHEF
- LHEF, 32
- Lightcone scaling, *see* QCD Scale invariance
- Linear confinement, *see* Confinement
- LO, 24, 25, 45
- Lund symmetric fragmentation function, 56
 - Bowler modification, 57
- Markov chains, 34, 42, 43
- Matching, 45–50
 - CKKW, 45, 47
 - L-CKKW, 45, 47
 - Matching scale, 47
 - MCatNLO, 48
 - MENLOPS, 49
 - MLM, 45, 47
 - POWHEG, 48
 - Slicing, 45
 - Subtraction, 48
 - Unitarity, 49
 - VINCIA, 50
- Matching scale, *see* Matching
- Matrix elements, 6, 17, 24, 25
- MCatNLO, *see* Matching
- MCnet review, 32
- MENLOPS, *see* Matching
- Mesons, 4, 55, 56
- Minimum-bias events, 58, 60
- MLM, *see* Matching
- Monte Carlo
 - Convergence, 34
 - Decay distributions, 44
 - Event generators, 22, 32, 51, 64, 65
 - Integration, 32–34
 - Monaco, 34
 - Pedagogical introduction, 44
 - RAMBO, 33
 - Statistics, 33
 - Tuning, 39, 55, 64, 65
 - Uncertainties, 33, 64
 - VEGAS, 34
- Narrow width approximation, 44
- NLO, 19, 24–28, 48
 - Infrared divergences, 24, 25
 - NNLO, 24, 26–28
 - Nobel prize, 12, 25
 - Numerical integration, 33
- Octet, 4
- Parton Distributions, *see* PDFs
- Parton level, 51
- Parton showers, 10, 22, 31, 34, 42
 - Evolution variable, 42
 - Infrared cutoff, *see* Hadronisation scale
 - Initial-state evolution, 22
 - Sudakov factor, 43
- Partons, 3, 20
- PDFs, 19, 20, 35
- POWHEG, *see* Matching, 50
- pQCD, 24, 29, 34
- Preconfinement, 51
- Primary hadrons, 51
- p_\perp -ordering, 42
- PYTHIA, 32, 50, 51, 53, 56, 61
- QCD
 - Colour factors, 6
 - Coupling, 5, 6, 10
 - Lagrangian, 3, 5
 - Landau Pole, *see* α_s
 - Renormalisation, *see* α_s
 - Scale invariance, 10, 24, 47
 - Structure constants, *see* SU(3)
 - Trace relations, *see* SU(3)
- Quarks, 4–7
 - As string endpoints, 53
 - Contribution to beta function, 11
 - PDFs, 21
- RAMBO, 33, 34
- Renormalisation, *see* α_s
- Resonance decays, 44
- SARGE, 34
- Scale invariance, *see* QCD
- Schwinger Mechanism, 54, 56
- Sector decomposition, 28
- Sextet, 15

- SHERPA, 32, 51
- Soft eikonal, *see* Eikonal
- Soft limit, 24, 26, 28, 30, 36
- Spin correlations, 39, 44
- String breaks, 54
- String junctions, 16, 56
- String model, 51, 53, 55, 66
- Strong coupling, 13
- Structure functions, 22
- SU(3), 4, 5, 8
 - Adjoint representation, 5
 - Fundamental representation, 5
 - Generators, 6
 - Of Colour, 4
 - Of Flavour, 4
 - Structure constants, 8
 - Trace relations, 8
- Subtraction, 27–29
 - In the context of matching, 48
- Subtraction schemes, 29
- Sudakov factor, 43, 45, 50
- T_R , 8
- Traces in SU(3), *see* SU(3)
- Transcendentality, 39
- Transverse-momentum-ordering, *see* p_\perp -ordering
- Tuning, *see* Monte Carlo
- Tunneling, 54
- Twist, 20
- Uncertainties
 - Factorisation, 19, 20
 - Monte Carlo statistics, 33
 - PDF sets, 21
- Underlying event, 31, 51, 58
- Unitarity, 25, 27, 40
- VEGAS, *see* Monte Carlo
- VINCIA, 34, 50
 - Matching, 50
- Young tableaux, 16